Electron- and photon-induced fragmentation of molecular ions

Annette Svendsen

Department of Physics and Astronomy
University of Aarhus, Denmark

PhD Thesis
August 2006

Contents

PHOTON-INDUCED FRAGMENTATION OF BIOMOLECULES

APPENDIX

Preface

This thesis has been submitted to the Faculty of Science at the University of Aarhus, Denmark, in order to fulfill the requirements for the PhD degree. The work presented in this thesis has been carried out under the supervision of Dr. Lars H. Andersen at the Department of Physics and Astronomy at the University of Aarhus from August 2002 to August 2006.

Acknowledgements

Without the help and support from a great number of people, the present thesis would not have come into existence. I would like to take the opportunity to acknowledge the persons that I have been so fortunate to work with.

First and foremost, I am indebted to my supervisor, Lars H. Andersen. He has been an excellent mentor, and I have always been able to count on his expertise whenever it was needed. Moreover, I have highly appreciated that he always have taken the time to answer whatever questions I might have had and to discuss results and new experiments. Steen Brøndsted Nielsen is gratefully acknowledged for the many fruitful discussions we have had during my time as a PhD student and for being a good friend.

When I first joined the group, I had the pleasure of working with Henrik Bluhme and Klaus Seiersen who always kept spirits high in the lab. Together with Lars, they are acknowledged for having taught me how to operate the electron targets and the ELISA storage ring. Later on, Mohamed El Ghazaly joined the group, and he is thanked for his efforts during experiments. During the last year, I have been fortunate to work with Lutz Lammich who is extremely skillful in the lab and always pleasant company. Furthermore, Hella Sand and Marianne Sanggaard are thanked for good company in the lab, and Iben B. Nielsen and Helle Krogh for contributing to the good atmosphere in the group.

Søren Pape Møller, Jørgen S. Nielsen, and Niels Hertel are gratefully ac-

knowledged for their assistance, especially during ASTRID beam times. In particular, Jørgen and Niels are thanked for teaching me the basics about running the ASTRID storage ring, for always coming up with solutions to experimental problems, for making life easier during beam times with the SMS system, and for their pleasant company.

Kåre Iversen, Jens Vestergaard, and Karsten Rasmussen are thanked for technical assistance. In particular, I have enjoyed chitchating with Jens and Karsten when receiving their help. Finn Abildskov has been a great help concerning the hardware for absolute ion current measurements and the software for controlling the electron targets which he has been working on even after his retirement.

I cannot keep track of all the times I have needed the assistance of Poul Erik Eriksen and his crew in the electronics department. In this respect, I would like to mention Erik Søndergaard, Helge Wahlgreen, Per Bluhme Christensen, Frank Mikkelsen, and Paul Aggerholm who often have helped in solving our problems concerning electronic equipment.

Egon Jans is thanked for his help in preparing sputter ion sources and maintaining them with high spirits. Klaus Bahner is also thanked in this respect.

Erik Lægsgaard is gratefully acknowledged for sharing his immense knowledge of solid-state detectors and for his involvement concerning MATLAB programming. Bjarke Christensen and Peter Balling are thanked for their help concerning the laser system used at Separator II.

Anette Skovgaard is acknowledged for proofreading English manuscripts prepared during my PhD studies. I have very much appreciated the comments on the present manuscript from Lutz and Henrik who both have read things very thoroughly.

For two months, I had the pleasure of visiting the group of Prof. Carl Lineberger at JILA, in Boulder, Colorado. I would like to thank Jack Barbera, Joshua P. Martin, and Vladimir Dribinski for good hours both in and outside the lab. Furthermore, the rest of the Lineberger group is thanked for creating a friendly atmosphere.

During my time at the university, I have met many great people some of whom have become very good friends. Thank you for all the good times we have had so far. Furthermore, my family is gratefully acknowledged for always being very supportive and especially my parents for always letting me know that they are proud of me. Finally, I would like to thank Kristian for his immense support, patience and for taking my thoughts of writing from time to time.

Annette Svendsen
July 31st, 2006

List of publications

This thesis is based on the following publications:

I. **A. Svendsen**, L. Lammich, M. Sanggaard, and L. H. Andersen,
Electron-impact detachment of PO_n^- ($n = 0$–3)
In preparation

II. **A. Svendsen**, H. Bluhme, K. Seiersen, and L. H. Andersen,
Electron scattering on $OH^-(H_2O)_n$ clusters ($n = 0$–4)
J. Chem. Phys. **121**, 4642 (2004)

III. **A. Svendsen**, H. Bluhme, M. O. A. El Ghazaly, K. Seiersen, S. B. Nielsen, and L. H. Andersen,
Tuning the Continuum Ground State Energy of NO_2^{2-} by Water Molecules
Phys. Rev. Lett. **94**, 223401 (2005)

IV. L. Lammich, H. Sand, **A. Svendsen**, I. B. Nielsen, and L. H. Andersen
Microsecond dynamics in the gas phase photoabsorption of retinal chromophores
In preparation

During my PhD studies, I have furthermore participated in a number of experiments which will not be discussed in this thesis. This work has led to the following publications:

V. G. Angelova, O. Novotny, J. B. A. Mitchell, C. Rebrion-Rowe, J. L. LeGarrec, H. Bluhme, **A. Svendsen**, and L. H. Andersen
Branching ratios for the dissociative recombination of hydrocarbon ions III: the cases of $C_3H_n^+$ ($n = 1$–8)
Int. J. Mass. Spec. **235**, 7 (2004)

VI. L. H. Andersen, H. Bluhme, S. Boyé, T. J. D. Jørgensen, H. Krogh, I. B. Nielsen, S. B. Nielsen, and **A. Svendsen**,
Experimental studies of the photophysics of gas-phase fluorescent protein chromophores
Phys. Chem. Chem. Phys. **6**, 2617 (2004)

VII. H. Bluhme, M. J. Jensen, S. B. Nielsen, U. V. Pedersen, K. Seiersen, **A. Svendsen**, and L. H. Andersen,
Electron scattering on stored mononucleotide anions
Phys. Rev. A **70**, 020701 (2004)

VIII. M. O. A. El Ghazaly, **A. Svendsen**, H. Bluhme, A. B. Nielsen, S. B. Nielsen, and L. H. Andersen,
Electron Scattering on Centrosymmetric Molecular Dianions $Pt(CN)_4^{2-}$ and $Pt(CN)_6^{2-}$
Phys. Rev. Lett. **93**, 203201 (2004)

IX. J. B. A. Mitchell, O. Novotny, G. Angelova, J. L. LeGarrec, C. Rebrion-Rowe, **A. Svendsen**, L. H. Andersen, A. I. Florescu-Mitchell, and A. E. Orel
Dissociative recombination of rare gas hydride ions: I. NeH^+
J. Phys. B **38**, 693 (2005)

X. M. O. A. El Ghazaly, **A. Svendsen**, H. Bluhme, S. B. Nielsen, and L. H. Andersen,
Electron scattering on p-benzoquinone anions
Chem. Phys. Lett. **405**, 278 (2005)

XI. J. B. A. Mitchell, O. Novotny, J. L. LeGarrec, A. Florescu-Mitchell, C. Rebrion-Rowe, A. V. Stolyarov, M. S. Child, **A. Svendsen**, M. A. El Ghazaly, and L. H. Andersen,
Dissociative recombination of rare gas hydride ions: II. ArH^+
J. Phys. B **38**, L175 (2005)

XII. O. Novotny, J. B. A. Mitchell, J. L. LeGarrec, A. I. Florescu-Mitchell, C. Rebrion-Rowe, **A. Svendsen**, M. A. El Ghazaly, L. H. Andersen, A. Ehlerding, A. A. Viggiano, F. Hellberg, R. D. Thomas, V. Zhaunerchyk, W. D. Geppert, H. Montaigne, M. Kaminska, F. Österdahl, and M. Larsson,
The dissociative recombination of fluorocarbon ions: II. CF^+
J. Phys. B **38**, 1471 (2005)

XIII. **A. Svendsen**, M. O. A. El Ghazaly, and L. H. Andersen,
Molecular size effect in NCO and NCS dianion resonances
J. Chem. Phys. **123**, 114311 (2005)

XIV. O. Heber, K. Seiersen, H. Bluhme, **A. Svendsen**, L. H. Andersen, and L. Maunoury,
Dissociative recombination of small carbon cluster anions
Phys. Rev. A **73**, 022712 (2006)

XV. A. Ehlerding, A. A. Viggiano, F. Hellberg, R. D. Thomas, V. Zhaunerchyk, W. D. Geppert, H. Montaigne, M. Kaminska, F. Österdahl, M. Ugglas, M. Larsson, O. Novotny, J. B. A. Mitchell, J. L. LeGarrec, A. I. Florescu-Mitchell, C. Rebrion-Rowe, **A. Svendsen**, M. A. El Ghazaly, and L. H. Andersen,
The dissociative recombination of fluorocarbon ions: III. CF_2^+ and CF_3^+
J. Phys. B **39**, 805 (2006)

XVI. V. Dribinski, J. Barbera, J. P. Martin, **A. Svendsen**, M. A. Thompson, R. Parson, and W. C. Lineberger,
Time-resolved study of solvent induced recombination in photodissociated $IBr^-(CO_2)_n$ clusters
J. Chem. Phys., accepted for publication

Outline of the thesis

Chapter 1 gives a general motivation of the work presented in this thesis.

Chapter 2 provides motivations for studying electron-anions collisions and introduces the most important reactions occurring upon electron impact on a negative ion. Moreover, a brief overview of the field is given to initiate the reader unfamiliar with the research field. Finally, questions addressed in this work are outlined.

Chapter 3 presents the experimental techniques employed in this work to realize experimental studies of electron scattering. Ion sources used for negative-ion production are described followed by introductions to the experimental setups at two storage rings, ASTRID and ELISA.

In **Chapter 4**, results on electron collisions with PO_n^- ($n = 0$–3) are reported. The measured reaction cross sections are presented in addition to the branching ratios of the most important reactions occurring as a result of electron impact.

Chapter 5 deals with electron impact on small anion-water clusters, the particular clusters being $OH^-(H_2O)_n$ ($n = 0$–4). Cross sections for various reactions have been measured, and also the relative importance of different reaction channels is elucidated.

In **Chapter 6**, the influence of water molecules on the electronic stability of NO_2^{2-}, a small doubly charged negative ion, is investigated. This has been done by bombarding $NO_2^-(H_2O)_n$ ($n = 0$–2) with electrons and studying the capture of the incident electron.

Chapter 7 gives a brief conclusion and discussion on the outlook for new experiments on electron-anion collisions.

Chapter 8 introduces a new experimental setup. This setup may be used to follow the temporal evolution of photoexcited molecular ions. Presently, preliminary results on the timescales for dissociation of photoexcited chromophores are presented.

Chapter 9 forms the last chapter of the thesis and serves as a brief summary.

CHAPTER 1

Introduction

The present thesis deals with electron- and photon-induced fragmentation of molecular ions. The main part of the work concentrates on understanding the interactions between electrons and negative molecular ions. A smaller part is concerned with the molecular dynamics following photoabsorption by large molecular cations. Both processes are of fundamental interest to study, since they play an important role in the world that surrounds us.

Collisions between electrons and negative ions occur constantly in the atmosphere of the Earth and may also take place in interstellar clouds. Not only in these naturally occurring plasmas, but also in man-made ones used for materials processing do these reactions influence the chemical composition. Hence, knowledge about electron-ion interactions is needed to model the properties of these media. Moreover, the interactions between electrons and molecules are of relevance to life sciences. One of the main mechanisms behind radiation damage has been suggested to originate from collisions between biological molecules and low-energy electrons. Through ionization, the incident radiation produces free electrons which may inflict severe damage to surrounding biomolecules by causing cleavage of molecular bonds, directly or indirectly.

The absorption of light and the subsequent photophysical processes occurring in photoexcited molecules are examples of other types of reactions ubiquitous in nature. The interactions between light and molecules are responsible for, for instance, photosynthesis and human vision. Thus, studies of the response of biomolecules to absorption of light provide a piece of information that contributes to achieving a more detailed understanding of many processes important in biology.

Apart from the fact that both electron and photon collisions with molecules are common in nature, it is also of more general interest to study them.

Investigations of these interactions form the basis of obtaining a better understanding of the underlying physics involved. As a result, the ability of theory to describe such reactions and make predictions is brought to a higher level.

The current work focuses on experimental investigations of the interactions of electrons or light with ions. Some of the phenomena mentioned above take place in environments, which are bound to affect the nature of the reactions. However, a satisfactory understanding of complex reactions can emerge only from knowledge about more simple systems, the description of which is feasible to theory. The approach chosen here is thus to study such interactions in the gas phase. Here, the molecular ions are isolated implying that any influence of the surroundings is absent, and consequently the processes can be studied under more controlled conditions as compared to, for instance, liquid phase experiments. Hence, this work represents one step of the way to a full understanding of reactions that occur when electrons or light interact with molecules.

PART I
ELECTRON-INDUCED FRAGMENTATION OF ANIONS

CHAPTER 2

Overview of electron-anion collisions

The present chapter serves as an introduction to the field of electron-anion collisions. It begins with motivations for studying negative ions and an outline of the different processes occurring as a result of electron impact on an anion. Earlier experimental work on the subject is reviewed along with theoretical studies aiming at reproducing the measured cross sections. Since electron-anion collisions may be used to probe unstable multiply charged anions, a section on doubly charged anions is included. Finally, the questions addressed in the present work are outlined.

2.1 Introduction

Negative ions, anions, exhibit properties which are remarkably different from those of their neutral and positive counterparts. Whereas the positive and neutral species have an infinite number of bound excited states, anions only have a few, if any [1]. This contrast may be traced to the different nature of the binding potentials. In neutral molecules and positively charged ions, the electrons are bound by the long-range Coulomb potential which is capable of supporting an infinite number of bound states. However, in a negative ion, the excess electron feels a short-range r^{-4} potential. This r^{-4} dependence originates from the interaction between the excess electron and an induced dipole moment in the remaining neutral system. At a distance r, the electric field, $\vec{E} \propto \vec{r}/r^3$, of the excess electron induces a dipole moment, $\vec{P} \propto \alpha\vec{E}$, α being the polarizability, to the neutral species which in turn gives rise to

an attractive potential, $V(r) \propto \vec{P} \cdot \vec{E} \propto r^{-4}$. Unlike the Coulomb potential, this weaker potential only allows for a finite number of bound states. As the short-range potential emerges from interactions between the charge cloud of the neutral parent and the additional electron, the motion of the electrons are inherently correlated. For anions, inter-electronic interactions thus become relatively more important than the attractive interactions between electrons and the nuclei, which normally dominate the positive and neutral species. As electron correlations often account for the properties of anions, the independent electron model provides a poor description of these systems. More sophisticated models beyond the Hartree-Fock approximation must therefore be employed. Given the fact that electron correlations are difficult to handle, anions accordingly present a challenge to theory, and comparison between experiments and theory thus provides a sensitive probe of the ability of various models to correctly describe these correlation effects. It should further be noted that electron correlations are of interest to theoretical physics in general since such effects are a common theme in physics, for example superconductivity is a result of electron-electron interactions.

Apart from being interesting from a fundamental point of view, anions also play an important role in various branches of physics. Already in 1939, Wildt proposed that H^- is the predominant source of the opacity of the Sun and of photospheres in general [2, 3], a theory later confirmed by calculations and measurements [4, 5]. Not only H^-, but also other atomic and molecular anions are of importance to astrophysics as they are considered to take part in the chemistry of stars and interstellar media. An example is that of small linear carbon cluster anions which exhibit absorption spectra comparing very well with spectra of interstellar media [6]. In our own atmosphere, anions are abundant in the form of e.g. O_2^- and ClO^-, and such species must therefore be included in models aiming at describing the atmosphere [7, 8]. Furthermore, negative ions are present in plasmas and discharges which are of importance to laser action and materials processing. The properties of plasmas are strongly dependent on the presence of anions, and hence knowledge about cross sections for various collisional processes involving anions is needed to model plasma behavior.

The present work involving scattering of free electrons by negative ions was initiated for mainly two reasons. Firstly, it is the aim to gain more insight into the collision dynamics by characterizing the reaction cross sections with respect to threshold behaviors and general energy-dependencies. For atomic and small molecular anions, the detachment cross sections display very similar features. It is therefore interesting to investigate if the same general trends persist when the complexity of the target is increased. Secondly, electron scattering provides a unique tool for studying *unstable* multiply charged anions in the isolated phase. These systems are very intriguing and present a chal-

lenge both to experiments and to theory. Experimentally, the problem arises due to the extremely short lifetime of the order of 10^{-15} s, which makes it virtually impossible to study such states by direct observations. The theoretical description of these unstable species is complicated by both the coupling to the continuum and especially the high degree of electron correlations, which are of utmost importance. A more elaborate discussion on electron scattering as a means of studying unstable multiply charged anions is given below.

2.2 Electron-induced reactions

The quantity studied in electron-anion collision experiments is the cross section for various electron-induced reactions. Due to the detection scheme used in the present work, only cross sections for reactions leading to production of neutral fragments can be measured. In the following, emphasis is therefore put on reactions producing neutral fragments.

When free electrons collide with anions, several processes can occur. The negative ion can be neutralized in the collision by *detachment* of a bound electron:

$$AB^- + \mathrm{e}^- \rightarrow \begin{cases} AB + 2\mathrm{e}^- \\ A + B + 2\mathrm{e}^- \end{cases}, \tag{2.1}$$

illustrated here for the case where an electron collides with a heteronuclear diatomic anion, AB^-. In the first reaction, the anion interacts with a free electron producing a neutral molecule, AB, and two free electrons in a *pure detachment* process. Electron impact might also cause a transition to a dissociative potential energy curve of the neutral leading to two neutral atoms, $A + B$, and two free electrons with the final result of *detachment plus dissociation* (or *dissociative detachment*). In Fig. 2.1, these reactions are illustrated in terms of the relevant potential energy curves of the anion and the neutral.

Other processes leading to production of neutrals are *dissociation* and double electron detachment combined with dissociation:

$$AB^- + \mathrm{e}^- \rightarrow \begin{cases} A^- + B + \mathrm{e}^- \\ A^+ + B + 3\mathrm{e}^- \end{cases}, \tag{2.2}$$

In the pure dissociation event, the anion is lifted to an excited electronic state, which is dissociative, while the colliding electron escapes with reduced energy. The dissociation proceeds through an excited repulsive state of the anion, and hence the process may be called dissociative excitation in accordance with the nomenclature used in electron impact on positive ions [9]. Similarly, the process of double electron detachment plus dissociation may proceed by a repulsive state of the positive ion.

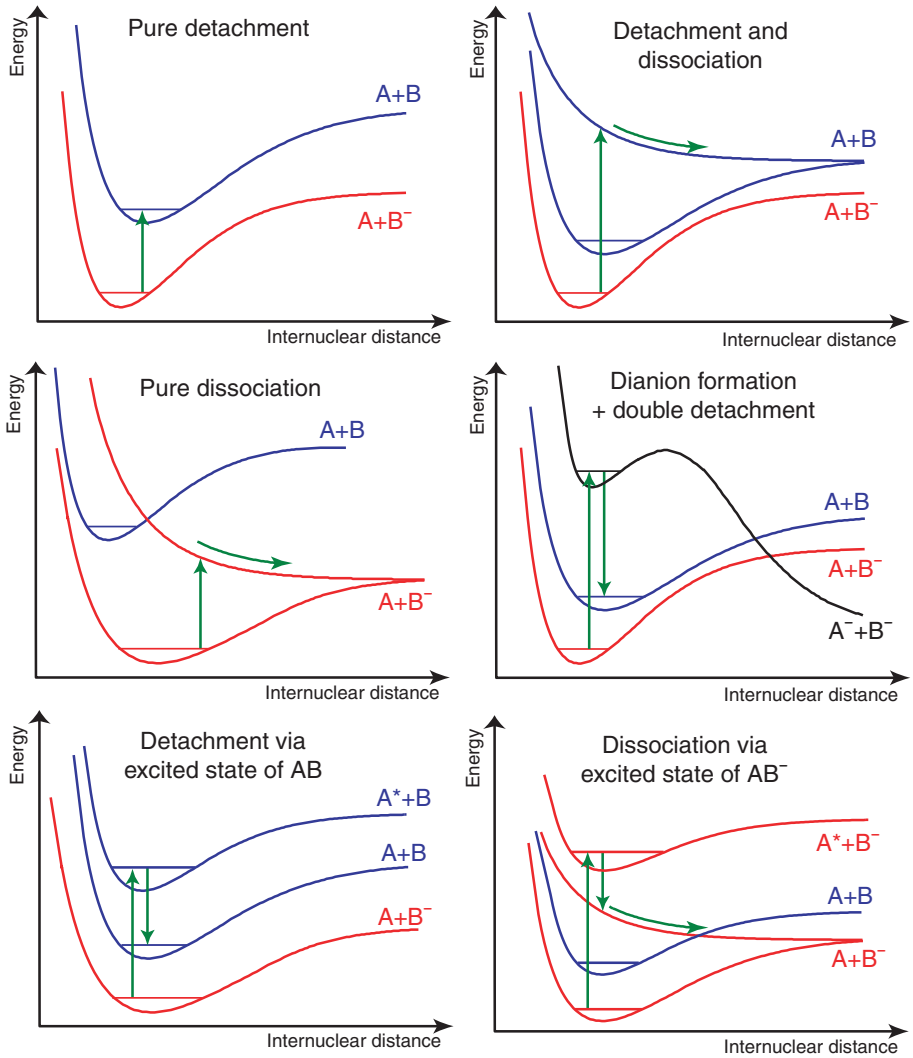

Figure 2.1: Schematic representation of some of the possible reaction mechanisms arising from electron impact on an anion. The red curves represent potential energy curves for different electronic states of the monoanion, AB^-, the blue ones relevant potential energy curves for the neutral, AB, while the black one shows the potential energy curve for a doubly charged anion, AB^{2-}.

The minimum collision energy needed for a certain reaction to become possible is referred to as the *threshold energy*, and one may ask what is the threshold energy for a particular process. The naive answer is that the energy of the incident electron at the threshold must equate the energy difference between the initial and final states, that is the energetic threshold. However, this is not quite the case, as the situation is complicated by the Coulomb repulsion in the incoming channel. For the incident electron to trigger a reaction, it must first come sufficiently close to the anion which involves overcoming the Coulomb repulsion. To some extent this can be accomplished by tunnelling through the Coulomb barrier, but the reaction probability is strongly enhanced if the projectile electron carries more energy than needed to cause the actual transition. Hence, the *effective* threshold energy for any electron-induced reaction is higher than the energetic threshold. As an example, the effective threshold energy for pure detachment is found to be a factor of 2–3 higher than the actual binding energy of the target excess electron [10, 11].

The dominant reaction channel is usually pure detachment, since electron binding energies for anions are generally smaller than dissociation energies. If, however, the overlap between the nuclear wave functions in the anionic and neutral molecules is unfavorable, pure detachment is suppressed, and the flux goes into dissociation instead [12, 13].

All the processes presented above can occur at any incident-electron energy above the threshold energy for the reaction. This is true since the projectile electron leaves the molecule after the collision and is allowed to carry away an arbitrary amount of energy. Therefore, the processes are *non-resonant* and give rise to cross sections that are smooth functions of the energy of the incoming electron. Meanwhile, some reactions can cause pronounced structures in the cross section, and the origin of such structures can in principle be traced to two different types of *resonant* processes.

One possibility is that the incoming electron excites the anion to a resonant state in the continuum, which subsequently autodetaches and/or dissociates:

$$AB^- + \mathrm{e}^- \rightarrow AB^{*-} + \mathrm{e}^- \rightarrow \begin{cases} AB + 2\mathrm{e}^- \\ A + B + 2\mathrm{e}^- \\ A^- + B + \mathrm{e}^- \end{cases} . \tag{2.3}$$

Here, the asterisk symbolizes an excited state. However, the resonant character of these processes is relaxed as excitation may occur at any incident-electron energy above the threshold, like the case for the non-resonant processes. Consequently, the reactions in Eq. (2.3) are not expected to result in resonant structures in the cross section.

In another type of process, the incoming electron is captured into a resonance state of a *doubly charged negative ion* (dianion) which subsequently de-

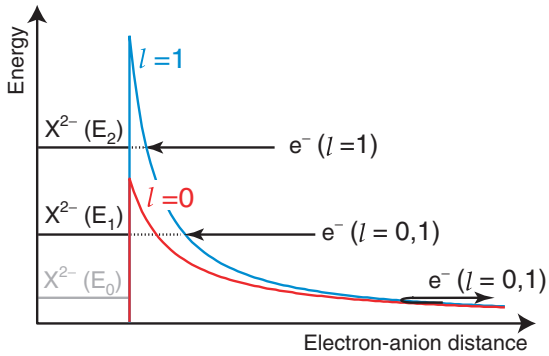

Figure 2.2: The scattering problem shown schematically. The potential energy of the scattering electron is shown as a function of the electron-anion distance for two values of the angular momentum l. E_0 represents a low-energy state of the dianion which is unlikely to be populated due to the thickness of the barrier, E_1 a 'visible' state of intermediate energy, and E_2 a state which can only be supported if the incoming electron carries an angular momentum greater than zero.

cays:

$$AB^- + \mathrm{e}^- \;\rightarrow\; AB^{2-} \;\rightarrow\; \text{decay products.} \tag{2.4}$$

This is a true resonant process in the sense that the energy of the incident electron must match the energy of the resonance state for the reaction to occur. Hence, such a process can give rise to peak-like structures in the cross section.

Due to the Coulomb repulsion, it may seem unlikely that the projectile electron can be captured and thereby become part of a transient dianion. To explain how this may still happen, it is useful to describe the collision dynamics in more detail, and a schematic illustration of the scattering problem is shown in Fig. 2.2. When the electron scatters on the anion, the long-range interaction is mainly electrostatic repulsion, and the potential energy therefore increases as the electron approaches the target. As the electron comes closer to the target it experiences the electrostatic attraction of the target nuclei, and thus a decrease in potential energy. When the long-range repulsion and the short-range attraction are combined, a repulsive Coulomb barrier emerges behind which dianionic states may exist (the resonances are thus *shape resonances* [14, 15]). For the incoming electron to populate these states in a scattering event, the Coulomb barrier has to be penetrated through quantum mechanical tunnelling. However, if a dianionic state is located at low energy where the barrier is thick, penetration becomes virtually impossible, thus hindering the free electron from becoming part of a new dianion. At higher energies, the barrier is less impervious and excited states, if existing, might be

populated.

The presence of the Coulomb barrier has been discussed by several authors [16–18], and the existence of the barrier has indeed been verified experimentally through a series of photoelectron spectroscopy studies of multiply charged anions [19, 20]. The exact form of this repulsive Coulomb barrier is very difficult to describe as it depends strongly on the interaction between the incident electron and the electron cloud of the anion [16, 18]. In addition, a repulsive centrifugal term $l(l+1)/2r^2$ (l is the angular momentum of the free electron) needs to be taken into consideration, a contribution which heightens the barrier. As a consequence, states which lie above the Coulomb barrier may be supported if the incoming electron carries an angular momentum of $l > 0$ [21].

The electron scattering technique presents an unique opportunity to study transient dianionic states situated in the electronic continuum. Most other techniques used for studying gas-phase dianions, like mass spectrometry and photoelectron spectroscopy, rely on the dianions exhibiting a sufficiently long lifetime to be detected in the experiments, usually implying that the lifetimes must be greater than 10^{-7}–10^{-6} s. As states near the top of the barrier are extremely short-lived with lifetimes in the order of femtoseconds, such transient species cannot be studied by these techniques. Instead, these short-lived states can be probed by bombarding monoanions with free electrons as described above. The states give rise to peak-like structures superimposed on the non-resonant cross section with widths that are partially determined by the lifetime of the dianion formed [21]. Typically, the observed width is a few eV, implying a lifetime τ in the order of femtoseconds ($\Delta E \sim \hbar/\tau$). Thus, a structure in the cross section is an indication of dianion formation.

It should be noted that the continuum dianionic states are only observed in scattering experiments if they lie in a certain energy range. The upper energy limit arises from the fact that the state must be located below the top of the combined angular momentum and Coulomb repulsive barriers. If not, the state becomes a virtual state with an extremely short lifetime, since there is no potential barrier keeping the incoming electron trapped. From the relationship between the resonance width and the lifetime, this implies that the resonance structure becomes extremely wide and is washed out. As already discussed, the lower energy limit is governed by a low probability to tunnel through the barrier. However, there is another effect which influences the lower energy limit. In the experiments considered here, the formation of transient dianions is identified by detection of *neutral* decay fragments. Hence, for the state to be observable, decay into neutral fragments must be possible, which imposes a restriction on the resonance energy. First of all, to create neutrals the resonance energy must be greater than the electron-binding energy of the monoanion or the lowest energy for dissociation into charged and neutral fragments. Sec-

ondly, due to their mutual repulsion, the escaping charged fragments, possibly electrons, must carry kinetic energy at far distance. Hence, the resonance energy must exceed the sum of the two energy contributions for the dianion to be detectable in experiments.

2.3 Previous investigations

Several investigations on electron-anions collisions have been carried out prior to this work, and an overview of these investigations is given in the following section. The two main aspects of electron-anion collisions are the threshold behavior of the detachment cross section and structures in the cross section attributed to the formation of doubly charged negative ions. The overview describes the two aspects separately, and both experimental and theoretical results are outlined.

2.3.1 Threshold behavior

As already mentioned, Wildt suggested in 1939 that H^- is the predominant source of the opacity of the Sun [2], and later this hypothesis was in fact confirmed [4, 5]. Electron-impact detachment was considered an important mechanism for the destruction of H^- and knowledge about the absolute cross section and its energy dependence was needed to model photospheres. Motivations for initiating experiments were thus laid out, and the first experimental results on electron-impact detachment from H^- were published in 1966 by Tisone and Branscomb [22]. They used a so-called *crossed-beams* setup where an H^- beam of well-defined energy was crossed at right angles ($\theta = 90°$) with an electron beam. In the following years, several experimental results using the crossed-beams technique were obtained [23–25], but a common feature was lack of data in the threshold region. To obtain a low collision energy, it was necessary to go to low electron energies in the laboratory frame, and in this energy range, the experiments struggled with poor electron beam intensities. This situation resulted in an extremely low signal-to-noise ratio making measurements impossible. In the 1970s, Peart and Dolder therefore employed an *inclined-beams* method where the angle, θ, between the ion and electron beams was changed to 10°–20°. Changing the angle made measurements at low collision energies possible as higher electron beam energies could now be employed to obtain the same collision energies as for the crossed-beams setup. Using this method, Peart and coworkers measured electron-impact detachment cross sections for H^- [26–28], C^- [29, 30], O^- [29, 30], and F^- [31].

After these experiments in the 1970s, no experiments in the field of electron-anion collisions were carried out for almost two decades. Only with the ad-

vent of magnetic storage rings was the field revitalized. Magnetic storage rings had been used in nuclear and particle physics for many years, and in the early 1990s a small number of ion storage rings dedicated to atomic and molecular physics came into operation. In such rings, the ion beam is confined by magnetic fields to circulate in a closed orbit, and during storage, it is *merged* ($\theta = 0°$) with an electron beam in one ring section. This setup has several advantages in comparison with the crossed-beams technique as pointed out in the reviews by Larsson [32] and Andersen [33]. The first use of a storage ring as a means to study electron-anion collisions was reported by Andersen and coworkers in 1995, who studied electron-impact detachment of D^- [34]. The high-quality data clearly demonstrated that the storage ring combined with the merged-beams technique was a powerful tool for measuring the energy dependence of cross sections for electron induced reactions in the threshold region. Since then, a number of experiments have been carried out mainly at the storage rings ASTRID in Aarhus and CRYRING in Stockholm. Several atomic anions have been studied [10, 34–41] along with diatomic anions [11–13, 42–45] and small polyatomic negative ions [21, 46–50]. Moreover, the appearance of electrostatic storage rings [51] and ion traps [52, 53] have made it possible to study large molecules like DNA building blocks [54, 55] and other heavy, large molecules [56–58]. It should also be mentioned that experiments concerning electron collisions with *multiply charged* negative ions have been reported [55, 59].

Needless to say, a lot of information is contained in all these experiments, and only the main features will be stressed here. It was established that the detachment cross section is characterized by an effective threshold 2–3 times larger than the electron binding energy. As explained in Sec. 2.2, this effect can be accounted for by the Coulomb repulsion in the incoming channel, which the projectile electron must overcome to cause detachment. Furthermore, the detachment cross section has a smooth energy dependence, which is expected due to the non-resonant character of the process. For molecular anions, electron impact can also induce dissociative reactions, but for small anions — with only a few exceptions [12, 13, 50] — pure detachment is still observed to be the dominant process. Finally, a comparison of the detachment cross sections for the various types of ions reveals that the cross section shapes are remarkably similar, even when atomic anions are compared to large biomolecules.

Over the years, also the threshold behavior of the photodetachment cross section of anions has been studied intensively [60], and in the threshold region, the Wigner law [61] provides a good description of the cross section. But whereas the threshold behavior for detachment by photon impact is well-understood, this is not the case for detachment by electron impact. As compared to photodetachment, the situation for electron impact detachment is far more complex, since there are at least three species in the final state as opposed

to only two in the case of photodetachment. Moreover, the famous Wannier theory [62] describing the threshold behavior for single ionization of neutrals or positive ions by electron impact is not applicable to negative ions, since the residual is a neutral species rather than a positive ion.

Detachment by electron impact is a process very difficult to handle theoretically due to the necessity of describing two continua, and correlations between the two free electrons in the final channel complicate things even further. Most of the early theoretical studies concentrated on describing the cross section in the high energy range, where variations of the Born approximation are applicable [63–69]. Inherently, these calculations are of limited validity in the near-threshold region. As the first, Hart and coworkers [70] investigated the cross section in the threshold region by making use of only general properties of the three-particle wave function outside a finite reaction zone. Unfortunately they did not realize the importance of an effective threshold. Most other calculations make use of two-electron models where only the incident and target excess electron are taken into account. These models can be divided into three subgroups: *classical* models [71, 72] in which both electrons are described classically, *semiclassical* calculations [64, 73–76], which treat the incident electron classically but the target electron quantum mechanically, and finally full *quantum mechanical* models [77–80], which describe both electrons within the realms of quantum mechanics.

In his classical model, Solov'ev [71] considered that the electric field of the incoming electron perturbs the binding potential of the target excess electron, and over-the-barrier escape becomes possible, if the incident electron comes sufficiently close (see Fig. 2.3). From these considerations, the detachment probability was related to the solid angle through which escape is possible, and the cross section was easily calculated. However, escape can occur at incident electron energies below the classical threshold, as quantum mechanics allows the bound electron to tunnel through the barrier. This approach was taken by Smirnov and Chibisov [64]. They calculated the detachment cross section assuming that the ionic electron tunnels through the barrier, a process very similar to that of electric field ionization [81]. The idea of Ostrovsky and Taulbjerg [73] was to combine the classical over-the-barrier model with quantum tunnelling. They considered classical escape to be dominating at small distances between the projectile and the bound electron, while the tunnelling process was assumed to be important only at larger distances. Whereas the tunnelling theory was identical to that of Smirnov and Chibisov, Solov'evs classical model was substantially amended. Here, Ostrovsky and Taulbjerg introduced the concept of decay rate to account for the fact that the bound electron does not escape immediately, even if the reaction condition is fulfilled. Individually, the two models cannot account for the measured cross sections, but the new model is able to describe the near-threshold region of

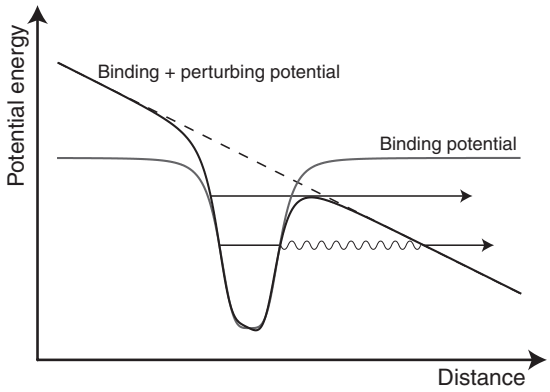

Figure 2.3: Illustration of the detachment process. Shown is the binding potential and the potential resulting from the perturbation caused by the electric field associated with the incoming electron. Escape over-the-barrier and by tunnelling are sketched.

the detachment cross section to some extent. Nonetheless, the range of validity seems rather limited (see Ref. [73] for comparison of the three models and the data). A similar simple semiclassical model is that of Kazansky and Taulbjerg [74], which is based on a non-stationary quantum wavepacket study. The wave function of the bound electron is propagated in time during the collision with the classical electron, and the detachment probability is subsequently related to the overlap integral between the initial and final state wave functions. The shape of the simulated cross section turned out to be in good agreement with experimental results, however, the calculated absolute magnitude was somewhat lower than the experimental one. Lin and coworkers [75] obtained good agreement with experiments by employing standard close-coupling theory to describe the bound electron within the framework of quantum mechanics. Using lowest-order distorted-wave theory, Pindzola [77] calculated the detachment cross section for H^- and O^- and obtained results that compared very nicely with the experimental data for the latter. Nevertheless, this was considered to be somewhat fortuitous as the calculations indicated that strong correlation effects between the incident electron and the target were present as also noted by Kazansky and Taulbjerg [74]. Therefore it was concluded that higher-order perturbational methods probably were needed in order to describe the process properly.

Inspired by the Wannier theory [62], Rost derived an analytic expression for the detachment cross section [76]. In this model, the cross section is decomposed into a product of a background part (a slowly varying contribu-

tion) and a part containing the dominant energy dependence. The latter part is attributed to tunnelling of the outgoing electron pair through the Coulomb barrier, and, in analogy with Wannier's assumptions, the electrons are considered to escape back-to-back. The threshold detachment probability is then obtained by calculating the action along the classically forbidden two-electron orbit. The analytic expression was compared to the experimental data for D^-, B^-, and O^- and the agreement was found to be very good indeed.

A completely different method was employed by Robicheaux [79, 80]. He realized that the correlation between the two electrons in the final channel is merely an artifact of using an unsuited coordinate system. Hence, the initial and final state wave functions were described in two different coordinate systems to suppress correlations related to the choice of coordinates. The cross section was expressed in terms of the so-called T-matrix elements, which were calculated and summed for 10–20 partial waves. This procedure yielded results that were in excellent agreement with the experimentally determined cross sections for H^- and B^-. Also the differential cross sections were calculated by Robicheaux, and they were later confirmed by time-dependent close-coupling theory calculations by Pindzola and Robicheaux [78], thereby providing a solid confirmation of both sets of results.

More recently, a formalism originally developed for calculations of electron impact ionization cross sections of neutral and positive targets was extended to negative atomic ions by Deutch [82]. Experimental data for H^-, B^-, C^-, and F^- were used to determine empirical parameters required for the application of the formalism. With these parameters at hand, the detachment cross section of O^- was calculated and found to be in fair agreement with the experimental data. Moreover, the detachment cross section of Li^- was calculated, but unfortunately it was not compared to the available experimental data of which the authors were unaware.

By now, it seems that detachment cross sections of *atomic* anions can be described quite accurately by theory, and especially the recent full quantum mechanical calculations show astonishingly good agreement with the experimental data. However, most of the models presented above rely on numerical simulations that depend on the specific target, and they are therefore not easily compared to new experimental data on other species. In addition, the semi-classical and quantum mechanical descriptions assume the target excess electron to be weakly bound which is not necessarily the case when *molecular* anions are considered. For the molecular species, also the possibility of, for example, nuclear rearrangement needs consideration, which further complicates the picture.

In need of a simple analytic expression that might be used to describe the near-threshold behavior of non-resonant detachment cross sections, a simplistic classical model has been introduced by Andersen [34]. It turns out that the

simple model is actually able to give a fair description of the detachment cross section for both atomic and polyatomic anions. The 'reaction zone' model assumes that detachment occurs with constant probability p once the projectile electron is within a distance R_{th} of the anion. Assuming that the incoming electron experiences a purely repulsive Coulomb potential, the distance of closest approach $D(\rho)$ becomes (in atomic units):

$$D(\rho) = \frac{1}{2E} + \sqrt{\left(\frac{1}{2E}\right)^2 + \rho^2}, \tag{2.5}$$

where ρ is the impact parameter, and E is the energy of the incoming electron. The non-resonant cross section is then calculated according to:

$$\begin{aligned} \sigma_{\text{NR}} &= 2\pi \int_0^\infty \rho \mathrm{d}\rho \begin{cases} p & D(\rho) \leq R_{\text{th}} \\ 0 & D(\rho) > R_{\text{th}} \end{cases} \\ &= p\pi R_{\text{th}}^2 \max\left[0, \left(1 - \frac{E_{\text{th}}}{E}\right)\right], \end{aligned} \tag{2.6}$$

where the classical threshold energy for detachment, $E_{\text{th}} = 1/R_{\text{th}}$ (in atomic units), has been introduced. This simple model has been successful in describing the near-threshold behavior of detachment cross sections for both atomic and molecular anions [10, 11]. Some anions exhibit deviations from the model below the threshold energy where the measured cross section has a smoother onset than predicted by the classical expression of Eq. (2.6). This effect is ascribed to the tunnelling of the target electron out of the binding potential. As the reaction zone model is purely classical, it does not include tunnelling effects. The model cross section by Ostrovsky and Taulbjerg [73] including tunnelling effects does indeed have a smoother onset in better agreement with experimental data near the threshold energy. Still, the reaction zone model provides a better overall description of measured cross sections [10].

In Chaps 4–6 where experimental results of electron-impact detachment from various anionic clusters are presented, the shape of the detachment cross sections is discussed with the 'reaction zone' model as the starting point.

2.3.2 Dianions

It is well-known that doubly charged negative ions, dianions, like SO_4^{2-} and CO_3^{2-} exist in solutions and solids. In spite of this fact, these ions are not stable as isolated entities in the gas phase [83–85]. The reason is the large Coulomb repulsion between the excess electrons which renders the small dianions unstable against spontaneous emission of an electron (*autodetachment*)

or dissociation into two monoanionic fragments (*Coulomb explosion*). The stability of small dianions in the condensed phases is provided by interactions with solvent molecules or counterions. Hence bringing the species into the gas phase, where the stabilizing effects of the surrounding media are absent, causes the small dianions to spontaneously break apart. In larger molecules, the additional charges can be spatially separated, and consequently the electrostatic repulsion decreases. Therefore it is not surprising that large dianions may exist as *stable* entities in the gas phase.

The properties of dianions, be it stability or structure, are extremely challenging to describe theoretically due to the large amount of electron correlation and the diffuse character of the excess electrons. As mentioned above, the metastable and unstable states of small dianions may decay by autodetachment or dissociation, which further complicates the theoretical investigation of such species. For reviews of dianion research, Refs [17, 86–88] should be consulted.

Over the years, the existence of stable and unstable atomic dianions has been a matter of some controversy on both the experimental and the theoretical side. Being the smallest dianion of all, H^{2-} has attracted special attention. In the 1970s, Peart and coworkers observed structures in the electron-impact detachment cross section of H^- which were attributed to the formation of short-lived (that is, $\tau < 10^{-7}$ s) states of H^{2-}. The two states were located at 14.5 eV and 17.2 eV above the ground state of H^- [26–28] with resonance widths corresponding to lifetimes in the order of 10^{-15} s. From their calculations, Thomas and Taylor classified the states as $(2s)^2(2p)\ ^2P$ and $(2p)^3\ ^2P$, respectively [89, 90]. Moreover, Schnitzer and Anbar reported that they had detected states of H^{2-} and D^{2-} with half-lifes of 23 ns in a tandem mass spectrometer [91–93]. Two decades later, Robicheaux and coworkers questioned the existence of such unstable states of H^{2-}. They emphasized that the results of Peart and Dolder contradicted a proof by Simon [94] stating that a many-particle system, which experiences purely Coloumbic forces, cannot exist at energies above the threshold for complete disintegration, which in the case of H^{2-} is $13.6 + 0.75 = 14.35$ eV above the ground state of H^-. Furthermore, they argued that the assignment of the H^{2-} to be of ^2P character would violate the unitarity of the collision matrix, and finally, their two independent *ab initio* calculations did not show any evidence of resonant states of H^{2-}. The conclusion of the investigations was that the reported resonance by Thomas and Taylor was a mere artifact of a too small basis set. These results were followed by three independent electron-impact detachment experiments [34, 35, 41], neither of which displayed structures in the cross section, thereby supporting the investigations by Robicheaux. More recently, the existence of $2p^3\ ^4S$ resonance states of H^{2-} has been debated [95–98]. The prediction of these states is not in contradiction with experiments, as the transition to a ^4S state of H^{2-} from the

^{1}S ground state of H^- is spin forbidden. To populate the ^{4}S states in electron scattering experiments would require starting from the $2p^2$ ^{3}P excited state of H^-, but this state has never been observed. Clearly, the question whether resonance states of H^{2-} exist or not is not yet resolved.

Other atomic dianions stable on the µs timescale have been reported in mass spectrometry [99, 100], but the claims could not be reproduced or showed to be flawed (see Refs [101–103] and references therein). The nonexistence of *bound* or *long-lived* ($\tau \geq 10^{-7}$ s) atomic dianions now seems to be a well-established fact [17, 104]. As for H^{2-}, predictions of short-lived resonance states of atomic dianions as O^{2-}, S^{2-}, B^{2-}, and Al^{2-} (see Refs [105, 106] and references therein) have been made, but for the three first species no sign of dianion formation was observed in electron scattering experiments [10, 36, 40]. According to the theoretical calculations, the atomic dianions decay into a free electron and the atomic monoanion, and hence the dianionic states, if existing, are not revealed in the detachment cross section, which is measured in the scattering experiments. To date, unstable atomic dianions have never been observed experimentally even though theory predicts the presence of such states. Hence the existence of short-lived states remains an open question, whereas there is consensus that bound and long-lived states are non-existing.

Turning to molecular dianions, no stable or long-lived di- or tri-atomic gas-phase dianions are known. Theoretically, it has been concluded by Boldyrev and Simons, that diatomic and linear triatomic dianions are unstable with respect to electron loss [107]. However, unlike the case of atomic dianions, both theoretical and experimental evidence for the existence of short-lived resonance states of di- and tri-atomic dianions have been reported. Among the small unstable dianions studied are systems such as C_2^{2-} [42, 107–109], B_2^{2-} [11, 43], BN^{2-} [11, 110], NO_2^{2-} [21], and CN_2^{2-} [111].

The first long-lived doubly charged negative ion to be experimentally observed in the gas phase was benzo[cd]-pyrene-6-one ($C_{19}H_{10}O^{2-}$) in 1969 [112]. Two decades passed before the existence of a gas-phase dianion consisting of fewer than twenty atoms was reported by Schauer and coworkers who in their mass spectrum identified carbon cluster dianions as small as C_7^{2-} [113]. This observation triggered a search for the smallest stable or long-lived isolated dianion both among theoreticians and experimentalists. From theoretical considerations it was concluded already in 1991 that the earth alkaline tetrahalides MX_4^{2-} (M = Be, Mg or Ca; X = F or Cl) [114, 115] are electronically stable, but unstable with respect to dissociation. However, the lifetime was expected to be long due to the presence of the Coulomb barrier inhibiting dissociation. Indeed, in 1999, this class of dianions was seen in mass spectra by Klein and Middleton [116]. Meanwhile, the focus was turned to the alkaline trihalides MX_3^{2-} (M = Li, Na or K; X = F or Cl) and particularly LiF_3^{2-} which

Scheller and Cederbaum suggested as a possible candidate for the smallest dianion [85, 117]. Also this species is energetically allowed to dissociate, but with a lifetime in the order of 10^{11} years [117] the dianion is essentially stable. Only recently was the LiF_3^{2-} discovered experimentally [118]. In terms of the number of atoms, this dianion is the smallest known, but in fact not in terms of mass. So far, the lightest species that has been discovered experimentally is BeC_4^{2-} [119], which was found in 1999. Most likely, the system is unstable with respect to electron autodetachment, but it exhibits a long lifetime due to the presence of the Coulomb barrier [120]. In contrast to LiF_3^{2-}, which is bound mostly electrostatically, BeC_4^{2-} is covalently bound. Finally, it should be mentioned that the smallest truly bound dianion to be observed so far is OC_5^{2-}, which was found by Gnaser and coworkers in 2002 [121]. Refs [17, 86, 88] provide more extensive reviews of the investigations of long-lived and stable gas-phase dianions.

Experimental studies of the intrinsic properties of dianions were first conducted by Wang and coworkers using photodetachment photoelectron spectroscopy [19, 20]. Their studies presented the first conclusive experimental evidence for the existence of the repulsive Coulomb barrier which at that time had already been inferred by several authors [16–18]. The experiments revealed that photons of energies considerably larger than the binding energy were needed to detach the excess electron. This fact could only be accounted for by the existence of a barrier. Even photoelectrons with more kinetic energy than the incoming photon were observed [122], an observation only possible if the binding energy is negative. In the latter case, the electrons are trapped behind the Coulomb barrier, and the lifetime of the anion is governed by tunnelling through the barrier.

As mentioned above, dianions are commonly found in solids and in solutions, since they are stabilized in these condensed phases through interactions with counterions or solvent molecules. To elucidate the influence of counterions on the properties of stable and unstable dianions, Wang and coworkers have studied free singly and doubly charged alkali metal sulfate ion pairs, $M^+(SO_4^{2-})$ and $[M^+(SO_4^{2-})]_2$ (M = Na, K) [123]. Experimental evidence was given that the complex can be considered as a distorted free SO_4^{2-} interacting electrostatically with the alkali metal cation. Further, the presence of the counterion was found to stabilize the dianion by several eV [123].

The effect of surrounding water molecules have also been addressed by the Wang group. They investigated the sequential hydration of several dianions, and have thus provided the first direct information on how the electronic stability changes as a function of solvation [84, 124–127]. It was observed that each of first few water molecules increases the electron binding energy by roughly 0.6 eV, and that further addition of water molecules successively

stabilizes the dianion, even though the stepwise increase in binding energy becomes smaller. For a review on photoelectron spectroscopy on dianions, Refs [87, 128] should be consulted.

2.4 Open questions

The investigations outlined in the preceding section have indeed been essential for obtaining an understanding of the electron-anion collision process and of the properties of small doubly charged anions. To summarize, the key observations concerning the electron-induced fragmentation processes were:

- The cross section for electron-induced detachment exhibits a characteristic shape, which is well-described by a classical model cross section.
- The threshold energy for electron-induced detachment is 2–3 times larger than the electron binding energy.
- For most systems, the dominant process is pure detachment.
- For some molecular ions, structures due to the formation of transient dianions are visible in the cross section.

With these observations, many of the initially unclear points concerning the electron-anion collision process were clarified. However, there are still interesting questions that deserve an answer.

Since only a few of the molecular anions studied prior to this work contained more than two atoms, the route followed here is to investigate the effect of molecular size on the different aspects of electron-induced reactions. To be more specific:

- Does the detachment cross section change shape for more complex molecular ions?
- How does the size of the system influence the properties of resonant dianion states?
- What influence do water molecules have on the properties of resonant dianion states?
- What is the fragmentation pattern of weakly-bound — as opposed to covalently-bound — anions?

These questions are addressed in the following chapters.

CHAPTER 3

Experimental techniques

In the following, the experimental techniques that are employed in this work for studying electron-anion collisions are presented. The chapter begins, as all these experiments do, with ways to produce various ions, and in particular two different types of ion sources are introduced. Subsequently, the experimental setup at ASTRID along with the ASTRID storage ring itself are described followed by a section on how cross section and branching ratio measurements are conducted. The last part of the chapter gives an introduction to the ELISA storage ring and the experimental setup used at this ring to study electron-anion collisions. A description of the experimental procedures at ELISA concludes the chapter.

3.1 Ion production

A large variety of ion sources exists, and the working principles of one source can be quite different from that of another. None of the sources are universal, but rather each of them is characterized by being designed to produce specific types of ions. Thus, some ion sources are useful for producing negative but not positive ions, some are able to produce ions from gaseous materials but not from solids, while still others are suited to bring large biomolecules into the gas phase.

To produce the ions studied in the present work, two different ion sources have been used, and they are the subjects of interest for the remainder of this section.

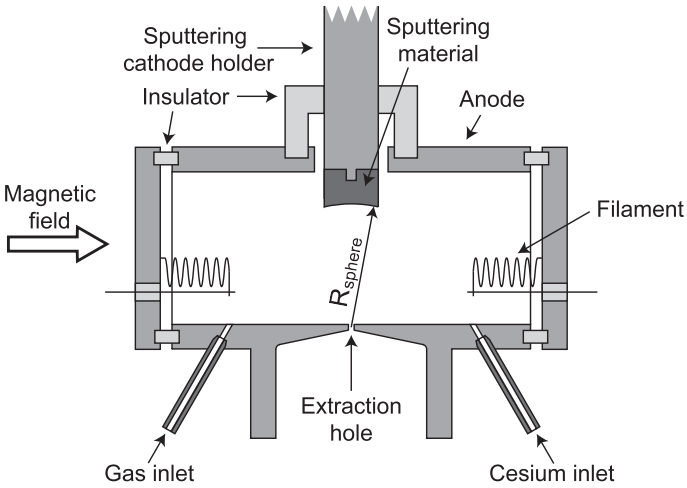

Figure 3.1: Schematic drawing of the discharge chamber in the Aarhus Negative Ion Source.

3.1.1 The Aarhus Negative Ion Source

In the early 1970s, Middleton designed an ion source which he described as being *close to universal* [129]. The source was a sputter source capable of delivering high intensity beams (several µA) and was especially useful for producing ions from solids. Inspired by the work of Middleton, the working principles of the Aarhus Negative Ion Source (ANIS) [130, 131] are essentially the same as the Middleton source, however the design is different.

The general idea of a sputter source is to produce the desired anions from a solid sample by bombarding the sample with suitable cations (here Cs^+). This process takes place in the heart of the ANIS source, which is the discharge chamber sketched in Fig. 3.1. Two filaments connected in series are placed in the chamber, one at each end, and during normal mode of operation a current of ∼40 A is supplied to these. Not only do the filaments heat up the discharge chamber to ∼500 °C, but the surrounding source housing is heated as well. Through contact with the hot housing, a cesium oven located below the discharge chamber is heated to 100–130 °C, which leads to evaporation of cesium from the reservoir. Using a thermocouple, the oven temperature can be monitored to control the cesium consumption, and, if needed, the oven can be heated even further by a third filament. When the cesium vapour enters the discharge chamber it is ionized by the electrons emitted from the hot filaments, and a plasma is formed. The plasma is confined by a magnetic field transver-

sal to the beam direction. The Cs^+ ions are accelerated to a cathode containing the solid sample, and as the cathode is kept at high voltage (typically -2 to -3 kV), the energetic ions sputter material from the cathode surface upon impact. On the cathode surface a layer of cesium is formed from which the sputtered neutrals or ions capture electrons through charge-transfer processes. This effect drastically increases the negative ion yield as seen by Krohn [132]. The end of the cathode has a concave shape of radius R_{sphere} which serves to focus the repelled negative ions onto the outlet opening opposite the cathode. Due to the focusing effect, the distance between the cathode and the outlet has a tremendous effect on the output intensity [131], which attains its maximum at the distance R_{sphere}.

If the desired ions cannot be produced by the use of solids alone, gases can be supplied through an inlet. By introducing a gas into the discharge chamber, the chemical composition of the plasma is changed, thereby leading to the production of different ion species. This option of combining the use of solid and gaseous materials is one of the great advantages of the source, which makes it close to universal.

The drawback of the source lies in the limited time of operation before maintenance. After some days of use, the cathode sample might be sputtered away and needs to be renewed. For that purpose, the source is equipped with an air-lock valve which offers the possibility of changing the cathode without breaking the vacuum. If, instead, the oven runs out of cesium, the source must be vented in order to remove the oven for reloading. This is a lengthy procedure since the filaments usually require outgassing after exposure to air. Finally, the filaments are worn down by continuous operation leading to an increase in resistance. Hence, the power deposited in the source increases for fixed current, and this might cause overheating of the source. In the end, the filaments must be replaced, which involves taking apart the entire source. The durability of the filaments is very dependent on whether or not a gas is supplied to source, and, if so, which type of gas is used. However, during operational periods of one to two weeks only the cathode and occasionally the cesium oven need attention.

When chances are that the desired anions most easily can be produced from a solid or from a combination of solid and gaseous materials, the sputter source is employed, but due to its drawbacks, other sources — e.g. the one described below — present better alternatives for ions that can be produced using only gases.

3.1.2 The Cold Cathode Ion Source

An ion source that works extremely well with gases is the Cold Cathode Ion Source. This source is a hollow-cathode glow discharge source and is one of

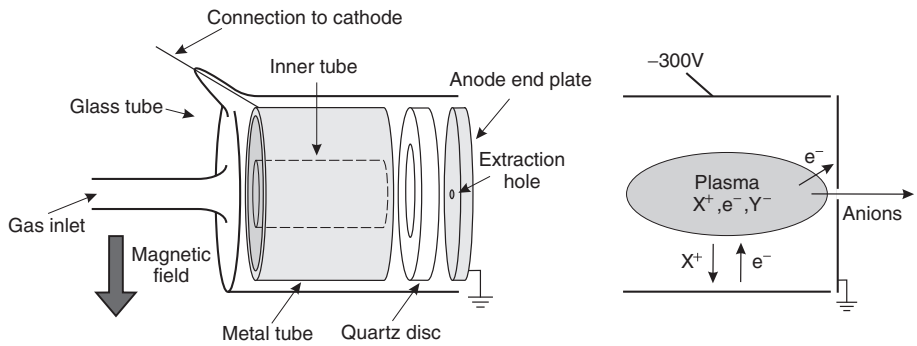

Figure 3.2: Schematic drawing of the cold cathode glass ion source (left) and the working principle (right).

the simplest ion sources that can be made. As seen in Fig. 3.2, the source consists of only very few parts. The outer part of the source is a glass tube which is open at one end and closed at the other except for a small nozzle serving as a gas inlet. Inside the glass housing a cylindrical metal electrode is placed, which can be connected to an external supply by a wire leading through the glass. Furthermore, the electrode is in contact with a smaller coaxial metal cylinder allowing for tighter plasma confinement, and the small cylinder serves as the hollow cathode. By use of a quartz disc, these electrodes are electrically isolated from the front of the accelerator onto which the source is mounted. The high pressure (order of several mbar) region of the ion source is separated from the vacuum of the accelerator (10^{-5}–10^{-4} mbar) by a metal plate with a small orifice which allows for ion extraction. This plate also serves as an anode connected to platform ground. A gas is supplied through the gas inlet, and the pressure is controlled by a needle valve.

When the cylindrical electrode is on negative potential relative to the front of the source, free electrons initially present in the ion source are accelerated from the hollow cathode to the front of the source. On their way, electron-ion pairs are created through collisions with neutrals. Positive ions formed in these reactions are accelerated in the opposite direction, causing the emission of more electrons as they bombard the cathode. If the generation of electron-ion pairs is sufficient to make up for the loss to the electrode and the walls of the source, a stable plasma is formed inside the inner cathode cylinder. As the ion mobility is much smaller than the electron mobility, a sheath of positive space charge emerges between the cathode and the plasma. The potential of the essentially charge-neutral plasma is close to that of the anode, a fact also stemming from the different mobilities μ of electrons and ions: the resistance

R_+ ($\propto 1/\mu_e$) between the plasma and the anode is much smaller than the resistance R_- ($\propto 1/\mu_i$) towards the cathode, since the former is determined by the higher electron mobility. Hence, a substantial fraction of the potential applied between the cathode and anode appears across the cathode sheath region [133, 134]. The applied voltage is roughly −300 V, and consequently the voltage drop from the plasma to the cathode is sufficiently large to accelerate the secondary electrons emitted from the cathode to high energies. Upon entering the plasma, the energetic electrons efficiently cause ionization of atoms and ions. As a result of the potential difference between the plasma and the anode, the negative ions present in the plasma are extracted through the small hole in the anode plate. In order to prevent simultaneous extraction of electrons, a magnetic field transversal to the direction of extraction is applied by placing a magnet outside the source. The field causes electrons to be deflected away from the outlet opening whereas the much heavier anions are only little influenced.

The source is very easy to run and essentially only two parameters are needed for optimization: the ion source pressure and the discharge current. Stability and long time use (several weeks) without any maintenance are some of the source characteristics which often make it the first choice for anion production.

3.2 The merged-beams setup at ASTRID

The experimental studies of electron-ion collisions presented in Chaps. 4 and 5 of this thesis were carried out at the Aarhus STorage RIng, Denmark (ASTRID). In the ring, ions are stored at high energies (MeV) and during storage they are merged with an electron beam in one of the ring sections. The electrons are provided by an electron cooler device capable of producing an intense beam of electrons with a narrow velocity distribution. The following sections serves as an introduction to these two main experimental ingredients, the ASTRID storage ring and the electron cooler. The latter is described with emphasis on how to obtain high energy resolution in experiments.

3.2.1 The ASTRID storage ring

The ASTRID storage ring is a dual-purpose device, which can be used for electron as well as ion storage [135, 136]. During electron storage, the ring serves as a source of synchrotron radiation, which is of use to experiments covering a wide range of scientific fields (see Ref. [137] for more information on synchrotron radiation research at ASTRID). When used for either positive or

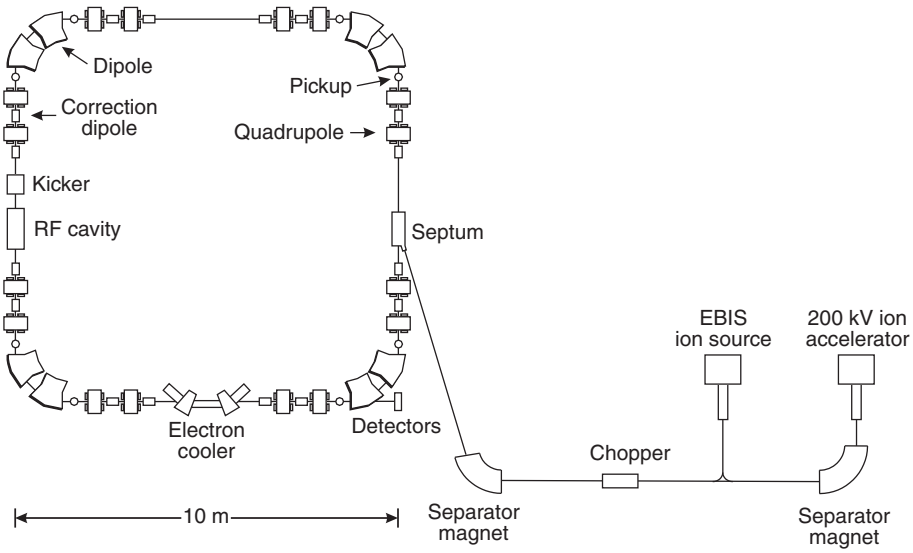

Figure 3.3: Schematic drawing of the ASTRID heavy-ion storage ring with the injection beamline.

negative ion storage, electron-ion collisions and proton dosimetry with special attention on cancer therapy are the main research topics.

ASTRID is shown schematically in Fig. 3.3. It has a square geometry with a circumference of 40 m. Each of the four corners consists of two 45° dipole magnets, and the straight sections are equipped with quadrupole magnets for focusing purposes and correction dipole magnets for final beam positioning. Furthermore, in each straight section two sets of pickup electrodes are placed, which are used to monitor the ion beam position in the ring. Various ion sources can be mounted at the accelerator platform where ions of charge, $Q{\cdot}e$, (Q being either positive or negative) are produced, extracted and pre-accelerated to an energy of usually $150{\cdot}|Q|$ keV. In order to single out a particular ion of those produced in the source, the ions are mass-to-charge analyzed by a separator magnet. Hence, merely ions of a given mass-to-charge ratio are guided through the beam line beyond the magnet. Further downstream, a chopper allows a beam pulse with a spatial length corresponding to the ring circumference to pass while the remaining ions are deflected away from the beam. After passing the chopper, the beam pulse reaches another separator magnet and then the septum magnet, which injects the ion bunch into the ring. An electrostatic kicker placed opposite the septum deflects the ions into a closed orbit in the ring thus leading to storage (single turn injection). Sub-

sequently, the stored ions are bunched by means of a radio-frequency (RF) system where the frequency is set to an integer multiple, n, of the revolution frequency, thereby producing n ion bunches (a typical number is 18–25). To accelerate the ions to final energies of order MeV, the RF is then ramped up synchronously with the magnetic fields in the dipole and quadrupole magnets. The maximum momentum p_{max} attainable for a given ion is determined by the magnetic rigidity, $B \cdot R$=1.93 Tm, where B is the maximum magnetic field strength obtainable by the magnets and R the radius of curvature of the ring lattice. p_{max} is found by equating the Lorentz force, $QevB$, with the relativistic centripetal force, pv/R, (p being the relativistic momentum and v the velocity), and hence the maximum kinetic energy is:

$$\begin{aligned} E_{\mathrm{kin}}^{\mathrm{max}} &= \sqrt{p_{\mathrm{max}}^2 c^2 + M^2 c^4} - Mc^2 = \sqrt{(QeBRc)^2 + M^2 c^4} - Mc^2 \\ &= 931.5 \left[\sqrt{0.3858 Q^2 + M^2} - M \right] \text{ MeV}, \end{aligned} \tag{3.1}$$

where M the ion mass in atomic mass unit (amu) and c the speed of light. In practice, however, this maximum kinetic energy was for a long time not achievable due saturation effects in the dipole magnetic fields. These effects complicated the synchronous ramping of the quadrupoles with the dipoles thus making it extremely difficult to reach the maximum energy. Recently, the ramping procedure was facilitated by employing the result of measurements, which mapped out the current vs magnetic field characteristics of the dipole and quadrupole magnets. Hence, the limit set by Eq. (3.1) is now feasible.

The ion beam lifetimes at these high energies are determined by charge-changing collisions with residual gas in the ring. The mean pressure, maintained by more than 40 vacuum pumps, is in the low 10^{-11} mbar region, which results in typical lifetimes of a few seconds for molecular ions.

The acceleration of ions in the ring makes it possible to store virtually any ion, positive or negative, provided that a reasonable beam current can be extracted from the ion source. However, as the acceleration procedure takes a few seconds, it is difficult to study electron collisions with short-lived ion species.

3.2.2 The electron cooler

The electron target for collision experiments is provided by the electron cooler mounted in one of the straight sections in the ring (see Fig. 3.3). Figure 3.4 shows a sketch of the electron cooler device. The electron beam is produced in the gun and transported by magnetic fields to the interaction region where it is merged with the ion beam. After the 0.95 m-long overlap section, the electrons are separated from the ions by deflecting them into a collector.

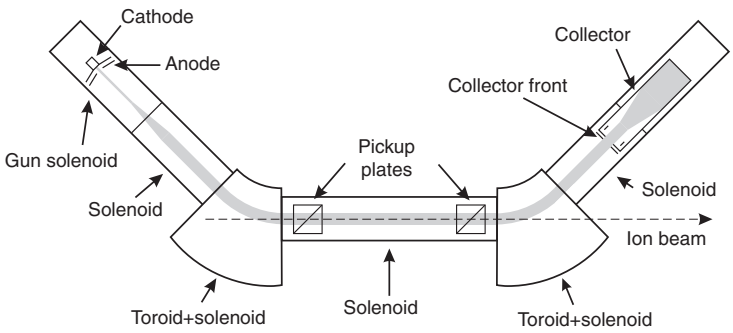

Figure 3.4: Schematic drawing of the electron cooler at ASTRID. Electrons created at the cathode are accelerated to the anode from where they are guided through the interaction region and into the collector by magnetic fields.

The name 'cooler' refers to the fact that the electron cooler device can be used to phase-space cool the ion beam. On each roundtrip in the ring, the ions are passed through the cold electron beam travelling at the same mean velocity as the ions. Going through the interaction region, the ions undergo Rutherford scattering by the electrons. In this process, heat is exchanged between ions and electrons through Coulomb interactions, and the continuously renewed electron beam thus serves as a heat reservoir for the ions. The result is a reduction of the ion velocity spread in all three spatial directions. For an elaborate discussion of the subject, Ref. [138] should be consulted.

In the present work, the electron cooling technique was not employed, since the molecular systems under investigation were too heavy to allow for phase-space cooling on a reasonable timescale. Therefore, the electron cooler merely served as a means of producing an intense electron beam of well-defined energy.

The electron beam is produced in the electron gun, which has a modified Pierce geometry [139]. The cathode is a 1 cm diameter BaO coated tungsten cathode, which emits electrons through thermionic emission when heated to ∼1200 K. The electrons are accelerated from the cathode kept at negative potential V_{cath} towards a grounded anode grid with a transmission of ∼80%. The extracted electron current I_{e} is space-charge limited and relates to the cathode potential through Child's law [140]:

$$I_{\text{e}} = PV_{\text{acc}}^{3/2}. \tag{3.2}$$

Here, $V_{\text{acc}} = -V_{\text{cath}}$ is the acceleration voltage (10–2000 V). The constant, P, is the perveance determined by the geometry of the electron gun. For an electron

beam of radius, R_e, and a cathode-anode distance of d, the perveance can be expressed as [140]:

$$P = \frac{4}{9}\pi\epsilon_0\sqrt{\frac{2e}{m_e}}\left(\frac{R_e}{d}\right)^2, \tag{3.3}$$

where m_e is the electron mass and ϵ_0 the permittivity of free space. The distance between the cathode and anode can be changed from outside the vacuum chamber, thus allowing for some control of the current. During the experiments described here, the current is typically in the order of a few mA.

The space charge potential

After acceleration, the electrons enter a drift region where they are transported to the merging section. In this region, the central electrons within the cylindrical beam move slower than the outer ones as the latter shield the ground potential of the surrounding vacuum chamber. This fact has a non-negligible effect on the electron energy in the laboratory frame, E_e^{lab}, which is given by:

$$E_e^{lab} = \frac{1}{2}m_e v_e^2 = e(V_{acc} + V_{sp}). \tag{3.4}$$

Here, v_e is the electron velocity and V_{sp} the negative space charge potential due to presence of the electrons. The electron beam is represented by a charge distribution of uniform number density, n_e, and with sharp boundaries [141]. The distribution has a cylindrical symmetry and is surrounded by the coaxial cylindrical vacuum chamber, which is grounded. The potential resulting from this configuration is found analytically by solving the Poisson equation or by employing Gauss's law (see appendix A), which leads to the following expression:

$$V_{sp}(r) = \frac{en_eR_e^2}{4\epsilon_0}\left[2\ln\left(\frac{R_e}{R}\right) + \left(\frac{r}{R_e}\right)^2 - 1\right], r < R_e\,. \tag{3.5}$$

R and R_e are the radii of the vacuum chamber and the electron beam, respectively. As seen, the potential, and hence the electron energy, depend on the distance r from the center axis. If the electron current, $I_e = en_e\pi R_e^2 v_e$, and E_e^{lab} are introduced instead of the number density, n_e, and the electron velocity, v_e, a simplified expression for $V_{sp}(r)$ is obtained:

$$V_{sp}(r) = -K_{sp}(r)\frac{I_e}{\sqrt{E_e^{lab}}}\,. \tag{3.6}$$

Here, $K_{sp}(r)$, is a positive factor purely dependent on the geometrical parameters and the position in the electron beam (see Eq. (A.11)).

In the interaction region, the ion and electron beams are aligned to a good approximation. The radius of the electron beam is $R_e = 1.06$ cm, and the radius of an uncooled ion beam is $R_i \approx 0.5$ cm [142]. Due to the finite ion beam size, the ions will interact with electrons at different radii and hence experience different electron energies. This effect contributes to the energy resolution in the experiment as discussed on p. 36, although it is not necessarily the limiting factor. Nonetheless, the average electron energy of electrons interacting with the ion beam can be found by integrating the space charge potential over the extent of the ion beam and subtracting this potential from the acceleration voltage. The result is:

$$E_e^{lab} = e\left(V_{acc} - K_{sp}^{eff}\frac{I_e}{\sqrt{E_e^{lab}}}\right), \tag{3.7}$$

where K_{sp}^{eff} is a constant obtained by averaging $K_{sp}(r)$ over the ion beam. The constant is called the space charge constant, and from the above equation, it is evident that K_{sp}^{eff} must be known in order to calculate the electron energy. The space charge constant can be determined experimentally as described below.

In electron-collision experiments, the measured quantity is the cross section mapped out as a function of the collision energy (also referred to as the relative energy). For parallel electron and ion beams, the relative energy, E_{rel}, is defined as:

$$E_{rel} = \frac{1}{2}m_e(v_e - v_i)^2 = \left[\sqrt{\frac{m_e}{M_i}E_i} - \sqrt{E_e^{lab}}\right]^2, \tag{3.8}$$

where M_i and E_i are the ion mass and energy. The relative energy is changed by varying the electron energy while keeping the ion energy fixed. The measurable quantities are V_{acc}, E_i and I_e, and as Eq. (3.7) must be solved to find E_e^{lab}, it is necessary to know K_{sp}^{eff} in order to calculate the collision energy. However, there are two ways of obtaining a certain relative energy: either the electrons are faster than the ions ($v_e > v_i$) or the other way around ($v_e < v_i$). Clearly, the cross section for a given reaction is independent of which species is faster, and hence measurements of the cross section for $v_e > v_i$ must be identical to those for $v_e < v_i$. The requirement that the cross section is symmetric around $v_e = v_i$ allows K_{sp}^{eff} to be determined and thereby making it possible to calculate the relative energies.

Energy resolution

An important parameter in the experiment is the energy resolution. The relative ion energy spread in ASTRID has been measured to be in the order of

10^{-4} [143], whereas the relative laboratory energy spread of the electrons is of order 10^{-2}–10^{-3} due to, for example, acceleration voltage ripple. Since the energy spread of the ions is an order of magnitude smaller, the spread in relative energy is mainly governed by the electrons. Therefore, it is essential to produce an electron beam with a narrow velocity distribution.

When first emitted from the hot cathode, the velocity distribution of the electrons is a thermal three-dimensional Maxwell distribution characterized by the cathode temperature, T_0:

$$f(\mathbf{v}_\mathrm{e}) = \left(\frac{m_\mathrm{e}}{2\pi k T_0}\right)^{3/2} \mathrm{e}^{-m_\mathrm{e} v_\mathrm{e}^2/2kT_0}. \tag{3.9}$$

The cathode temperature is ∼1200 K yielding a mean energy of $\langle E_\mathrm{e}\rangle = 3/2kT_0$ $= 0.16$ eV. However, accelerating the electrons breaks the spherical symmetry of the velocity distribution as the longitudinal (parallel to the beam direction) and transversal (perpendicular to the beam direction) degrees of freedom are affected differently. To the first approximation, the transversal velocity spread is unchanged after acceleration whereas the longitudinal one undergoes a kinematic compression. After the acceleration stage, the velocity distribution is therefore characterized by two different temperatures, a longitudinal temperature, $T_\parallel$, and a transversal one, $T_\perp$. In the frame moving with the average electron velocity, the velocity distribution is described by a flattened Maxwell distribution:

$$f(\mathbf{v}) = \frac{m_\mathrm{e}}{2\pi k T_\perp} \mathrm{e}^{-m_\mathrm{e} v_\perp^2/2kT_\perp} \sqrt{\frac{m_\mathrm{e}}{2\pi k T_\parallel}} \mathrm{e}^{-m_\mathrm{e} v_\parallel^2/2kT_\parallel}, \tag{3.10}$$

where $v_\perp$ and $v_\parallel$ are the transversal and longitudinal velocities in the moving frame. The temperatures are defined according to the equipartition theorem of statistical mechanics stating that the mean value of each independent quadratic term in the energy is equal to $kT/2$ [144]:

$$\begin{aligned} \frac{1}{2}kT_\parallel &= \frac{1}{2}m_\mathrm{e}\sigma_{v_\parallel}^2 = \frac{1}{2}m_\mathrm{e}\left(\langle v_\parallel^2\rangle - \langle v_\parallel\rangle^2\right), \\ \frac{1}{2}kT_\perp &= \frac{1}{2}m_\mathrm{e}\sigma_{v_\alpha}^2 = \frac{1}{2}m_\mathrm{e}\left(\langle v_\alpha^2\rangle - \langle v_\alpha\rangle^2\right), \quad \alpha = x, y, \end{aligned} \tag{3.11}$$

where v_x and v_y are the two transversal velocities relating to $v_\perp$ through the equation $v_\perp^2 = v_x^2 + v_y^2$.

Due to energy conservation, the longitudinal energy spread, σ_E, is constant during acceleration and is therefore equal to the initial spread of $(kT_0)/\sqrt{2}$. When accelerated to an energy, E_0, the relative energy spread of the electrons

is given by σ_E/E_0, which is twice as large as the relative longitudinal velocity spread, $\sigma_{v_z}/\langle v_z \rangle$. Accordingly, the longitudinal electron temperature in the moving frame is found to be [138]:

$$\frac{1}{2}kT_{\parallel} = \frac{1}{2}m_{\mathrm{e}}\sigma_{v_z}^2 = \frac{1}{2}m_{\mathrm{e}}\left(\frac{\langle v_z \rangle \sigma_E}{2E_0}\right)^2 = \frac{(kT_0)^2}{8E_0}. \tag{3.12}$$

Under typical conditions, the expression above results in values of $kT_{\parallel}$ in the order of 0.01 meV, which is orders of magnitude smaller than kT_0. However, another contribution to the longitudinal temperature has to be taken into account. Prior to acceleration, the electrons have some potential energy arising from Coulomb interactions. This energy is left unchanged by the acceleration as the time scale involved is too short for electron interactions to occur. Subsequently, the potential energy is partly converted into kinetic energy thereby influencing the electron temperature, a process known as *longitudinal-longitudinal relaxation*. Hence, the change in potential energy must be added to the longitudinal temperature, which then becomes [138]:

$$kT_{\parallel} = \frac{(kT_0)^2}{4E_0} + C\, n_{\mathrm{e}}^{1/3}, \tag{3.13}$$

where C is a constant. The additional term is estimated to be in the order of 0.1 meV making it in fact the dominant contribution to the longitudinal temperature. Consequently, $kT_{\parallel}$ is essentially independent of the acceleration energy. The longitudinal temperature can be determined experimentally by studying narrow structures in scattering cross sections, and measurements of dielectronic-recombination cross sections yield a temperature of $kT_{\parallel} = 1.0 \pm 0.5$ meV [141].

While the longitudinal temperature is greatly reduced by the acceleration, the transversal temperature is left unchanged as already mentioned. The energy associated with the transverse degrees of freedom is stored in cyclotron motion as the guiding magnetic field causes a spiralling motion of the electrons in the plane perpendicular to the beam direction. Superimposed on this motion is a magnetron motion caused by the transversal electric field arising from the space charge of the electron beam. The energy stored in the magnetron motion is of the order of 0.01–0.1 eV and the transverse temperature is therefore expected to be somewhat higher than the cathode temperature. Reduction of the transversal energy is accomplished by an adiabatic expansion of the electron beam, a method first employed by Danared [145]. The technique relies on the fact that the action integral is an adiabatic invariant [146]. This implies that the magnetic flux through the electron orbit is a constant of motion provided that the magnetic field varies slowly compared to the orbiting frequency of the motion [147]. The magnetic flux, Φ, through a cyclotron

orbit of radius, r_c, is given by:

$$\Phi = B\pi r_c^2, \tag{3.14}$$

where B is the magnetic field strength. In terms of the cyclotron frequency, $\omega_c = eB/m_e$, the kinetic energy contained in the motion can be expressed as:

$$E_c = \frac{1}{2} m_e \omega_c^2 r_c^2 = \frac{e^2 B \Phi}{2\pi m_e}. \tag{3.15}$$

As is evident, the cyclotron energy is linearly dependent on B. Hence, the transversal energy can be diminished by subjecting the electrons to a slowly decreasing magnetic field when travelling from the gun to the interaction region. The kinetic energy is reduced by the adiabatic expansion factor, f_a, defined as

$$f_a = \frac{B_{gun}}{B_{sol}}, \tag{3.16}$$

as is likewise the transversal temperature:

$$kT_\perp = \frac{kT_0}{f_a}. \tag{3.17}$$

As the magnetic flux through a cyclotron orbit is constant, Eq. (3.14) implies that the radius of the orbiting motion increases, and accordingly the electron beam is expanded to a radius of:

$$R_e = R_0 \sqrt{f_a}, \tag{3.18}$$

where $R_0 = 0.5$ cm is the radius of the cathode. In all experiments presented here, the value of the expansion factor was kept at 4.5, yielding a transversal temperature of $kT_\perp \simeq 25$ meV. The energy removed from the transverse degrees of freedom is put into the longitudinal motion, but the energy transfer does not influence the longitudinal temperature considerably. The additional energy spread can be viewed as an increase in the cathode temperature in Eq. (3.13) by the amount $kT_0(1 - 1/f_a)$. However, the dominant contribution is still that of the longitudinal-longitudinal heating, and the longitudinal temperature is therefore unaffected by the expansion.

Having established the transversal and longitudinal electron temperatures, the energy resolution in the experiment can be obtained. As mentioned previously, the collision energy spread is essentially governed by the electron energy spread, and therefore the ion energy spread is neglected in the following. Furthermore, the ions probe different parts of the electron space charge field, which in addition to the thermal electron velocity spread, influences the

collision energy spread. For the time being, however, this contribution is neglected, but it will be dealt with shortly.

Assuming parallel beams, the electron velocity distribution in the ion rest frame is given by:

$$f(\mathbf{u}, \Delta) = \frac{m_e}{2\pi k T_\perp} e^{-m_e u_\perp^2/2kT_\perp} \sqrt{\frac{m_e}{2\pi k T_\parallel}} e^{-m_e(u_\parallel - \Delta)^2/2kT_\parallel}, \tag{3.19}$$

where $u_\perp$ and $u_\parallel$ are the transversal and longitudinal electron velocity components in the ion rest frame. Furthermore, $\Delta = |\langle \mathbf{v}_e \rangle - \mathbf{v}_i|$ is the detuning velocity between the ions and the electrons, and $\mathbf{v}_i$ and $\langle \mathbf{v}_e \rangle$ are the ion and electron beam mean velocities, respectively. The detuning energy, defined as $E_d = m_e \Delta^2/2$, is equal to the relative energy in Eq. (3.8). The longitudinal velocity, $u_\parallel$, is isolated from the equation $E_e = m_e(u_\perp^2 + u_\parallel^2)/2$, and in Eq. (3.19) $u_\parallel$ is then substituted by the resulting expression. By integrating over the transverse velocity, the electron energy distribution in the rest frame of the ions is found to be

$$f(E_e, E_d) = \int f(\mathbf{u}, \Delta) \frac{du_\parallel}{dE_e} du_\perp. \tag{3.20}$$

$f(E_e, E_d)$ is the distribution of collision (or relative) energies and thus determines the energy resolution of the experiment. The integral above can be solved numerically, and the results for three different detuning energies are shown in Fig. 3.5. To illustrate the effect of the adiabatic expansion of the electron beam, distributions for an expanded ($kT_\perp = 25$ meV) and unexpanded ($kT_\perp = 100$ meV) beam are shown.

An important characteristic of the electron energy distribution is the energy spread, $\delta E_e(E_d)$, as a function of the detuning energy. The expression for the energy spread is derived in appendix B and the result is:

$$\delta E_e(E_d) = \sqrt{(kT_\perp)^2 + \frac{1}{2}(kT_\parallel)^2 + 2kT_\parallel E_d}. \tag{3.21}$$

As is clear from Fig. 3.5, the energy distributions are neither Gaussians nor symmetric, and hence the energy spread calculated above should be interpreted with care. Nonetheless, Eq. (3.21) implies that the energy resolution at low relative energies is determined by the transversal temperature and by the longitudinal one at higher energies ($E_{rel} \gtrsim 10$ eV), a trend also evident in Fig. 3.5.

The above equation neglects the additional spread in collision energy which stems from the fact that the ions probe different parts of the electron space

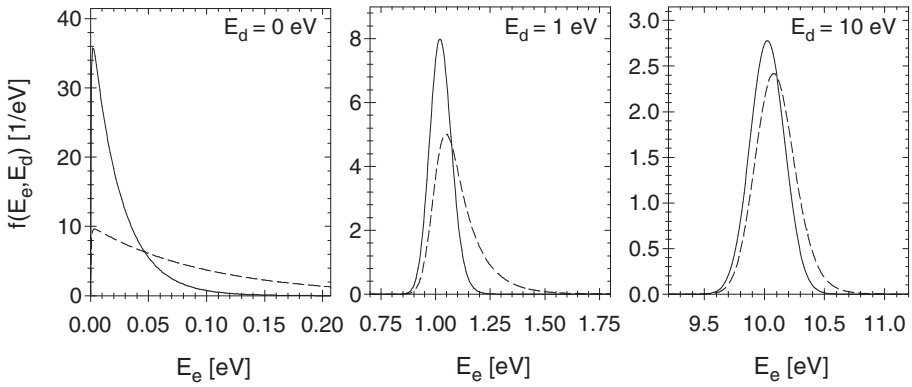

Figure 3.5: Electron energy distributions in the ion rest frame calculated for three different detuning energies. The solid and dashed curves represent distributions with transversal temperatures of $kT_\perp = 25$ meV and 100 meV, respectively. In all cases, the value used for the longitudinal temperature is $kT_\parallel = 1$ meV.

charge potential. To take this contribution into account, it is assumed that at each radial distance, r, the electron velocity distribution in the ion rest frame obeys Eq. (3.19), where $v_e(r) = \sqrt{2E_e^{lab}(r)/m_e}$ is now a function of the radial distance. Here, $E_e^{lab}(r)$ is a solution to the equation

$$E_e^{lab}(r) = e\left(V_{acc} - K_{sp}(r)\frac{I_e}{\sqrt{E_e^{lab}(r)}}\right). \tag{3.22}$$

The electron current is related to the acceleration voltage through Eq. (3.2), and hence the energy difference between electrons in the center and at the edge depends on the perveance. The collision energy distribution is now obtained in a similar manner as Eq. (3.20), except that the distribution must be averaged over r. Figure 3.6 shows the longitudinal collision energy spread for two different values of the perveance. The situation from the left graph is taken from an experiment on PO_2^- with $m_e E_i/M_i = 15.5$ eV, $V_{acc} = 70$ V and $P = 2.79 \times 10^{-3}$ mA/V$^{3/2}$, and in the right one, the value of the perveance has been doubled. As evident, the perveance may be chosen in such a way that the resolution is determined by the thermal spread. However, if the perveance is too large, the contribution from the space charge potential cannot be ignored. Roughly speaking, the additional spread becomes significant when the energy difference, ΔE_{sp}, between electrons in the center and at the ion beam edge is larger than the energy spread obtained from Eq. (3.21), that is

$$\Delta E_{sp} = E_e^{lab}(R_i) - E_e^{lab}(0) > \delta E_e(E_d). \tag{3.23}$$

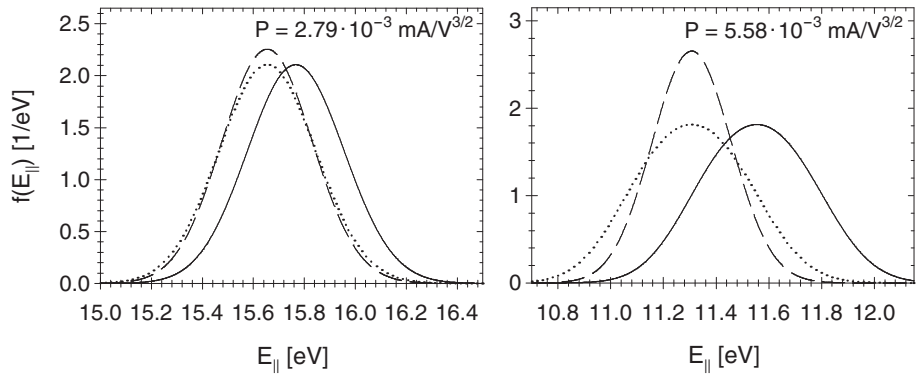

Figure 3.6: The longitudinal collision energy distributions for two different values of the perveance. The dashed curves represent the distribution on the center axis of the electron beam (infinitely narrow ion beam), whereas the solid curves show the distribution for an ion beam of radius $R_i = 0.5$ cm. To illustrate the change in spread, the latter distribution is overlayed the first (dotted curves).

3.3 Experimental procedures at ASTRID

The interesting quantities in electron-anion collisions are the cross section for various processes as a function of collision energy and the branching ratios of the different reaction channels. This section is devoted to a description of how these quantities are actually measured in the merged-beams setup at ASTRID.

Experiments are initiated by extracting ions from the ion source, injecting the desired ions into ASTRID, and accelerating them to final energies in the order of MeV. Since the injection and acceleration stage has a duration of several seconds, the ions are expected to be in thermal equilibrium with the surroundings during storage. While circulating in the ring, the ions undergo collisions with residual gas causing the formation of neutral particles. Upon arriving at the next dipole magnet, the ions continue along the stored orbit whereas the neutrals pass unaffectedly through the magnetic field thereby leaving the ring. Placed in one of the corners of ASTRID are various detectors which are used to detect the neutral products (see Fig. 3.3). One is a Micro Sphere Plate with a fluorescent phosphor screen. This imaging detector serves merely as a means of obtaining a visual image of the ion beam position in the ring and is not employed during actual measurements. Instead, an energy sensitive solid state surface-barrier detector (SSD) is utilized. When impacting on the SSD, the neutrals give rise to a signal proportional to the energy deposited in the detector. If a collision neutralizes the ion in the right section, the formed neu-

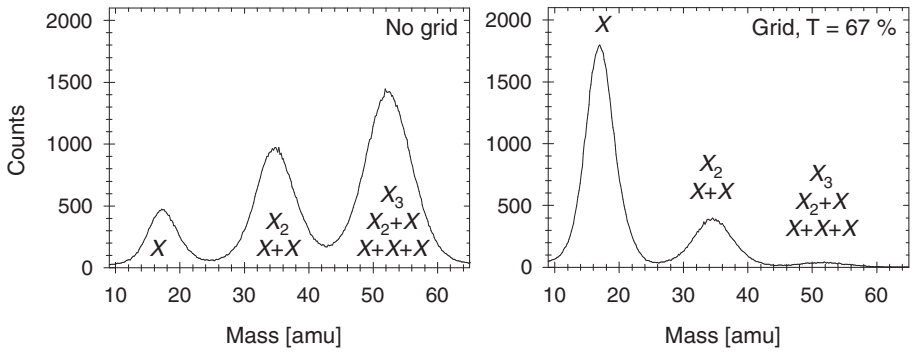

Figure 3.7: Pulse height spectra with $OH^-(H_2O)_2$ stored in the ring. **Left:** Spectrum without a grid in front of the detector. **Right:** Spectrum with a grid of 68% transmission inserted in front of the detector. *X* denotes O, OH or H_2O as these cannot be separated by the detector.

tral fragments hit the detector and deposit the full energy, E_i, of the ion beam. However, if charged fragments are formed in the collision, only the energy carried by the neutrals is deposited as the charged fragments do not reach the detector because of the dipole magnetic field. Since each fragment formed in a collision carries a fraction of the full energy proportional to its mass, the pulse height spectrum of the SSD contains information about the chemical composition of the ion beam. An SSD spectrum recorded with $OH^-(H_2O)_2$ stored in the ring is shown in Fig. 3.7. Due to the finite energy resolution of the detector, O, OH and H_2O cannot be distinguished, and the signals from single hydrogen atoms cannot be resolved from electronic noise. Accordingly, only three distinct peaks show up in the spectrum. Furthermore, the detector cannot resolve molecules from groups of molecular fragments of the same total mass arriving within a few microseconds as the two events deposit the same amount of energy. Therefore, each peak sums up the detections of several different events as also indicated in the figure.

After using the SSD to check that it is in fact the desired ions that are stored, the next step is to ensure good overlap between the ions and the electron beam. In the initial optimization, the imaging detector is used to visually center the electron-induced signal on the SSD detector. Afterwards, the overlap is adjusted more carefully by monitoring the signal from the SSD and optimizing the signal-to-background ratio and the total count rate.

3.3.1 Cross section measurements

The cross sections for electron-induced reactions are measured as a function of relative energy by varying the electron energy in the lab frame while keeping the ion energy fixed. One measurement cycle consists of injecting and accelerating the ions, merging them with the electron beam to perform the collision measurements, and finally ramping down the dipole magnets to prepare for the next injection. During each cycle, the collision energy remains constant, and the measurement at a particular energy is repeated for a given number of injections before the electron energy is changed. During a measurement, the count rates in each peak appearing in the SSD spectrum are recorded as a function of storage time. To allow for subtraction of the count rate stemming from residual gas collisions, the electron beam is chopped by alternating the grid anode in front of the gun between 0 V and −3 kV. The typical chopping frequency is 20–40 Hz. Furthermore, the electron current and acceleration voltage are recorded in each cycle.

Due to the finite spread in relative velocity, it is not possible to extract the cross section directly from measurable quantities. Instead, the quantity extracted from the experiments is the rate coefficient

$$\langle v\sigma\rangle(E_{\mathrm{rel}}) = \int v\sigma(v) f\left(\boldsymbol{v}, \sqrt{2E_{\mathrm{rel}}/m_{\mathrm{e}}}\right) \mathrm{d}\boldsymbol{v}, \tag{3.24}$$

which is the velocity-weighted cross section averaged over the relative-velocity distribution. In the expression, v is the relative velocity, σ the cross section, and $f(\boldsymbol{v}, \sqrt{2E_{\mathrm{rel}}/m_{\mathrm{e}}})$ the three-dimensional distribution of relative velocities from Eq. (3.19).

In terms of the measurable quantities, the total rate coefficient for all processes leading to an event in SSD peak number k can be expressed as

$$\langle v\sigma\rangle_{\mathrm{meas}} = \frac{N(k) - N_0(k) f}{N_{\mathrm{i}}} \frac{v_{\mathrm{i}}}{L\varepsilon n_{\mathrm{e}}}, \tag{3.25}$$

which is then measured as a function of the relative energy, E_{rel}. Here, v is the electron velocity in the ion rest frame, σ the cross section, v_{i} the ion velocity, n_{e} the electron density, L the length of the interaction region and $\varepsilon(=1)$ the detection efficiency. $N(k)$ and $N_0(k)$ are the rates of neutrals in SSD peak number k measured with the electron beam on and off, respectively. The factor $f = \exp(T_{\mathrm{ch}}/\tau)$, where $1/(2T_{\mathrm{ch}})$ is the chopping frequency, accounts for the fact, that the two rates are not recorded simultaneously. Thus, the finite lifetime τ of the ion beam must be taken into consideration. Since N_0 is recorded as a function of storage time and is proportional to the number of ions in the ring, this quantity can be used to determine the ion beam lifetime. N_{i} is the

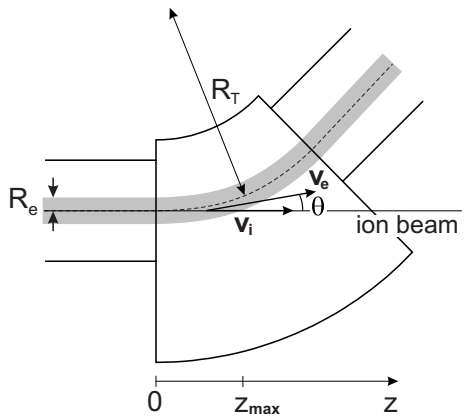

Figure 3.8: Close-up of the toroid region where the electrons and ions separate.

rate of ions passing through the electron cooler. Determination of N_i, and thereby the absolute rate coefficient, requires a measurement of the number of ions stored in the ring. However, the device normally used to measure the ion beam currents in these experiments has a lower limit of about 50 nA. For most of the experiments presented here, the currents extracted from the ion source were of the order 10–100 nA, thus making it difficult to perform current measurements. Nevertheless, relative rates were found by substituting N_i with the rate of background events, a quantity proportional to the number of ions in the ring as already mentioned.

In the toroid regions of the electron cooler, where the electron and ion beams merge and separate, electron and ion velocities are not strictly parallel. This leads to higher relative energies in these regions than in the center of the interaction region. Consequently, the rate coefficient measured at a given relative energy, $\langle v\sigma\rangle_\mathrm{meas}$, contains a small contribution from higher relative energies which must be subtracted to obtain the true rate coefficient $\langle v\sigma\rangle$. The collision energies encountered in the toroid regions can be written as

$$\begin{aligned} E_\mathrm{rel}^\mathrm{tor}(z) &= E_\mathrm{e}^\mathrm{lab} + \frac{m_\mathrm{e}}{M_\mathrm{i}} E_\mathrm{i} - 2\sqrt{E_\mathrm{e}^\mathrm{lab} E_\mathrm{i} \frac{m_\mathrm{e}}{M_\mathrm{i}}} \cos\theta \\ &= E_\mathrm{rel} + 2\sqrt{E_\mathrm{e}^\mathrm{lab} E_\mathrm{cool}} \left[1 - \frac{\sqrt{R_\mathrm{T}^2 - z^2}}{R_\mathrm{T}} \right], \end{aligned} \tag{3.26}$$

where $E_\mathrm{cool} = \frac{m_\mathrm{e}}{M_\mathrm{i}} E_\mathrm{i}$ is the electron energy at which the ions and electrons travel at the same velocity. Furthermore, z is the longitudinal position in the

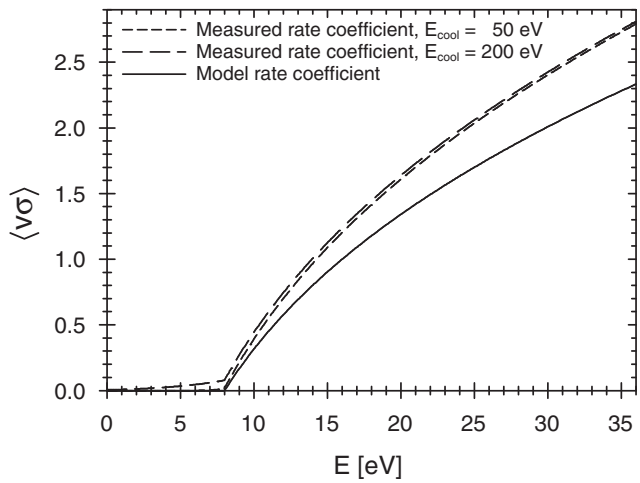

Figure 3.9: Illustration of the toroid contribution. A model rate coefficient resembling that of an electron detachment process is shown (solid curve) along with the measured rate coefficient for two different values of the ion storage energy expressed in terms of the cooling energy, $E_{\mathrm{cool}} = \frac{m_{\mathrm{e}}}{M_{\mathrm{i}}} E_{\mathrm{i}}$ (dashed curves).

toroid region, θ the corresponding angle between the electron and ion velocities, and R_{T} the radius of curvature of the electron beam in the toroid magnet. At a given relative energy, the measured rate coefficient can then be expressed as

$$\begin{aligned}\langle v\sigma\rangle_{\mathrm{meas}}(E_{\mathrm{rel}}) \cdot L_0 &= \langle v\sigma\rangle(E_{\mathrm{rel}}) \cdot L_0 + 2\int_0^{z_{\mathrm{max}}} \langle v\sigma\rangle(z)\mathrm{d}z \\ &= \langle v\sigma\rangle(E_{\mathrm{rel}}) \cdot L_0 + 2\int_{E_{\mathrm{rel}}}^{E_{\mathrm{max}}} \langle v\sigma\rangle(E') \cdot \left(\frac{\mathrm{d}z}{\mathrm{d}E}(E')\right)\mathrm{d}E',\end{aligned} \tag{3.27}$$

where E_{max} is the maximum collision energy reached at the position $z_{\mathrm{max}} = \sqrt{(R_{\mathrm{T}}+R_{\mathrm{e}})^2 - R_{\mathrm{T}}^2}$, and L_0 is the length of the region where the ion and electron velocities are parallel. From the measured rate coefficient, the toroid contribution can be found by exploiting the above equation in an iterative manner. The true rate coefficient is then obtained by subtracting the calculated contribution from the measured one. For a model cross section, Fig. 3.9 shows the measured rate coefficient including the toroid contribution to illustrate the toroid effect. All data presented in this thesis are corrected for toroid contributions.

Having obtained the rate coefficient $\langle v\sigma\rangle$, it is now possible to extract the cross section, which is calculated by dividing the rate coefficient by the aver-

age relative velocity, that is

$$\sigma \simeq \frac{\langle v\sigma \rangle}{\sqrt{\frac{2E_{\mathrm{rel}}}{m_{\mathrm{e}}}}}. \tag{3.28}$$

If the velocity distribution is highly asymmetric, the true cross section is poorly approximated by the above equation. However, as can be seen in Fig. 3.5, this is true only for very low collision energies (in the order $kT_{\perp}$). Since the threshold energies for electron detachment for all ions investigated in the present thesis are far above this energy region, the true cross section is well-approximated by Eq. (3.28).

3.3.2 Branching ratio measurements

While cross sections are always extracted by the analysis presented above, the analysis to obtain the branching ratios of different reaction channels varies from molecule to molecule. This is of course due to the fact that the reaction channels of two different molecules are not comparable, and hence each molecule must be treated individually. Nonetheless, the overall procedure is the same, and therefore the measurement technique and the following analysis are presented through an example.

The SSD pulse height spectrum from the $OH^{-}(H_2O)_2$ experiment (see Chap. 5) is shown in Fig. 3.7. As mentioned, it is not possible to distinguish between O, OH and H_2O due to the finite energy resolution of the detector. Neither is it possible to resolve the peaks corresponding to the detection of one or several hydrogen atoms from electronic noise present in the SSD spectrum at low energy. Thus, only three distinct peaks appear in the spectrum arising from the detection of one, two, and three entities, X, where X represents O, OH or H_2O. Furthermore, the detector cannot resolve molecules from groups of molecular fragments of the same total mass. For instance, an X_2 molecule will induce the same signal as two X fragments arriving simultaneously. However, this problem must be surpassed if the branching ratios are to be found. In order to separate such channels from each other, a well-established grid technique is used [148–151]. Here, a grid of a finite transmission, T, is inserted in front of the detector (see Fig. 3.3). In the present experiments, two different grids of transmissions $T \simeq 24\%$ and $T \simeq 68\%$ are used.

Only neutral fragments are detected, and accordingly no information is obtained about channels that do not lead to neutral fragments. Such channels are therefore neglected in the following. Moreover, some channels cannot be distinguished from each other as they lead to the same neutral fragments, and these are thus treated as only one single channel. Bearing this fact in mind, electron scattering on a system consisting of three identical entities, X, such as

$OH^-(H_2O)_2$, can lead to the following reaction channels:

$$
\begin{array}{lcll}
X_3^- + e^- & \rightarrow & X_3 + 2e^- & (C_a) \\
 & & X_2 + X + 2e^- & (C_b) \\
 & & X + X + X + 2e^- & (C_c) \\
 & & X_2^- + X + e^- & \\
 & & X_2^+ + X + 3e^- & (C_d) \\
 & & \cdots & \\
 & & X^- + X_2 + e^- & \\
 & & X^+ + X_2 + 3e^- & (C_e) \\
 & & \cdots & \\
 & & X^- + X + X + e^- & \\
 & & X^+ + X + X + 3e^- & (C_f) \\
 & & \cdots &
\end{array}
\quad . \tag{3.29}
$$

Without a grid in front of the detector, the channels C_a, C_b, and C_c will all contribute to the signal in the full energy peak as the total mass of all the neutral fragments is the same for each of the three channels. However, with a grid of transmission, T, inserted in front of the detector it is possible to differentiate between these channels since they will contribute to the full energy peak with different weights: T, T^2 and T^3, respectively. Figure 3.7 shows the pulse height spectrum with and without a grid in front of the detector. The figure shows that the relative intensities of the peaks change when the grid is inserted. With a grid, the total rate of events, R_0, is distributed among the three peaks according to

$$
\begin{aligned}
R_3 &= [aT + bT^2 + cT^3]R_0 \\
R_2 &= [bT(1-T) + 3cT^2(1-T) + eT + fT^2]R_0 \\
R_1 &= [bT(1-T) + 3cT(1-T)^2 + dT + 2fT(1-T)]R_0,
\end{aligned} \tag{3.30}
$$

where R_1, R_2 and R_3 are the rates in the peak corresponding to the detection of one, two and three neutral X fragments, and $a, \ldots, f$ are the branching ratios of the channels $C_a, \ldots C_f$. The branching ratios are normalized through the equation

$$a + b + c + d + e + f = 1. \tag{3.31}$$

As the rates in the three peaks are measured at three different transmissions (T = 100%, 68% and 24%), ten equations have to be solved (Eq. (3.30) for each of the three transmissions plus the normalization condition). It should be noted that the total count rate R_0 is not necessarily the same for the three

different grid measurements, and hence the number of unknowns is nine (six branching ratios and three total count rates). Usually the total count rates are eliminated from the equations by solving the set of equations for R_1/R_3 and R_2/R_3 instead.

The system of equations is solved using a standard χ^2-minimization routine, yielding the branching ratios for the different decay channels.

3.4 The crossed-beams setup at ELISA

Investigations of electron-anion collisions can also be performed at the ELectrostatic Ion Storage ring, Aarhus (ELISA). The ions are injected into the ring where they are stored for a few seconds. Shortly after injection, the ions are crossed with an electron beam in a straight section of the ring. The electrons are provided by ETRAP which is a device capable of producing a beam of electrons or a cloud of trapped electrons. In the following, the ELISA storage ring is described in further detail along with the ETRAP device. Finally, the experimental procedures at ELISA are outlined.

3.4.1 The ELISA storage ring

The ELISA storage ring [51, 152] differs significantly from conventional magnetic storage rings, such as ASTRID, in a number of ways. A fundamental difference is the principle of operation. Where magnetic fields are used to store ions in ASTRID, ELISA relies solely on electrostatic fields for steering and focusing purposes. As a consequence, ELISA has different properties than ASTRID, a fact becoming more obvious when comparing the equations of motion for ions in the two rings. The magnetic field strength, B, required to deflect an ion of mass m and charge q into a circular orbit of radius R is found by equating the Lorentz force, mvB, with the centripetal force, mv^2/R:

$$B = \frac{mv}{qR} = \frac{\sqrt{2mE}}{qR}, \tag{3.32}$$

where v and E are the velocity and energy of the ion, respectively. It is evident that the required magnetic field strength is dependent on the mass of the ion for fixed energy. Substituting the magnetic field by an electric field of field strength $\mathcal{E}$ changes the Lorentz force to $q\mathcal{E}$, and instead the equation of motion yields:

$$\mathcal{E} = \frac{mv^2}{qR} = \frac{2E}{qR}. \tag{3.33}$$

The expression reveals that the required electric field strength is independent of the ion mass for a given energy. Ignoring gravity, this means that for a given energy-to-charge ratio ions of any mass can be stored in ELISA. This fact is the major advantage of an electrostatic storage ring as compared to a magnetic one, since the settings of the electrostatic steering devices remain the same for any ion — be it H^- or a heavy biomolecular negative ion — provided the energy-to-charge ratio is constant. The latter is easily fulfilled, as this ratio is nothing but the acceleration voltage. Hence, only the magnet for mass-selection and a few timing parameters before the ring need consideration when changing between storage of ions of various mass.

In a magnetic storage ring, it is also possible to store heavy ions such as e.g. C_{60}^-, but in these cases the storage energy is limited to the keV-range due to the finite magnetic rigidity, i.e. finite value of $B{\cdot}R$. However, the main advantage of a magnetic ring over an electrostatic one is mostly related to the high MeV storage energy that can be obtained for lighter molecules. The high storage energy enables the use of energy-sensitive detectors to identify the neutral fragments, but this feature is lost for very heavy ions due to the lower storage energy.

For comparison, the storage energy in ELISA is limited to 25 keV, which presently rules out the use of energy-sensitive detectors due to their finite energy resolution (however, energy-sensitive detectors that can be used for low-energy electrostatic storage rings are currently being developed [153]). Thus, only the total count rate of neutrals can be recorded, and no information about the identity of the fragments is obtained.

Apart from the drawback of low storage energy, ELISA has no other main disadvantages. The smaller size allows the entire ring to be cooled down by mounting an insulating box around it and filling the box with liquid nitrogen. With this technique, temperature control from room temperature down to −55°C has been demonstrated [154, 155]. Furthermore, no cooling water has to be supplied to the ring as opposed to a magnetic ring, where cooling water is of critical importance due to the large currents (∼1000 A) carried by the coil windings of the dipole and quadrupole magnets. Hysteresis effects are absent, and finally, the cost of building an electrostatic storage ring is small.

Design of ELISA

A schematic drawing of the ELISA storage ring is shown in Fig. 3.10. It has a race-track shape with a circumference of 8.3 m. The ion orbit is defined by a 160° cylindrical electrostatic deflector at each end together with four 10° parallel plate deflectors. To position the beam vertically, parallel plate deflectors are placed before and after the 160° deflectors, and in each of the two straight sections two pairs of electrostatic quadrupoles serve to focus the ion beam.

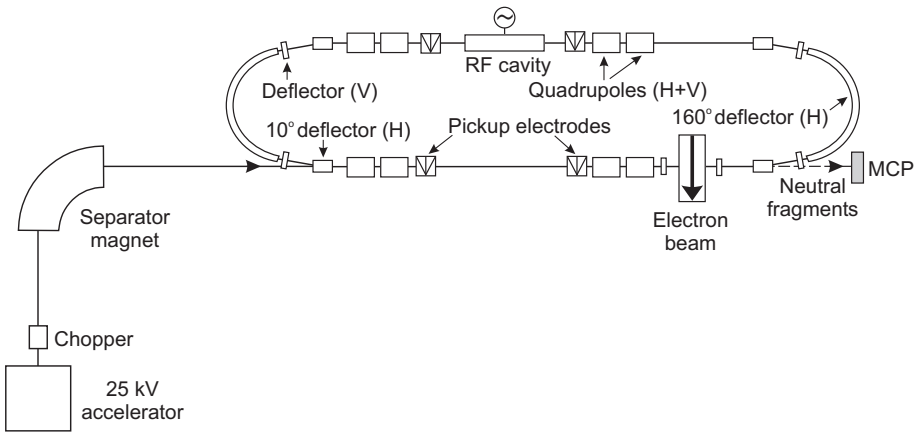

Figure 3.10: Schematic drawing of the electrostatic ion storage ring, ELISA. H and V denote elements affecting the ion trajectory in the horizontal and vertical directions, respectively.

Furthermore, the ring is equipped with pickup electrodes, which allow monitoring the ion beam position in the ring for intense beams (ion currents greater than ∼0.1 nA). An RF system located in the second straight section makes it possible to bunch a circulating ion beam [152], but this feature is rarely used. In the first straight section of ELISA, the electron target ETRAP is mounted which is capable of producing an electron beam crossing the ion beam at right angles. A magnetic field longitudinal to the electron beam provides the radial confinement of the electrons, and this field, which is transverse to the ion beam direction, causes the ions to be deflected vertically. To compensate for this deflection, vertical electrostatic steerers are placed just before and after the interaction region where the electrons and the ions are overlapped.

It is possible to mount various ion sources on the accelerator in order to use the most suited source to produce the desired ions. The ions are produced, extracted from the source, and accelerated to typically 22 keV. If the mounted ion source produces a continuous beam of ions, a chopper placed immediately after the acceleration stage can be used to pulse the beam. The chopper allows a bunch of ions to pass before it deflects the remaining beam away from the injection beam line. The time duration of the bunch is set to one revolution time in ELISA to ensure storage of the maximum number of ions. To separate the desired ions from other ions present in the bunch, the bunch is mass-to-charge analyzed in a separator magnet, and only the chosen ions continue

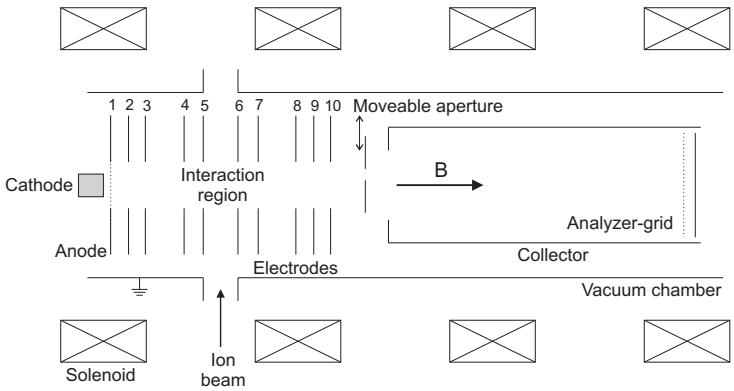

Figure 3.11: Schematic drawing of the ETRAP electron target.

further downstream. To inject the ions, the first 10° deflector in ELISA is kept at 0 V thus allowing the ions to enter the ring. Just before the first ions have made a full roundtrip, the 10° deflector is set to a value allowing for storage of the ions.

The pressure in the ring is 10^{-11}–10^{-10} mbar resulting in typical ion lifetimes in the order of several seconds at the storage energy of 22 keV.

3.4.2 The electron target ETRAP

The electron target for collision experiments is provided by ETRAP which is mounted in the first straight section of ELISA. A schematic drawing of ETRAP is seen in Fig. 3.11, and the details of the design and some electron beam properties are described in Ref. [9]. The ETRAP device has two modes of operation: it can provide a beam of electrons to study collision processes at relative energies ranging from ∼3 eV, or, as the name implies, it can trap a cloud of electrons to study collisions at low relative energies (below ∼1 eV).

The electrons are delivered by a 15 mm diameter BaO-coated tungsten cathode of the same type as the one mounted in the electron cooler at ASTRID. From the cathode, the electrons are accelerated towards the anode grid in front of the cathode. The potential of the anode grid can be changed allowing the grid to be used for blocking the electron beam or for reducing the electron current, which depends on the potential difference between the cathode and the anode as described by Child's law, Eq. (3.2). The electrons are guided through the interaction region by an axial magnetic field of ∼200 Gauss provided by four external coils. At the end of ETRAP, the electrons are dumped in a biased Faraday cup used to measure the electron current. Between the anode and

the cup, a series of nine ring electrodes is placed. The electrodes may be used to create a Penning trap potential to trap a cloud of electrons in the interaction region (trap mode). However, in the work presented in this thesis, all the electrodes were grounded in order to create a beam of electrons instead (beam mode).

Energy resolution

In ELISA, the ion beam and the electron beam cross at right angles as opposed to the ASTRID setup, where the two beams are merged. The distribution of collision energies encountered in ELISA is therefore fundamentally different from that in ASTRID. As described on p. 31, the electron energy in the laboratory frame depends on the radial position within the beam due to the space charge potential created by the surrounding electrons (see Eq. (3.22)). In crossed-beams experiments, the ions traverse the electron beam and therefore experience the full range of different longitudinal electron energies induced by the space charge potential. To investigate how this effect influences the energy resolution in the experiments, it is again useful to consider the electron velocity distribution. Since the acceleration breaks the spherical symmetry of the three-dimensional Maxwellian velocity distribution at the cathode, the distribution is described by the flattened Maxwell distribution of Eq. (3.10). In ETRAP, the electron beam is not expanded, and the transverse temperature is therefore equal to the cathode temperature yielding $kT_\perp \simeq 100$ meV. Like in the electron cooler at ASTRID, the longitudinal degree of freedom undergoes a kinematic compression, which significantly reduces the temperature, but the actual temperature has not been measured. In the following the temperature is assumed to have the same value as in the electron cooler, i.e. $kT_\parallel = 1$ meV. At each radial distance r, the longitudinal energy distribution in the laboratory frame is centered at an energy at this particular distance, $E_\mathrm{e}^\mathrm{lab}(r)$, and may thus be written as

$$f(E_\parallel, r) = \frac{1}{2\sqrt{\pi k T_\parallel}} \frac{1}{\sqrt{E_\parallel}} \mathrm{e}^{-\left(\sqrt{E_\parallel} - \sqrt{E_\mathrm{e}^\mathrm{lab}(r)}\right)^2 / kT_\parallel}. \tag{3.34}$$

In the expression, $E_\mathrm{e}^\mathrm{lab}(r)$ is the solution to Eq. (3.22), and this solution depends on the acceleration voltage, V_acc, applied to the electron beam and the electron current, I_e. In Fig. 3.12, the above distribution is plotted for electrons at the center of the beam and electrons close to the edge for different electron currents. The calculations assume an electron beam radius of 0.75 cm and a space charge potential of zero at a radius of 1.7 cm. The inner radius of the grounded ring electrodes is 1.5 cm, but in the interaction region situated be-

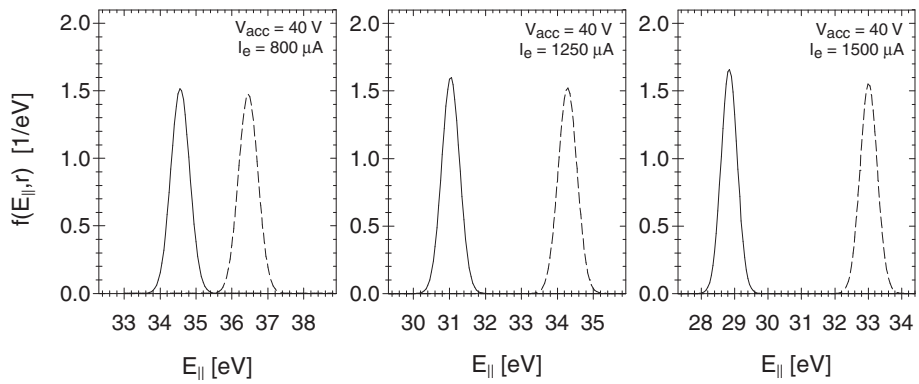

Figure 3.12: Calculated longitudinal energy distribution at the center of the electron beam (solid curves, $r = 0$ cm) and close to its edge (dashed curves, $r = 0.7$ cm) for different values of the electron current.

tween two electrodes, the equipotential curves presumably expand slightly in the radial direction. It is seen that the energy spread at a given radius is much smaller than the energy difference between $E_e^{lab}(r)$ at different values of r. Hence, the energy resolution is limited by the energy spread introduced by the space charge potential. Furthermore, the energy difference between the center and the edge is seen to increase with increasing current. By integration over the cross sectional area of the electron beam, the total longitudinal energy distribution in the lab frame can be found according to:

$$f_{\parallel}(E_{\parallel}) = \frac{1}{\pi R_e^2} \int_0^{R_e} f(r, E_{\parallel})\, 2\pi r \, \mathrm{d}r. \tag{3.35}$$

With this distribution at hand, it is possible to calculate the distribution of electron energies in the ion rest frame. As the ions move transverse to the electrons in the horizontal plane, only the horizontal electron energy distribution in the lab frame must be transformed in order to obtain the distribution of collision energies (see Fig. 3.13 for definitions of the different velocity components). The horizontal electron velocity distribution in the ion rest frame is centered on the ion velocity, $\sqrt{2E_i/M_i}$, which gives the following distribution for the horizontal electron energy, E_x, in the ion rest frame:

$$f_x\left(E_x, \frac{m_e}{M_i}E_i\right) = \frac{1}{2\sqrt{\pi k T_{\perp}}} \mathrm{e}^{-\left(\sqrt{E_x} - \sqrt{m_e E_i / M_i}\right)^2 / kT_{\perp}} \frac{1}{\sqrt{E_x}}. \tag{3.36}$$

To determine the distribution of collision energies, the three-dimensional elec-

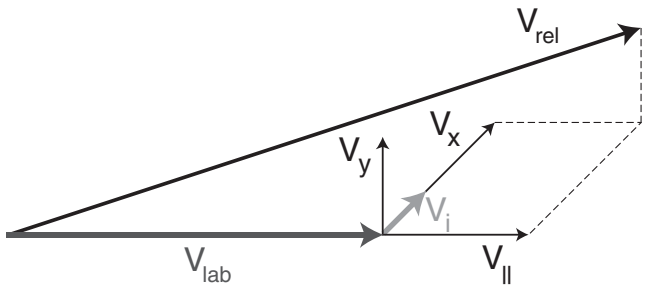

Figure 3.13: Drawing of the different velocity definitions.

tron energy distribution in the ion rest frame is now integrated over the horizontal and vertical energies, E_x and E_y:

$$f\left(E_{rel}, \frac{m_e}{M_i}E_i\right) = \iint f_{\parallel}(E_{rel} - E_x - E_y) f_y(E_y) f_x\left(E_x, \frac{m_e}{M_i}E_i\right) dE_x dE_y, \quad (3.37)$$

where the vertical electron energy distribution is described according to:

$$f_y(E_y) = \frac{1}{2\sqrt{\pi k T_{\perp}}} e^{-E_y/kT_{\perp}} \frac{1}{\sqrt{E_y}}. \quad (3.38)$$

Figure 3.14 shows the total longitudinal energy distribution from Eq. (3.35) together with the distribution of relative energies (the equation above) for three different acceleration voltages. The values used for the ion energy and mass are 22 keV and 46 amu, which exemplifies collision experiments with NO_2^-, and also the values of the voltage and current resemble what is normally used during experiments. Evidently, the energy resolution is limited by the longitudinal spread, and only at low acceleration voltages does the transversal spread contribute significantly. An estimate of the width of the distribution can be found by substituting $I_e = PV_{acc}^{3/2}$ and $E_e^{lab}(r) \simeq eV_{acc}$ on the right hand side of Eq. (3.22). The width, ΔE_{rel}, is roughly equal to the energy difference between electrons in the center and at the edge of the electron beam yielding

$$\Delta E_{rel} = E_e^{lab}(R_e) - E_e^{lab}(0) \simeq P(K_{sp}(0) - K_{sp}(R_e))eV_{acc}. \quad (3.39)$$

Thus, the width is ∼0.8 eV at a mean relative energy of 9 eV and approximately linearly increasing to ∼3.3 eV at 35 eV.

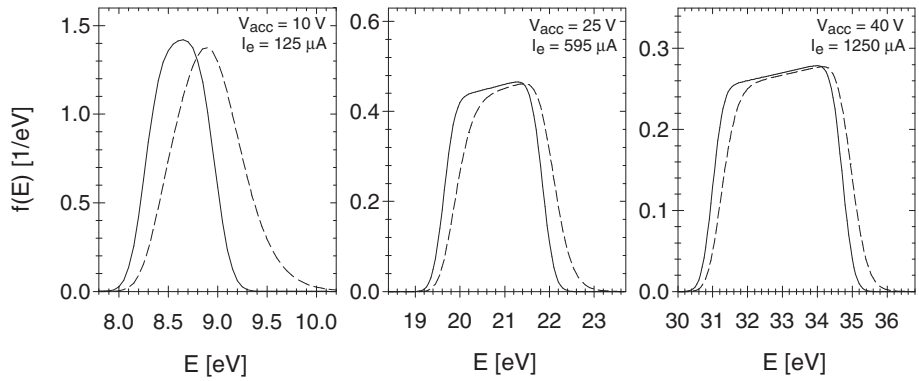

Figure 3.14: Calculated electron energy distributions in ELISA. Solid curves show the distribution of longitudinal electron energies, $E_{\parallel}$, while the dashed curves represent the distribution of relative collision energies, E_{rel}.

Relative energy and the effective space charge constant

In experiments, it is crucial to know the average relative energy for a given acceleration voltage applied to the cathode. Suppose for a moment that the electron energy in the laboratory frame is known. Since the electrons and the ions cross at an angle of 90° the electron energy in the ion rest frame, E_{rel}, becomes

$$E_{\mathrm{rel}} = E_{\mathrm{e}}^{\mathrm{lab}} + \frac{m_{\mathrm{e}}}{M_{\mathrm{i}}} E_{\mathrm{i}}. \tag{3.40}$$

Note that the above equation is only meaningful if the electron energy stored in the transversal degrees of freedom is much smaller than the energy stored in the longitudinal degree of freedom. This condition is always fulfilled in ETRAP. It is evident that the expression for the relative energy differs from that of the merged-beams configuration (see Eq. (3.8)). In particular, it must be noted that the above equation does not allow the relative energy to become zero. Hence, with the cross-beams setup low collision energies (below ∼3 eV) cannot be reached.

Finding the relative energy as a function of the acceleration voltage thus boils down to determining the average electron energy in the lab frame. The relation between the latter and the acceleration voltage is given by Eq. (3.7) where $K_{\mathrm{sp}}^{\mathrm{eff}}$ is the effective space charge constant. In order to calculate the relative energies, $K_{\mathrm{sp}}^{\mathrm{eff}}$ must be determined experimentally.

However, the procedure used at ASTRID to determine the space charge constant, described in Sec. 3.2.2, can obviously not be employed here. Instead,

the cross section of an anion can be measured in the same energy range with two different (V_{acc}, I_e) characteristics. For a given value of K_{sp}^{eff}, the two cross sections can be mapped out as a function of the relative energy, which depends on both V_{acc} and I_e through Eqs (3.7) and (3.40). In the region where the relative energies in the two measurements overlap, the two obtained cross sections must be identical. K_{sp}^{eff} is now varied until this requirement is fulfilled. Using this procedure, the value of K_{sp}^{eff} was found to be 46.8 $\mathrm{V}\sqrt{\mathrm{eV}}/\mathrm{mA}$.

For several different ions, comparisons between cross sections measured at both ASTRID and ELISA have revealed that in addition a fixed offset has to be introduced in Eq. (3.7) in order to obtain the actual electron energy. The offset can be subtracted from either V_{acc} or E_e^{lab}, and the difference is only very subtle in the final results. From a physical point of view, both situations make sense. The first could be ascribed to contact potentials or cathode work function effects, whereas the second could be due to a small potential in the interaction region causing the electrons to be not fully accelerated. For the data presented in Chap. 6, the offset has been applied to E_e^{lab}, as this was easier in the calibration procedure. The values obtained for the offset is $E_{offset} = 1.8$ eV, where this value must be subtracted from energy determined from Eq. (3.7) to obtain the true electron energy.

3.4.3 Experimental procedures

Experiments at ELISA are conducted in a way that is very similar to the one employed at ASTRID. Nevertheless, some differences between the two procedures exist, and therefore the technique is outlined below.

Before actual measurements are undertaken, good overlap between the ion and the electron beam must be ensured. Ions are extracted from the source, and the desired ions are subsequently injected into ELISA. During storage in the ring, the ions collide with the residual gas, and neutral fragments are formed in the process. Neutral fragments produced in the straight sections leave the ring after the next 10° deflector, since they are not affected by the electric fields. If created in the first section, the neutrals hit a Micro Channel Plate (MCP) detector placed behind the 10° deflector (see Fig. 3.10). Unlike the solid state detector used at ASTRID, the MCP cannot distinguish between particles of different mass, and only the total count rate of neutrals can be measured. Shortly before the deflector, the ion beam is crossed at right angles by the electron beam, and neutrals created in electron-ion collisions therefore also impinge on the MCP. In order to allow for background subtraction, the electron beam is turned on and off (chopped) at a frequency of 10–20 Hz. Good overlap between the two beams is ensured by changing the ion orbit in the ring slightly until a maximum electron-induced signal on the detector is achieved.

The total rate coefficient for production of neutrals is then measured as a function of relative energy by keeping the ion energy fixed while changing the electron energy. At ELISA, a measurement cycle starts by injecting the ions and letting them circulate for a while (50–500 ms) to assure vibrational cooling and decay of metastable ions. After this period, the ions are crossed with the chopped electron beam, and the count rates with and without electrons are recorded as a function of storage time. Furthermore, the electron acceleration voltage and electron current are recorded. After some seconds, the ion intensity has decayed significantly, at which point the measurement cycle is stopped, and the remaining ions are dumped in order to prepare for a new measurement cycle. During each cycle, the electron energy — and hence the collision energy — remains constant, and the measurement at a particular energy is repeated a given number of injections before stepping to the next energy point.

At present, it is not possible to measure the absolute ion current in ELISA, and therefore the total rate coefficient defined by Eq. (3.25) cannot be put on an absolute scale. Instead only the relative rate coefficient is extracted from the measurements, and therefore all constants entering Eq. (3.25) are skipped. In this case, the expression for the relative total rate coefficient is reduced to

$$\langle \sigma v \rangle_{\text{meas}} = \frac{N_{\text{s}} - N_{\text{b}} f}{N_{\text{b}} n_{\text{e}}}, \tag{3.41}$$

where N_{s} and N_{b} are the count rates with and without electrons, respectively, n_{e} is the electron density, σ the cross section and v the relative velocity. Due to the finite lifetime, τ, of the ion beam, a factor $f = \exp(T_{\text{ch}}/\tau)$, where $1/(2T_{\text{ch}})$ is the chopping frequency, must be introduced. This factor accounts for the difference in ion current during the recording of the signal and background count rates, N_{b} and N_{s}. The ion beam lifetime can be extracted from the measurements, since N_{b}, which is proportional to the number of stored ions, is recorded as a function of storage time.

The total rate coefficient is converted into a cross section by dividing it with the average collision energy

$$\sigma \simeq \frac{\langle \sigma v \rangle_{\text{meas}}}{\sqrt{\frac{2E_{\text{rel}}}{m_{\text{e}}}}}. \tag{3.42}$$

If the distribution of relative velocities is highly asymmetric or very broad, the cross section is approximated poorly by the above equation. As seen in Fig. 3.14, the distributions are not symmetric, and it could be speculated if the above equation is a good approximation. However, it turns out that for a number of different ions, the cross sections obtained at ELISA agree very well

with those measured at ASTRID. Therefore, the above equation is expected to give a fair approximation of the cross section, though the energy resolution is limited.

CHAPTER 4

Electron-impact detachment of PO_n^- ($n = 0$–3)

4.1 Introduction

Small doubly charged negative ions are intriguing systems as already mentioned in Chap. 2. They are unstable in the gas phase due to the large Coulomb repulsion between the excess charges, and the study of the properties of such systems therefore represents a challenge not only to experimentalists, but also to theoreticians.

To date, neither electronically bound nor unbound atomic dianions have been identified, whereas several di- and poly-atomic monoanions are known to form transient dianions when bombarded with electrons [21, 42, 45–49]. The transient dianions reveal themselves as resonant structures in the electron-impact detachment cross section of the monoanions. However, though resonance dianion states have now been observed for several systems, it remains a difficult task to predict for which molecular anions such states actually appear, a point clearly illustrated by Andersen and coworkers [45]. They studied electron-impact detachment of the isoelectronic species CN^- and BO^-, but only the former exhibits an observable resonant structure in the detachment cross section. Furthermore, this behavior is different from that of the isoelectronic species of NCO and NCS, both of which are able to form transient dianion states [49]. These findings are not readily explained, and it remains an open question why such a structure is not observed for BO^-.

In the present chapter, electron impact on PO_n^- ($n = 0$–3) is under investigation. This series of anions was chosen because of the resemblance to the

isoelectronic NO_n^-. Electron-impact detachment of NO_2^- and NO_3^- has previously been studied [21, 47], and in both cases, resonant structures were observed in the detachment cross sections. As the electronic structure of $PO_{2,3}^-$ resembles that of the corresponding nitrogen oxide anions, it could be expected that similar structures are observable for the former species. Thus, the comparison between the two different types of anions can shed more light on the conditions under which short-lived dianions are formed during collision events and, if observed, on the influence of size effects. Naively, dianions of $PO_{2,3}$ should be less unstable than the corresponding nitrogen oxide dianions since the Coulomb repulsion between the excess electrons in the former species is lowered as a result of the larger volume. Such an effect has been observed for the isoelectronic species of NCO and NCS [49].

Regarding electron-impact detachment of P^- and PO^-, no comparison can be made to N^- and NO^-. The latter two ions have not been studied, since N^- is electronically unstable [156, 157] and NO^- only very weakly bound with a binding energy of 0.026 ± 0.005 eV [158].

4.2 Experiment

The PO_n^- anions were formed in the ANIS sputter ion source described in Section 3.1.1. The cathode consisted of a mixture of 70% InP and 30% Ag, and to produce the oxygen-containing anions atmospheric air was furthermore let into the source. The extracted ion currents were in the order of 10–100 nA. After mass-selection and injection into the ASTRID storage ring at 150 keV, the ions were accelerated to final energies ranging from 1.72 MeV for PO_3^- to 4.41 MeV for P^-. The ion beam and the electron beam were merged several seconds after extraction of the ions from the ion source, at which time the ions are expected to be vibrationally cold.

The detector used for neutral particle detection was an energy sensitive surface barrier solid state detector (SSD) with a diameter of 4 cm. The detector was located 6 m after the electron-ion interaction region. For P^-, a single peak was observed in the SSD energy spectrum, while three peaks were seen for PO^- corresponding to detection of mass 16 (O), mass 31 (P), and mass 47 (PO and P + O), respectively[1]. As the masses of O_2 and P are very similar, four peaks showed up for PO_2^- equivalent to detection of mass 16 (O), mass 31–32 (P, O_2, and O + O), mass 47 (PO and P + O), and mass 63 (any combination of one P and two O atoms). In the case of PO_3^-, a peak corresponding to the detection of mass 79 would be expected in addition to the four peaks observed for PO_2, since the mass for three oxygen atoms is close to that of one P and

[1] All masses are given in atomic mass units (amu).

one O. However, the two peaks corresponding to detection of mass 63 and 79 are compressed into one single peak. This is attributed to the fact that the fragments lose energy on their way through the dead layer of the detector to the active area where they deposit their remaining energy. The energy loss is due to Coulomb interactions with nuclei and electrons of the detector material and scales with the square of the nuclear charge of fragments, thus being more significant for the heavier fragments [159]. Furthermore, the energy lost in the dead layer exhibits a broad distribution thereby causing a non-negligible spread in the detected energy deposit. Therefore, it is not possible to separate events leading to total neutralization, that is to PO_3 or channels of the same total neutral mass, from those leading to production of PO_2 (or channels of the same total neutral mass).

To extract the branching ratios, grid measurements were performed for all molecular ions with two grids of transmission, 68% and 24%, in addition to an equivalent measurement without a grid (see Sec. 3.3.2).

4.3 Results

4.3.1 P^-

The detachment cross section for P^- is presented in Fig. 4.1(a). The cross section is seen to be zero below a certain onset energy at ∼1.6 eV above which it increases smoothly with the collision energy. The red line represents a fit by the classical model cross section (Eq. (2.6)). The model provides a good description of the data, but small deviations are evident in the threshold region. These are ascribed to tunnelling, an effect not included in the classical picture. The threshold energy for detachment extracted from the fit is 2.3 ± 0.1 eV.

4.3.2 PO^-

Fig. 4.1(b) shows the cross section for neutralization of PO^-, which is the sum of the cross sections for pure detachment and dissociative detachment. The cross section for production of charged fragments is negligible in comparison and is therefore not shown. The neutralization cross section has an onset at ∼3.0 eV and exhibits a smooth behavior as a function of the collision energy with a maximum at ∼25 eV.

The red curve is a fit by the model cross section of Eq. (2.6). As seen, the agreement with the data is good, but the decreasing tendency at high energies is not reproduced by the model. The cross section decreases due to the smaller momentum transfer in the high energy collisions, and deviations occur since

this effect is neglected by the classical model. The value for the threshold energy extracted from the fit is 3.9 ± 0.2 eV.

To investigate the relative importance of pure detachment and dissociative detachment, grid measurements were carried out at four energies. For PO^-, the following electron-induced reactions are relevant:

$$\mathrm{PO^- + e^-} \rightarrow \begin{cases} \mathrm{PO + 2e^-} & \Delta E = \ \ 1.1\,\mathrm{eV} \quad \text{(a)} \\ \mathrm{P + O + 2e^-} & \Delta E = \ \ 7.2\,\mathrm{eV} \quad \text{(b)} \\ \mathrm{P^- + O + e^-} & \Delta E = \ \ 6.5\,\mathrm{eV} \\ \mathrm{P^+ + O + 3e^-} & \Delta E = 17.7\,\mathrm{eV} \quad \text{(c)} \\ \mathrm{P + O^- + e^-} & \Delta E = \ \ 5.8\,\mathrm{eV} \\ \mathrm{P + O^+ + 3e^-} & \Delta E = 20.9\,\mathrm{eV} \quad \text{(d)} \end{cases}, \tag{4.1}$$

where ΔE is the endothermic reaction energy. The reaction energies are calculated from the heats (or enthalpies) of formation as listed in the NIST Chemistry Webbook [160]. Here, also references to the original measurements of the heats of formation are found. In the energy range where the branching ratio measurements were performed, no electron-induced signal was observed in the peaks corresponding to detection of single P or O atoms, implying that channels (c) and (d) do not contribute to the total cross section at these energies. The extracted branching ratios are shown in Fig. 4.2(a). As seen, the dominant reaction channel is pure detachment with a branching ratio of more than 91% at all four energies. Above 25 eV, the branching ratio apparently begins to decrease as dissociative detachment is setting in. Note that even though this channel is more endothermic than channels (c) and (d), it contributes to the electron-induced reaction at lower energies than the latter channels.

4.3.3 PO_2^-

The neutralization cross section for PO_2^- is seen in Fig. 4.1(c). It increases smoothly with the collision energy after the onset at ~6.5 eV. The cross section for production of charged particles is negligible in the investigated energy range and is therefore not shown.

A fit by the model cross section (Eq. (2.6)) is displayed as a red curve in the figure. A threshold energy for detachment of 8.8 ± 0.2 eV is obtained by the fit. The fitted curve reproduces the data fairly well, but the measured cross section exhibits a more smooth behavior in the onset region than predicted by the model cross section.

Branching ratio measurements were carried out at energies below 35 eV.

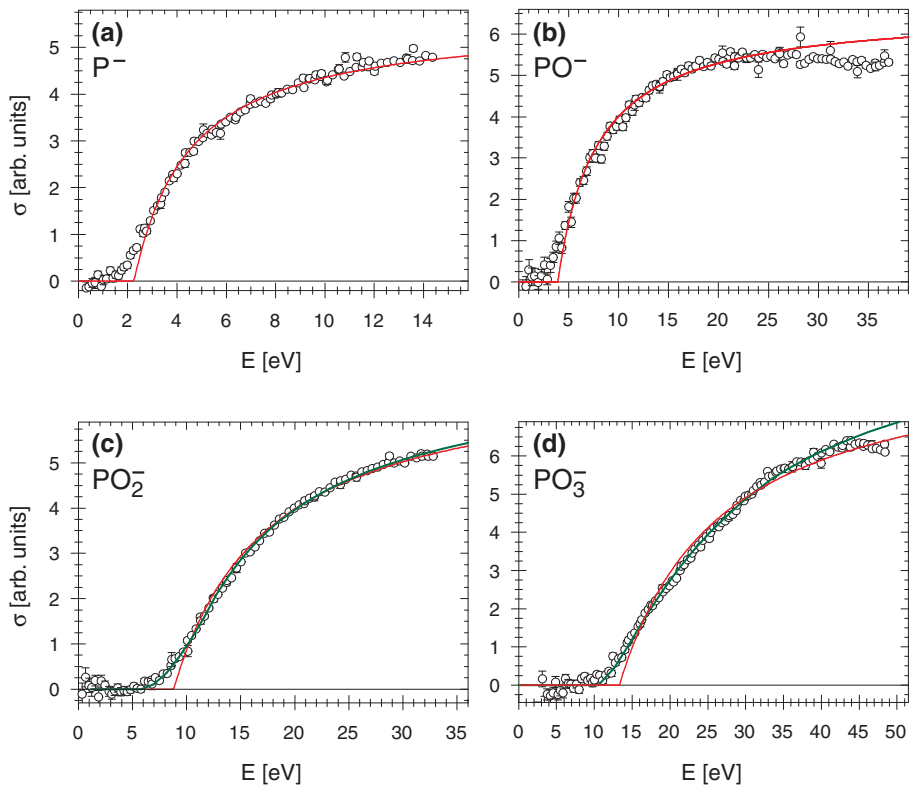

Figure 4.1: Cross section for neutralization as a function of the collision energy for **(a)** P^-, **(b)** PO^-, **(c)** PO_2^-, and **(d)** PO_3^-. The red curves represent fits of the cross section by the spherical classical model (Eq. (2.6)), while the green curves represent a model cross section for an elliptical reaction zone (see Sec. 4.4).

The reaction channels contributing to the neutralization cross section are:

$$PO_2^- + e^- \rightarrow \begin{cases} PO_2 + 2e^- & \Delta E = \ \ 3.6\ \text{eV} \quad (a) \\ PO + O + 2e^- & \Delta E = \ \ 9.0\ \text{eV} \quad (b) \\ P + O_2 + 2e^- & \Delta E = 10.0\ \text{eV} \quad (c) \\ P + 2O + 2e^- & \Delta E = 15.1\ \text{eV} \quad (d) \end{cases} . \tag{4.2}$$

Again, the endothermic reaction energies, ΔE, are calculated from heats of formation listed in Ref. [160]. As channels leading to production of charged fragments only constitute a small fraction of the electron-induced reactions,

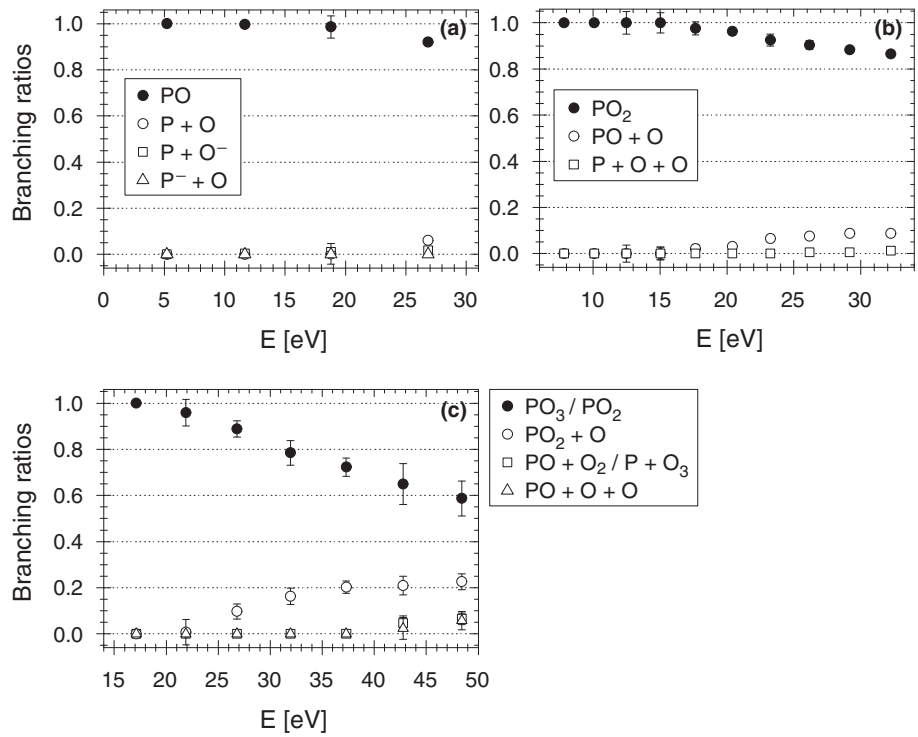

Figure 4.2: Branching ratios as a function of collision energy for **(a)** PO^-, **(b)** PO_2^-, and **(c)** PO_3^-.

they are not listed. The results of the measurements are seen in Fig. 4.2(b). Below 17 eV, neutralization solely stems from pure detachment (channel (a)), whereas detachment plus dissociation into PO + O makes up an increasing fraction of all events at higher energies. At 32 eV, the two channels account for $86 \pm 2\%$ and $8.8 \pm 1.0\%$ of all events, respectively. All other channels constitute the remaining flux, each contributing less than 2%.

4.3.4 PO_3^-

For PO_3^-, it is not possible to separate events leading to neutralization from those leading to one charged oxygen atom while the remaining fragments remain neutral (see Sec. 4.2). The cross section presented in Fig. 4.1(d) for PO_3^- is therefore the sum of the neutralization cross section and the cross section for production of one charged oxygen. At ~11.5 eV, the cross section has its

onset, and it continues to rise until ∼45 eV, whereafter it seems to decrease. As for PO_2^-, the cross section for production of other charged fragments than only one oxygen is almost negligible, and is therefore not shown.

The model cross section is found to give the best overall description of the data with a threshold energy of 13.3 ± 0.2 eV. However, it is evident that the model provides a poor description of the measured cross section which exhibits a markedly different overall shape than the model.

Measurements to identify the reaction channels in play were done at several energies in the range from 15 eV to 50 eV. It is found that the most important channels are:

$$PO_3^- + e^- \rightarrow \begin{cases} PO_3 + 2e^- & \Delta E = \ \ 5.0 \text{ eV} \\ PO_2 + O^- + e^- & \Delta E = \ \ 7.6 \text{ eV} \quad \text{(a)} \\ PO_2 + O^+ + 3e^- & \Delta E = 22.7 \text{ eV} \\ \\ PO_2 + O + 2e^- & \Delta E = \ \ 9.1 \text{ eV} \quad \text{(b)} \end{cases}, \tag{4.3}$$

where endothermic reaction energies are calculated with the use of Ref. [160]. The three reactions listed as channel (a) are unfortunately indistinguishable due to energy loss effects in the detector deadlayer (see Sec. 4.2). It is obvious from Fig. 4.2(c) that channel (a) is the dominant channel in the entire energy range, but the branching ratio for this channel decreases, as channel (b) is setting in. At all energies in this range, the two channels constitute more than 80% of the electron-induced reactions.

In the SSD pulse height spectra there are indications, however, that the main contribution to channel (a) might stem from pure detachment. A complete pulse height spectrum is shown in Fig. 4.3 together with the pulse height spectra of the electron-induced signal in the peak corresponding to detection of masses 79 amu and 63 amu for three different grids. From the complete pulse height spectrum, it is clear that the electron-induced signal peaks at higher energies than the background signal which most likely contains contributions from both mass 63 amu and 79 amu. As some of the electron-induced events stem from channel (b), flux must be transferred from the a neutral mass of 79 amu to mass 63 amu upon insertion of a grid in front of the detector. The figure clearly demonstrates that the electron-induced signal develops a tail to lower energies when grids are inserted, and, as expected, the tail is most pronounced at low transmissions. Furthermore, the rough energy calibration of the SSD pulse height spectrum shows that the tail appears in the energy range where a signal stemming from mass 63 amu would be expected ($E < \frac{63}{79} \cdot 1.72$ MeV $= 1.3$ MeV). As no contribution is found in this energy range in the spectrum taken without a grid, it is concluded that channel (a) is probably dominated by pure detachment.

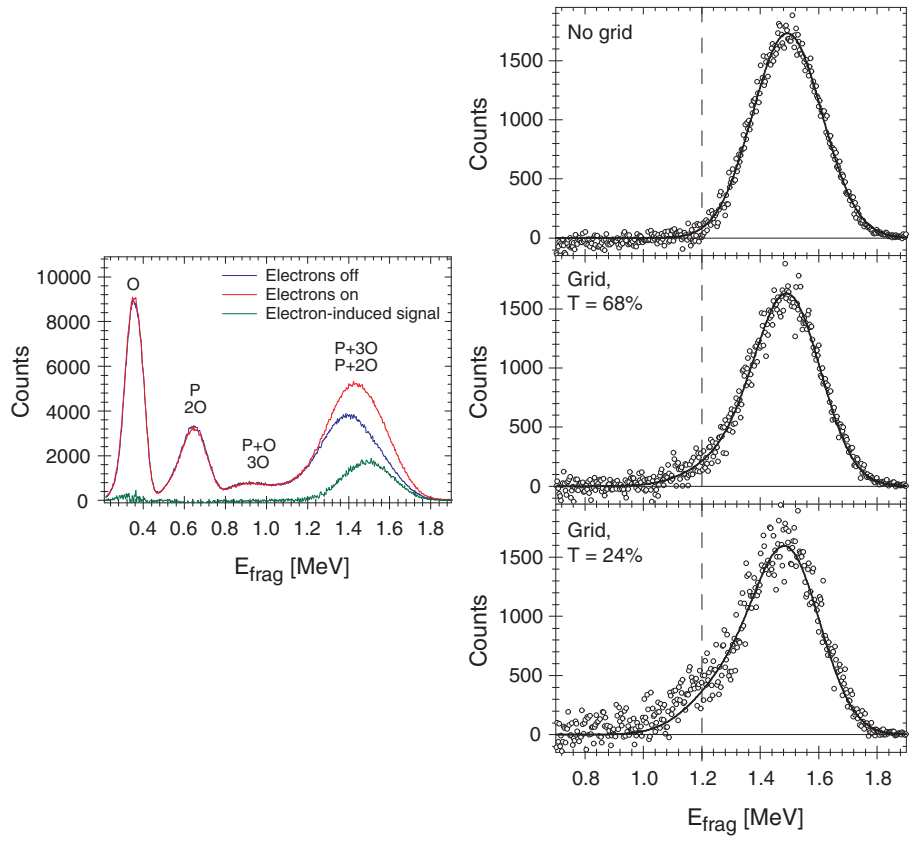

Figure 4.3: **Left:** Pulse height spectrum with and without electrons for PO_3^-, and the electron-induced signal. **Right:** Electron-induced signal for the peak corresponding to masses 63 amu and 79 amu for three different transmissions.

4.4 Discussion

4.4.1 Threshold energy

The threshold energy for electron-impact detachment of the four anions is related to the binding energy of the excess electron. The incoming electron interacts with the anions on a timescale much shorter than the timescales for molecular vibration and rotation, and hence, the molecular geometry remains unchanged during the detachment process. Therefore, it is relevant to compare the threshold energy for detachment to the *vertical detachment energy*

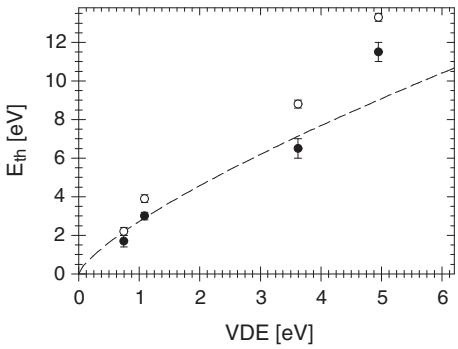

Figure 4.4: Measured threshold energy for detachment of the PO_n^- anions as a function of the vertical detachment energy (VDE) [162–165]. Filled circles are the onsets as read from the cross section plots, whereas the open circles represent the threshold energies obtained by a fit to the classical model cross section. The dashed line is the $2^{1/4}(\mathrm{VDE})^{3/4}$ prediction (see text for details).

(VDE) rather than simply the adiabatic electron affinity (EA) (see Ref. [161] for definitions). However, looking at the photoelectron spectra for PO^- [162], PO_2^- [163], and PO_3^- [164], only PO_2^- exhibits a difference between the EA and VDE, which is found to be 0.2 eV. The threshold energies are shown as a function of the VDE in Fig. 4.4. Here, both the threshold energy obtained from a direct reading of the cross section onsets as well as the values obtained from the fits by Eq. (2.6) are plotted. The difference reflects the discrepancies between the measured cross section and the model in the onset region.

For atomic anions, the threshold energy E_{th} may be related to the binding energy of the excess electron, E_{b}, and the extent of the binding potential, d, through the equation $E_{\mathrm{th}} = \sqrt{E_{\mathrm{b}}/d}$ (in atomic units) [10, 71, 73]. In the case of weakly bound atomic anions, the spatial extent of the binding potential scales according to $d \simeq 1/\sqrt{2E_{\mathrm{b}}}$ [166], and combining these two relations gives the following expression for the threshold energy:

$$E_{\mathrm{th}} = \sqrt{\frac{E_{\mathrm{b}}}{d}} \simeq 2^{1/4} E_{\mathrm{b}}^{3/4}. \tag{4.4}$$

For molecular anions, the binding energy is replaced by the VDE. This expression is also shown in Fig. 4.4. It is seen that this expression gives a fairly good estimate of the threshold energy for P^-, PO^-, and PO_2^-, whereas for PO_3^- the measured threshold energy is somewhat higher than the predicted one.

A phenomenon that can cause a higher threshold energy for PO_3^- than expected is the anion polarizability. As the incoming electron approaches the

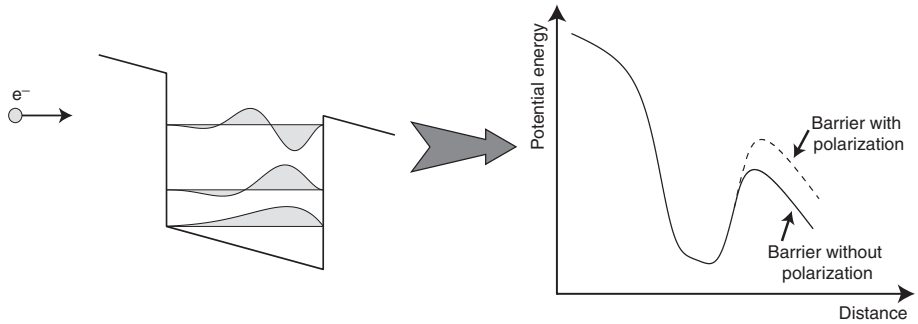

Figure 4.5: Schematic drawing of the binding potential of the excess electron. The target electrons respond to the incoming electron by moving to one side of the potential, hence leading to a polarization of the anion. The height of the potential barrier that must be penetrated or overcome in order to escape increases (dashed line) relative to a potential which ignores the polarization (solid line).

anion, the target electrons respond to its presence by moving towards the opposite side of the binding potential as sketched in Fig. 4.5. The electric field of the projectile electron creates a barrier in the potential through or over which electrons might escape. However, the increased electron density in the direction opposite the approaching electron makes the barrier higher relative to the situation where the polarizability is not taken into account. Thus, the incoming electron must carry more energy to cause detachment than expected from a model ignoring polarization of the anion. A similar effect has been observed for strong-field ionization of small metal clusters [167]. As compared to a calculation relying on a single-active-electron picture, a dramatic suppression of the ionization was observed there. The discrepancy was attributed to the cluster polarizability, and when including this effect in the calculation, better agreement with the observations was obtained.

4.4.2 Cross section behavior

For P^- and PO^-, the overall shape of the neutralization cross sections are well-described by the classical model cross section (Eq. (2.6)). This model assumes that a detachment reaction occurs with constant probability if the incoming electron comes within a certain distance of the anion. However, for PO_3^-, and partly PO_2^-, the model is insufficient to represent the overall shape of the measured cross section, which displays a much smoother behavior than the model in the onset region. A similar behavior of the cross section is further seen for p-benzoquinone ($C_6H_4O_2^-$) [57], and also for some of the hydroxide-water

cluster anions presented in the next chapter. The discrepancy between the data and the model cross section might be attributed to the geometry of the molecular systems. In the model used above, the reaction zone is chosen to be a sphere with radius $R_{\text{th}} = 1/E_{\text{th}}$, which is reasonable for the spherical symmetric atomic anions, but the assumption becomes problematic for, for example, planar molecules like p-benzoquinone and PO_3^-. As already mentioned, the nuclei can essentially be considered fixed in space during the scattering process. The detachment process is thus likely to depend on the orientation of the molecule relative to the impacting electron. The reason is twofold: Firstly, the Coulomb barrier experienced by the incoming electron is no longer isotropic, but depends rather on the direction of the incoming electron with respect to the orientation of the molecule; secondly, the binding force experienced by the detached electron depends on the direction from which it leaves the molecule. The combination of these effects leads to a dependence of the threshold energy on the molecular orientation, and the result is a smearing of the cross section. As a consequence, the model cross section no longer reproduces the observed behavior.

To investigate how an orientational effect as described above might influence the cross section shape, the classical model is extended so that the reaction zone is an ellipsoid instead of a sphere. The ellipsoid is characterized by the lengths of three semi-axes, which in the following are collectively denoted by $\boldsymbol{a}$, and the orientation of the ellipsoid with respect to a space-fixed frame is described by the three Euler angles, α, β, and γ, collectively referred to as $\boldsymbol{\Omega}$. The reaction probability is now given by:

$$P(E, \boldsymbol{\Omega}, \boldsymbol{a}, \rho, \phi) = \begin{cases} p, & \exists\theta : D(E, \rho, \phi, \theta) \leq R(\boldsymbol{\Omega}, \boldsymbol{a}, \phi, \theta) \\ 0, & \text{otherwise} \end{cases}, \tag{4.5}$$

where $D(E, \rho, \phi, \theta)$ is the distance between the incoming electron and the center of the ellipsoid, and $R(\boldsymbol{\Omega}, \boldsymbol{a}, \phi, \theta)$ describes the surface of the ellipsoid (see Fig. 4.6). ρ is the impact parameter of the incoming electron, and θ and ϕ are the polar and azimuthal angles, respectively (see Fig. 4.6). For a given orientation, $\boldsymbol{\Omega}$, of the anion, the cross section is given by:

$$\sigma(E, \boldsymbol{\Omega}, \boldsymbol{a}) = \int_0^{2\pi} \int_0^{\infty} P(E, \boldsymbol{\Omega}, \boldsymbol{a}, \rho, \phi)\, \rho \, \mathrm{d}\rho \, \mathrm{d}\phi. \tag{4.6}$$

In the ion beam, the ions have random orientations, and the above cross section must be averaged over all orientations before it can be compared directly to the data. The orientational averaged cross section is computed according

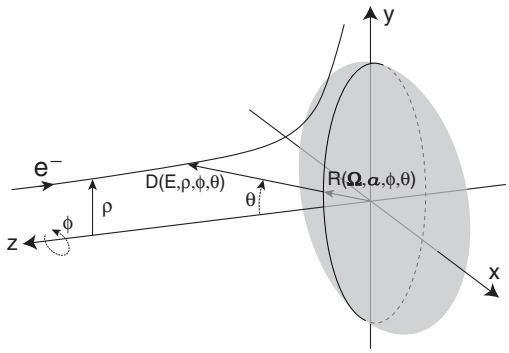

Figure 4.6: The scattering of an electron in the field of a central potential. The ellipsoidal reaction zone is drawn along with the definitions of different parameters.

to:

$$\langle \sigma(E, \boldsymbol{a}) \rangle = \frac{1}{8\pi^2} \int_0^{2\pi} \int_0^{\pi} \int_0^{2\pi} \sigma(E, \boldsymbol{\Omega}, \boldsymbol{a}) \sin\beta \, \mathrm{d}\gamma \, \mathrm{d}\beta \, \mathrm{d}\alpha. \tag{4.7}$$

The reaction probability, $P(E, \boldsymbol{\Omega}, \boldsymbol{a}, \rho, \phi)$, is determined numerically in a MATLAB routine, which also calculates both the orientation dependent and the orientational averaged cross sections through numerical integration. It must be noted that the shape of the cross section only depends on the ratios of the lengths of the three semi-axes, implying that it is determined by only two parameters.

In Fig. 4.1, the model cross section for an elliptical reaction zone is shown (green curves) together with the experimental data. For PO_2^-, the relation between the lengths of the three semi-axes was set to 1:0.5:0.5, whereas it is 1:1:0.3 for PO_3^-. These relations were obtained by comparing the measured cross sections to numerically calculated cross sections for different ellipsoids. In addition, the obtained ellipsoids are similar to the shapes of the anions which for PO_2^- is a bent geometry with a O–P–O bond angle of 119° [163] and for PO_3^- is a planar geometry with D_{3h} symmetry [164]. The figure shows that the ellipsoidal model gives a much better agreement with the measured cross section than the spherical model, implying that an orientational effect could be the origin of the observed cross section shape.

4.4.3 Dianions

In contrast to NO_2^- and NO_3^-, the cross sections of PO_2^- and PO_3^- do not show any sign of dianion formation. As the electronic structure of the two

sets of anions are similar, it was speculated that dianion states of PO_2 and PO_3 might be populated in scattering events as was the case for the analogous NO_2 and NO_3. For comparison, resonance structures in the detachment cross section are observed for the isoelectronic species NCO^- and NCS^-, and the low-energy resonance position of NCO^{2-} is a little higher than that of NCS^{2-} owing to the reduced Coulomb repulsion for the latter species [49]. In the case of NO_2^-, two resonance states were observed: one at 7.2 eV above the anion ground state and another at 16.5 eV [21]. Drawing parallels with the findings for NCO^- and NCS^-, two resonance states would also be expected for PO_2^-. However, if existing, the low-energy state of PO_2^{2-} is likely not to be seen in the experiments: presumably, the resonance position will be lower than the 7.2 eV seen for NO_2^- due to the reduced inter-electronic Coulomb repulsion in PO_2^-, and decay of PO_2^{2-} into detectable neutral fragments, that is $PO_2 + 2e^-$, is therefore likely to be prohibited. This is attributed to the fact that the electron binding energy of PO_2^- is 3.4 eV [163], 1.1 eV higher than NO_2^- [168], and as kinetic energy for the two escaping electrons further has to be provided, the emission of two electrons is probably not possible.

The argument given above does not exclude the possibility of observing a dianion state of PO_2 corresponding to the higher-lying dianion state of NO_2. Similarly, the observation of a dianion state of PO_3 analogous to that of NO_3^{2-} at 18.6 eV above the NO_3^- ground state cannot be ruled out on the grounds of energy considerations. The fact that no such states are observed for neither PO_2^- nor PO_3^- may be ascribed to several effects: (i) the states simply do not exist, (ii) the dianions decay by either single-electron autodetachment or Coulomb explosion in which cases no detectable fragments emerge from the process, (iii) penetration of the Coulomb barrier at the relevant energies is suppressed.

4.5 Conclusion

Electron-impact detachment of PO_n^- ($n = 0$–3) was studied for collision energies in the range 0 eV to about 40 eV. All cross sections exhibit a well-defined onset at an energy significantly larger than the binding energy of the excess electron. The measured cross sections were compared to a classical model cross section, which provided a good description of the cross section behavior of the smaller ions. However, for PO_3^-, the model cross section clearly failed, which was ascribed to the cross section being dependent on the orientation of the molecular anion with respect to the incoming electron.

Measurements to extract the branching ratios for the molecular anions were conducted, and it was found that pure detachment was the dominant reaction

channel in all cases. The second most important reaction was dissociative detachment where one of the P–O bonds was broken.

In contrast to their isoelectronic species NO_2^- and NO_3^-, neither PO_2^- nor PO_3^- is seen to form transient dianion states when bombarded with electrons.

CHAPTER 5

Electron-impact detachment of $OH^-(H_2O)_n$ ($n = 0$–4)

5.1 Introduction

In this chapter, electron impact on small $OH^-(H_2O)_n$ clusters is investigated. These microsolvated ions are abundant in the atmosphere of the Earth and play a role for the ion chemistry [169, 170]. Furthermore, these cluster ions have been suggested to act as condensation nuclei in formation of clouds [171, 172]. In connection with electron-anion collisions, these clusters are interesting since they exhibit properties which are markedly different from all other anions studied prior to this work. First of all, the water molecules are bound to the hydroxide anion by hydrogen bonds. As a result, the energy required to break the OH^--water bond is of the order tenths of eV, an amount much smaller than the excess electron binding energy, which is of order eV. Hence, the clusters are fragile compared to covalently bound anions, where the electron binding energy is generally smaller than dissociation energies. Consequently, the dissociation pattern of the hydroxide-water clusters might be very different from those of covalently bound systems. Secondly, it is interesting to investigate if the detachment cross section of more complex targets follows the same general behavior as for the atomic and polyatomic anions. The $OH^-(H_2O)_n$ clusters present an excellent opportunity to study electron collisions with targets of increasing complexity by successively adding waters to the system.

In the following, it will be shown that despite the large complexity of the clusters, the detachment cross section behavior is very similar to that of small

anions. The main electron-induced reactions are found to be many-body fragmentation in contrast to most results on polyatomic anions where pure electron detachment is dominant.

5.2 Experiment

The $OH^-(H_2O)_n$ ions were formed from water vapor in a cold-cathode ion source. Discharge currents of 3.5–6 mA produced ion beam currents ranging from ~2 nA for $OH^-(H_2O)_4$ to 32 nA for OH^-. After preacceleration to 150 keV, the ions were mass selected by an analyzing magnet and injected into the ASTRID storage ring. After injection, the ions were further accelerated to final energies ranging from 1.4 MeV for $OH^-(H_2O)_4$ to 5.7 MeV for OH^-. The ion beam and the electron beam were merged 5 seconds after extraction of the ions from the ion source, at which time the ions are expected to be vibrationally cold.

For the lightest ions ($n \leq 2$), a 4×6 cm^2 energy sensitive solid state surface-barrier detector (SSD) located 6 m after the electron cooler was used to detect the neutral fragments. For the heavier clusters, a circular SSD of 4 cm diameter was employed, as this detector had a better energy resolution needed to separate the individual water peaks. Due to the finite energy resolution of both detectors, only $n + 1$ peaks appeared in the energy spectrum recorded with $OH^-(H_2O)_n$ stored in the ring. The masses of O, OH, and H_2O are very similar, and within the resolution of the detector the cluster anions therefore resemble a system, X^-_{n+1}, consisting of $n + 1$ equally heavy entities, X. Essentially, only the heavy oxygen atoms can be traced, and it is not possible to conclude what happens to the hydrogens, that is if the OH and water molecules remain intact or dissociate upon electron impact. Thus, the X entity used in the following represents O, OH, O + H, OH + H, O + H_2, O + H + H, or H_2O. For the same reason, the meaning of 'total dissociation' in the present chapter is that the X_n cluster fragments into n X, e.g. all oxygen atoms are separated.

As the ion beam currents were too low to be measured (below 50 nA), it was not possible to measure the cross sections on an absolute scale, and thus only relative cross sections are presented below along with the branching ratios for the different electron-induced reactions.

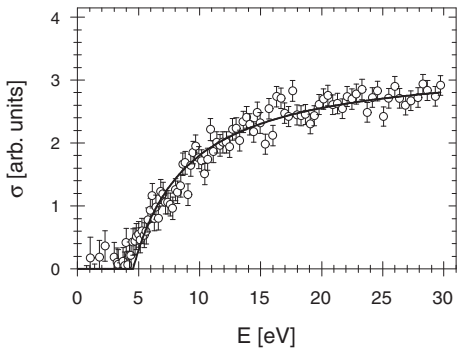

Figure 5.1: Total cross section for reactions leading to neutrals from electron impact on OH^- as a function of the collision energy. The solid line represents a fit by the model cross section (Eq. (2.6)).

5.3 Results

5.3.1 OH^-

Figure 5.1 shows the total cross section for reactions leading to pure detachment (OH), detachment plus dissociation (O + H), and neutral oxygen as a single neutral fragment ($O + H^-$ or $O + H^+$ from double detachment). Only the total cross section is presented since the O peak was not clearly separable from the OH peak, and since the H peak could not be resolved. However, it was found that the main contribution stemmed from pure detachment as the signal in the partially resolved O peak was negligible. The cross section is well described by the classical model of Eq. (2.6), and a fit by this model yields a threshold energy for detachment of 4.5 ± 0.2 eV. As compared to the fit, the measured cross section has a small tail to lower values near threshold, and from a direct reading the onset is found to be roughly 4 eV.

A previous experiment at ASTRID obtained an value of ∼3.7 eV for the detachment threshold [11]. The agreement between the two sets of data is found to be good, and the difference in threshold value thus reflects the uncertainty in the determination of the onset energy.

5.3.2 $OH^-(H_2O)$

The results for $OH^-(H_2O)$ are seen in Fig. 5.2(a). Pure detachment and/or dissociative detachment is clearly seen to be the dominant reactions over the entire energy range. The cross section for neutralization has an onset of ∼6 eV

and increases until 40 eV where a plateau is reached. The classical model provides a fair description of the overall shape of the cross section although the threshold value of 7.9 ± 0.2 eV obtained in the fit is somewhat higher than the true onset.

The cross section for reactions leading to only one charged X fragment opens up at higher energies (around 35 eV), but the cross section for these reactions is low compared with the one for detachment. Since the ionization energy of OH and H_2O is 13.0 eV [173] and 12.6 eV [174], respectively, energy for double detachment is available at the cross section onset of ∼35 eV, and thus the charged fragment is likely to be OH^+ or H_2O^+.

To elucidate whether pure detachment or detachment plus dissociation is the dominant channel, branching ratios were determined by the grid technique described in section 3.3.2. The result is shown in Fig. 5.4(a). Detachment plus dissociation is found to be the dominant channel, the average branching ratio being ∼85%, whereas pure detachment contributes $5 \pm 4\%$ to the total events and reactions leading to a single charged X fragment contributes $10 \pm 4\%$. The tendency of the clusters to dissociate is also seen in photodetachment studies where a photon of energy 4.8 eV (258 nm) causes both detachment and dissociation of the anionic system [175]. Looking at the energy levels involved in the process, it is plausible that detachment and dissociation is the most likely process. Several experimental and theoretical studies have addressed the question of the hydration energies of OH^-, and the results are quite similar [176–184]. As both vertical detachment energies for the clusters and hydration energies for OH^- are needed to obtain the energy level diagram, the work of Masamura [176] is used since all desired energies are calculated using the same method and level of theory. At the MP2/aug-cc-pVDZ level of theory, Masamura found a value of 3.6 eV for the vertical detachment energy and a hydration energy of $\Delta H_{1,0} = 1.17$ eV for $OH^-(H_2O)$ [176] (Fig. 5.3). Thus, the neutral state formed after electron detachment from the anion will be located 3.6 eV above the anionic ground state whereas the energy level of $OH^- + H_2O$ is placed 1.17 eV above the anion. As the electron affinity of OH is 1.828 eV [185], the energy level for the neutral system of $OH + H_2O$ is situated 1.17 eV + 1.828 eV = 3.00 eV above the ground state of $OH^-(H_2O)$ (see Fig. 5.3). Therefore it is found that the neutral state, formed upon electron detachment, lies ∼0.6 eV above the dissociation limit of $OH + H_2O$. Hence, dissociation of the formed neutral cluster is energetically possible in accordance with the measured branching ratios.

5.3.3 $OH^-(H_2O)_2$

The cross sections for different reaction channels of $OH^-(H_2O)_2$ are shown in Fig. 5.2(b). The onset for neutralization is ∼8.5 eV, and the cross section

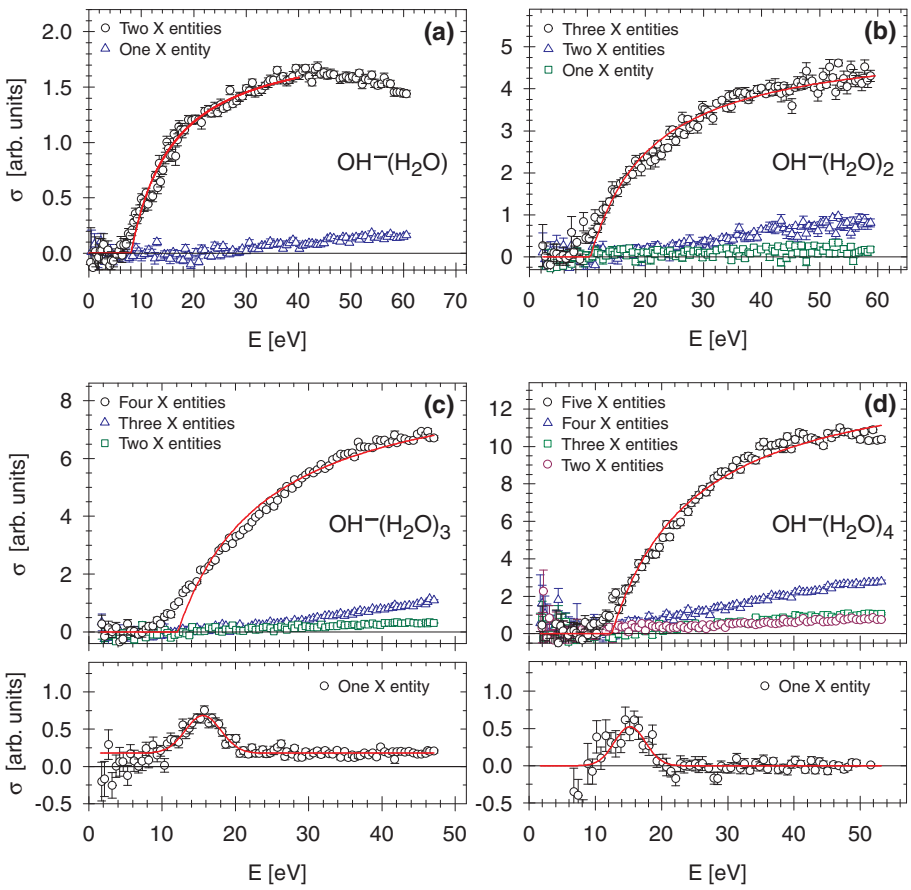

Figure 5.2: Cross sections for the different electron-induced reactions of **(a)** $OH^-(H_2O)$, **(b)** $OH^-(H_2O)_2$, **(c)** $OH^-(H_2O)_3$, and **(d)** $OH^-(H_2O)_4$. The neutralization cross section (the sum of the cross sections for detachment and dissociative detachment) is clearly the dominant for all ions. For $OH^-(H_2O)_3$, a resonance is seen at 15.6 eV in the cross section corresponding to the production of only one neutral X fragment. This is also the case for $OH^-(H_2O)_4$, where the resonance position is 15.2 eV.

n	VDE	$\Delta H_{n,0}$	E_{dis}
1	3.62	1.17	0.63
2	4.56	2.03	0.70
3	5.18	2.76	0.59
4	5.81	3.44	0.54

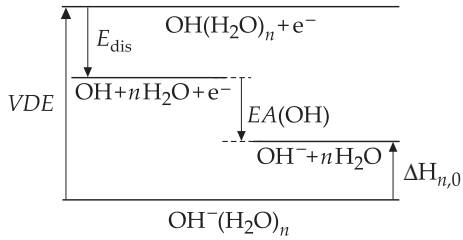

Figure 5.3: **Left:** Vertical electron detachment energies (VDE), total hydration energies for OH^- in $OH^-(H_2O)_n$ ($\Delta H_{n,0}$), and the dissociation energies (E_{dis}) of the neutral clusters in the anion geometry, all values in eV [176]. **Right:** Energy level diagram for $OH^-(H_2O)_n$, showing the location of the different states relative to one another.

increases smoothly up to 50 eV after which point it reaches a constant value. A fit to Eq. (2.6) yields a threshold energy of 10.1 ± 0.4 eV, which is somewhat higher than the onset since the measured cross section rises more smoothly than the model cross section. Such deviations near the onset may be explained by the electron tunnelling out of the binding potential, an effect inherently not included in a classical model.

Processes leading to a single charged X entity has an onset of ~20 eV followed by a smooth increase, again reaching a constant level at 50 eV. The energy difference between this onset and the threshold energy for detachment is comparable to the ionization potentials for OH and H_2O, thus making double electron release the plausible reaction channel. Reactions in which only one X fragment is detected are by comparison negligible.

Branching ratios for the different channels are shown in Fig. 5.4(b). Detachment plus total dissociation (i.e. dissociation into 3 separate X fragments) is the main channel, on average contributing ~80% to the total events. The second most important channel corresponds to total dissociation, the only difference being the production of a charged X entity. This channel opens at 20 eV and reaches a branching ratio of 20% at 90 eV. In total, all other channels contribute less than 10% at all energies above 20 eV. Total dissociation is also observed upon photodetachment, where the reaction pathway $OH^-(H_2O)_2 + h\nu \rightarrow OH + 2H_2O + e^-$ is seen for a photon energy of 4.8 eV (258 nm) [186]. Furthermore, the photodetachment data showed no evidence of two-body dissociation. Again, the tendency for dissociation can be explained by looking at the energetics involved in the processes. From the vertical detachment energy for the monoanion and the total hydration energy found in Fig. 5.3, it is concluded that the energy of the neutral cluster formed after a vertical transition from the anionic ground state is higher than the dis-

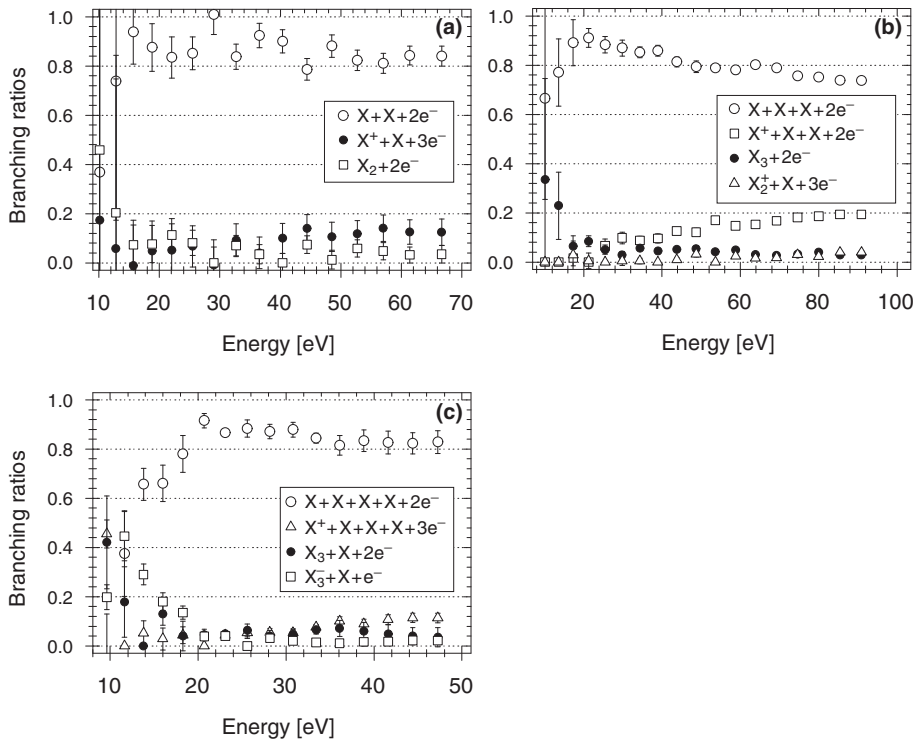

Figure 5.4: Branching ratios as a function of the collision energy for different electron-induced reactions of **(a)** $OH^-(H_2O)$, **(b)** $OH^-(H_2O)_2$, and **(c)** $OH^-(H_2O)_3$. In all cases, the dominant channel is detachment followed by $n+1$-body fragmentation, n being the number of water molecules.

sociation limit by ∼0.7 eV (see Fig. 5.3). Thus, total dissociation of the neutral cluster into its constituent molecules is energetically possible.

5.3.4 $OH^-(H_2O)_3$

Cross sections for different electron-induced reactions of $OH^-(H_2O)_3$ are shown in Fig. 5.2(c). The onset of the detachment cross section is at ∼9 eV from where the cross section continues to rise smoothly throughout the energy range. Also shown in the figure is a fit by the classical model of Eq. (2.6) which yields a threshold energy of 11.4 ± 0.7 eV. In this case, however, the shape of the measured cross section is not particularly well represented by the classical model, as the measured one exhibits a more smooth behavior.

The cross section for reactions resulting in one charged X fragment opens up at 20 eV and continues to increase in the measured energy interval up to 50 eV. The same behavior is found for the cross section for channels leading to only two neutral X fragments, though the increase with energy is somewhat smaller.

An interesting feature at ∼15 eV is seen in the cross section for reactions leading to a single neutral X fragment. This resonance is attributed to the formation and decay of the doubly charged negative ion of $OH(H_2O)_3$. When fitted with a Gaussian function, the position of the resonance is found to be 15.6 ± 0.2 eV with a FWHM of 5.7 eV. The width is determined by Franck-Condon factors, the dianion lifetime, and the energy resolution and may thus only give a lower bound of the lifetime of the dianion. On account of the high energy, the resonance state is believed to be an excited state of the dianion (see discussion section). As the state is found below the threshold energy for multiple electron release, the transient dianion decays into $X_3^- + X + e^-$. The decay could be interpreted as $OH^-(H_2O)_2 + H_2O + e^-$.

The branching ratios are found in Fig. 5.4(c). Clearly, detachment followed by four-body fragmentation is the dominant channel with an average of ∼80% for $E > 10$ eV. It is seen that the branching ratio for this reaction rises from 10 eV to 20 eV where a constant level is reached. In the same energy range, the branching ratio for the process leading to a single neutral X fragment decreases from ∼40% to ∼0%, which is due to the resonance detected in this decay channel. Finally, the branching ratio for the channel corresponding to total dissociation into three neutral fragments and one charged X fragment increases with energy to a final level of 10 ± 4%, which is also evident from the cross sections shown in Fig. 5.2(c). As for the smaller clusters, the energy level diagram for the systems involved provides some insight into the process. The values for the vertical detachment energy and the total hydration energy place the neutral cluster formed upon electron detachment above the dissociation limit by ∼0.6 eV (Fig. 5.3). Hence, energy for total dissociation is available.

5.3.5 $OH^-(H_2O)_4$

The cross sections for $OH^-(H_2O)_4$ are shown in Fig. 5.2(d). The results are quite similar to the results for the smaller clusters: Detachment and/or dissociative detachment are the leading channels with a large cross section compared to the other reaction channels. At ∼11.5 eV, the detachment cross section has its onset, and it continues to increase until ∼40 eV, where it seems to level off. The model cross section is found to give the best overall description of the data when the threshold energy is set to 12.1 ± 0.5 eV. Still, the fit is not quite

satisfactory, as the data clearly lie below the curve in some regions and above in other regions.

The cross section for reaction pathways leading to the formation of a single charged X fragment has an onset of ∼15 eV, and rises smoothly with increasing energy. A similar behavior is found for the cross sections for channels giving two or three neutral X fragments: These cross sections also have onsets of ∼15 eV, but increase more slowly with energy.

A resonance is found in the cross section for processes leading to a single neutral X fragment. This resonance can be fitted with a Gaussian function yielding an energy of 15.2 ± 0.4 eV and an FWHM of 5.5 eV. The resonance is an indication of dianion formation, and it is believed to be an excited state of the dianion of $OH(H_2O)_4$, owing to the high energy of the resonance (see discussion section). As multiple electron release is energetically forbidden, the dianion decays into $X_4^- + X + e^-$, which could be interpreted as $OH^-(H_2O)_3 + H_2O + e^-$.

To determine the branching ratios, measurements were carried out at four energies between 15 eV and 45 eV, but conclusions were difficult to draw due to the many reaction channels involved. However, the system shows a marked tendency to dissociate totally upon electron impact detachment as the branching ratio is ∼60% on average. Again, this tendency is supported by a comparison of the vertical detachment energy and the total hydration energy (see Fig. 5.3). Energetically, the neutral cluster formed upon detachment lies above the totally dissociated neutral cluster by an amount of ∼0.5 eV, which makes total dissociation energetically possible. Other channels contribute by less than 40% in total.

5.4 Discussion

5.4.1 Thresholds

None of the cross sections presented above could be put on an absolute scale, as the ion currents in the storage ring were too low to be measured. An estimate might however be given from the classical model (Eq. (2.6)), in which $R_{th} = 1/E_{th}$ in atomic units. All absolute detachment cross sections measured at ASTRID have been compared to the non-resonant model cross section, and an average value of the scaling factor p of ∼0.4 was found [47]. Using this value of p together with the determined values of the threshold energy, the absolute detachment cross sections for the five anions can be estimated, and the results are plotted in Fig. 5.5. It is emphasized that the presented curves only serve as estimates, and a comparison with results previously published on OH^- [11] shows that the estimate for OH^- is correct within a factor of

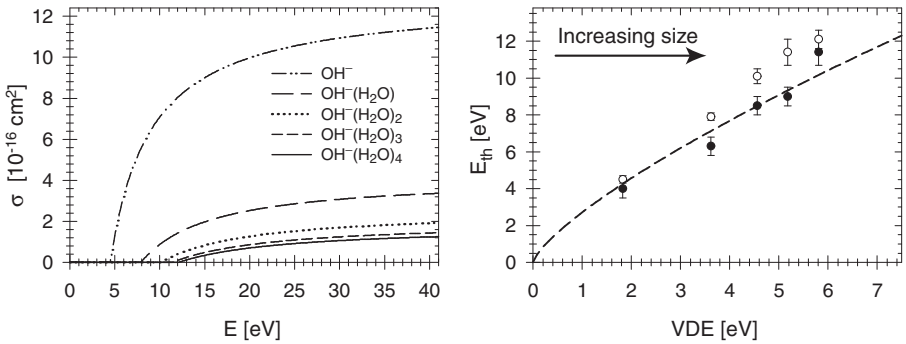

Figure 5.5: **Left:** Absolute cross sections as estimated from the model cross section of Eq. (2.6) with $p = 0.4$ for the five anions. **Right:** Threshold energies for detachment for the five ions as a function of the vertical detachment energy. The solid points are obtained when the onset energy is read directly from the cross section data, whereas the open points represent the threshold energy obtained from a fit to Eq. (2.6). For comparison, the classical over-the-barrier estimate of the threshold energy (Eq. (4.4)) is drawn (dashed line).

two. Measurements of absolute cross sections for C_n^-, Ag_n^- and Al_n^- [56, 58] have been compared to a scaling law by Robicheaux [79, 80], where the cross section is inversely proportional to the square of the *binding* energy of the excess electron. The predicted cross section magnitude deviated no more than a factor of five from the measured one. According to the model cross section used here, the magnitude scales inversely proportional to the *threshold* energy squared, but the difference between the two scaling laws is small. Therefore, the estimates given here are expected to be correct within the same range as Robicheaux's scaling law, namely a factor of five.

For each of the clusters, the threshold energy for detachment can be compared to the binding energy of the excess electron. As the interaction time between the anionic clusters and the electron is on the femtosecond scale, the positions of the nuclei remain fixed during the collision, and hence the vertical detachment energy, VDE, is taken as the electron binding energy of the molecular species. As already mentioned, the electron affinity of OH was determined through threshold photodetachment to be 1.828 eV [185], and at the MP2/aug-cc-pVDZ level of theory, Masamura calculated the vertical detachment energies for $OH^-(H_2O)_n$, $n = 1$–5 [176]. In Fig. 5.5, the threshold energy for electron-impact detachment of the five systems is plotted as a function of the vertical detachment energy. The two sets of points represent threshold energies obtained from fits to Eq. (2.6) and by direct readings of the cross section

onset. The difference between the two sets reflects the discrepancy between the model cross section and the data in the threshold region.

For atomic anions, the threshold energy may be predicted from the binding energy or vertical detachment energy of the excess electron according to Eq. (4.4). For comparison, this prediction is represented by a dashed line in Fig. 5.5. As seen, the expression gives a fair estimate of the threshold energy for the five clusters.

For some of the clusters, and for $OH^-(H_2O)_3$ in particular, the classical model cross section does not represent the measured cross section to a satisfactory extent as seen in Fig. 5.2. The measured cross sections have a much smoother rise than predicted by the model, which might be attributed to different effects. Firstly, electron tunnelling out of the binding potential can give rise to a low-energy tail in the near-threshold region. Secondly, the clusters have a complex structure as illustrated in Fig. 5.6, which shows the structure of $OH^-(H_2O)_3$ as calculated with GAUSSIAN-98 [187] at the B3LYP/6-311+G(d) level of theory. Looking at this structure, it might be speculated that the detachment threshold energy depends on the orientation of the cluster anion with respect to the impacting electron. Since the cluster anions have random orientations in the beam, the measured cross section is averaged over all orientations, which results in a smoother onset than predicted by the model cross section as also shown in the previous chapter. However, unlike for the PO_n^- anions, the structure of the present clusters is not really well-defined [184] implying that the ion beam contains a variety of different isomers, as also noted by Clements and coworkers [186]. Therefore, the present data are not compared to the ellipsoidal model introduced in the previous chapter, as there is no obvious choice for the ellipsoid geometry for these clusters.

Furthermore, it was found that the detachment process was followed by total dissociation of the clusters into the constituent molecules of OH and H_2O, the branching ratio being $\sim$75% for $n = 1$–4. As the clusters are held together by hydrogen bonds, the binding energy of a single water molecule to the cluster is small ($\sim$0.2 eV), and the clusters therefore dissociate upon electron bombardment. This is in contrast to covalently bound systems like O_3^-, NO_3^-, SO_2^- [47], NO_2^- [21], and PO_n^- (see Chap. 4 of this thesis) where total dissociation into atomic constituents is not observed. Total dissociation for the clusters was also observed in combination with the production of a single charged fragment, and this channel was found to be the second most important channel. This process can be understood in terms of double electron release from the OH molecule. Prior to the detachment process, the water molecules are oriented with one of their hydrogen atoms pointing to the negatively charged OH. Since the double electron detachment process is fast compared to the timescale for reorientation of the water molecules, the geometry of the

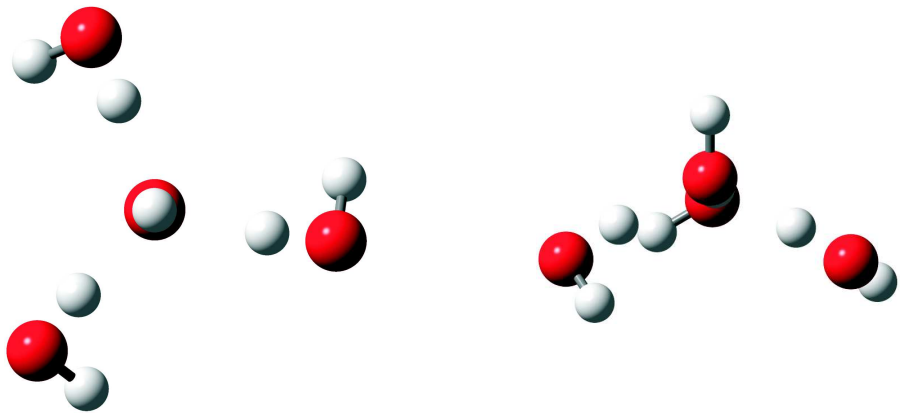

Figure 5.6: The geometry of $OH^-(H_2O)_3$ as calculated with the GAUSSIAN-98 [187] at the B3LYP/6-311+G(d) level of theory. The geometry is shown from two different angles of view.

system is unchanged immediately after double detachment, but now the hydrogen atoms are pointing towards the positively charged OH molecule. The interactions between the formed cation and the hydrogens are repulsive, thus leading to dissociation of the cluster.

5.4.2 Resonances

Resonances are found in the cross sections for $n = 3$ and $n = 4$, which are attributed to the formation of dianions. The lack of resonance states in the smaller clusters may be due to a combination of effects as will now be discussed.

As discussed in Chap. 2 of this thesis, small doubly charged anions are unstable in the gas phase due to the large Coulomb repulsion between the excess electrons. However, dianion states can be embedded in the electronic continuum of the singly-charged parent. If such states lie below the top of the repulsive Coulomb barrier, they have a finite lifetime determined by the excess electron tunnelling out through the barrier. In this case, the dianion state might be populated by bombarding the monoanion with electrons in which case a resonance appears in the scattering cross section.

In the present case, it is believed that for $n = 3$ the cluster becomes large enough for the Coulomb energy to be reduced sufficiently to bring an energy level of the dianion below the top of the repulsive Coulomb barrier. As the addition of a fourth water stabilizes the system even further, a resonance might also appear in the cross section for $OH^-(H_2O)_4$, which indeed is found to be

the case (see Fig. 5.2(d)). Since the dianionic state in both cases is located as high as ∼15 eV above the monoanion, the dianions are possibly formed in an excited state. This is supported by the fact that excited state resonances are found in the same energy region for, for example, NO_2^- [21] and NO_3^- [47]. The lack of a visible ground state resonance for any of the clusters may be explained by the repulsive Coulomb barrier being too thick to penetrate at the resonance energy of the ground state. However, this implies that the dianion ground state would have to lie at low energy even for the small system of OH where the electron-electron repulsion is bound to be significant. Yet not only the size of the system, but also the actual orbitals that come into play determine the energy level. In fact, dianionic states can have small negative binding energies even for small systems, an example being C_2^{2-} which lies above the monoanion by only 3.8 eV [11]. Furthermore, the ground state could decay into non-detectable fragments, that is, it decays through simple electron autodetachment leaving only the charged parent ion.

5.5 Conclusion

The cross sections for various reactions induced by electron impact on $OH^-(H_2O)_n$ for $n = 0$–4 were determined at the ASTRID storage ring. The threshold energies for detachment were found to be 4 eV for OH^- ranging to 11.5 eV for $OH^-(H_2O)_4$, reflecting the increase in electron binding energy upon hydration. The shape of the detachment cross sections was compared to a classical model cross section which to some extent reproduced the observed behavior.

Branching ratios for the different reaction channels were determined. In all cases where $n \geq 1$, the dominant channel was electron detachment plus total dissociation of the clusters into the constituent molecules of OH and H_2O, the branching ratios being ∼80%.

A resonance in the cross sections for $OH^-(H_2O)_3$ and for $OH^-(H_2O)_4$ was observed. In both cases, the resonance was found in the decay channel corresponding to the loss of a neutral water molecule while the rest of the system remained charged. The resonances were located at ∼15 eV and were ascribed to the formation of dianions in excited states.

CHAPTER 6

Electron attachment to $NO_2^-(H_2O)_n$ ($n = 0$–2)

6.1 Introduction

Though small dianions are unstable in the gas phase, they are important constituents in solids and in solutions. In these environments, stability is provided by polarization interactions with the surrounding molecules. To obtain a more detailed understanding of these interactions and how they affect the stability of small dianions, it is desirable to investigate particularly the transition from gas phase to solution phase. In practice, this can be accomplished by studying dianions embedded in small clusters of solvent molecules.

Wang and coworkers have studied how water molecules influence the electronic stability of dianions [124–126, 188]. For dianions in water clusters, they were able to measure the electron binding energy (EBE) as a function of the number of water molecules, adding waters one at a time. The photodetachment studies showed an increase in the EBE upon sequential hydration, and it was observed that the first few water molecules each increases the EBE by ∼0.5 eV. However, only binding energies of *stable* or *metastable* species with lifetimes in the order of µs could be determined in the experiments, implying that the dianion-water clusters had to be electronically stable or, at least, be nearly stable. In the case of $SO_4^{2-}(H_2O)_n$ and $C_2O_4^{2-}(H_2O)_n$, the smallest clusters that could be studied were limited to $n = 3$, as these were the smallest *bound state* dianions. Hence, it was not possible to deduce how water molecules affect the electron binding energy of *continuum state* dianions (see Fig. 6.1).

Here, the first evidence of environmental tuning of dianion resonance

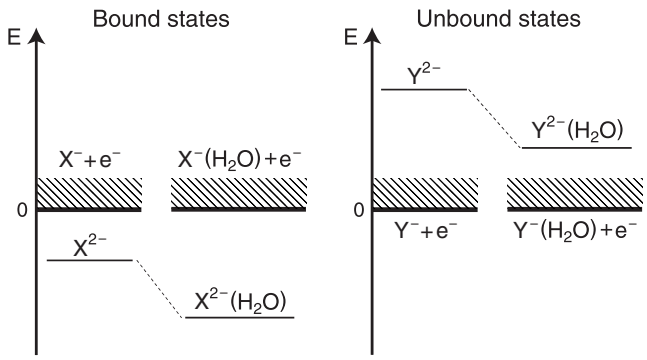

Figure 6.1: Solvation effect of bound and unbound states. The energy of the singly charged ion is chosen to be the zero point.

states in the continuum is presented. More specifically, the NO_2^{2-} dianion and NO_2^{2-} solvated by a few water molecules have been studied. The NO_2^{2-} dianion is known to have a lifetime of less than a microsecond [189] in aqueous solution. In the gas phase, however, NO_2^{2-} is found to be unstable by 7.2 eV with respect to loss of an electron with a lifetime of the order of femtoseconds [21], indicating a tremendous influence of water on the lifetime of the dianion. To elucidate the stabilizing effect at the single water molecule level, and the physical properties of NO_2^{2-} in water micro-solutions, the positive ground-state energies of NO_2^{2-}, $NO_2^{2-}(H_2O)$, and $NO_2^{2-}(H_2O)_2$ with respect to the respective monoanions have been measured in electron scattering experiments. Furthermore, the resonance states have been characterized by their decay channels.

6.2 Experiment

The present experimental work has mainly been conducted at the ELISA storage ring described in Sec. 3.4. The negative anions were formed in the cold cathode ion source to which a mixture of water vapor and N_2O gas was supplied. At low discharge currents, ion currents ranging from 100 nA for NO_2^- to 5 nA for $NO_2^-(H_2O)_2$ were obtained. After acceleration and mass-selection, the ions were injected into ELISA, where they were stored at an energy of 22 keV. The NO_2^- and $NO_2^-(H_2O)_{1,2}$ ions were stored in the ring for 0.5 seconds before the measurement started. The vibrational temperature of the ions is estimated to be room temperature after the 0.5 seconds of storage. After

this period, the ions were crossed with an electron beam of variable energy. The electron beam was chopped on and off at 10 Hz to distinguish between electron-induced and background signals from collisions with the residual gas in the ring. After the interaction region, neutral products mainly from electron-detachment reactions were detected by a multi-channel plate detector.

With the present experimental setup at the ELISA storage ring, no information about the products formed in the collision process can be obtained. However, such information is obtainable from experiments performed at the ASTRID storage ring where the high storage energy (MeV) allows for the use of energy-sensitive detectors. As branching ratios for the NO_2^- anion have already been published [21], only new experiments with $NO_2^-(H_2O)$ were carried out at ASTRID in order to determine the most important reaction channels and the decay pathway of the ground state dianion.

The signal from the solid state detector consisted of only four distinct peaks, as the masses of N, O, and H_2O are rather similar. Furthermore, the kinetic energy of single hydrogen atoms was so low (the beam energy was 1.919 MeV resulting in H kinetic energies in the order of 30 keV) that the peaks were buried in the electronic noise. Hence, within the resolution of the detector the anion resembles an anion X_4^- consisting of four equally heavy atoms X where X represents N, O, or H_2O. Furthermore, it might be possible to dissociate the water molecule upon electron impact in which case detection of an X entity could stem from detection of either O, $O + H$, $O + H_2$, $OH + H$, $O + H + H$, or $O + H + H$. On experimental grounds, it is therefore not possible to say whether the water molecule remains intact or dissociates during the collision.

6.3 Results

6.3.1 Cross sections

Figure 6.2(a) shows the cross section for formation of neutrals as a function of the electron energy for the three ions NO_2^-, $NO_2^-(H_2O)$, and $NO_2^-(H_2O)_2$ as obtained at the ELISA storage ring. For NO_2^- and $NO_2^-(H_2O)$, the non-resonant contribution to the cross section is found to follow the functional form of Eq. (2.6) with threshold energies of 9.0 ± 0.5 eV and 9.5 ± 0.5 eV, respectively as shown in Fig. 6.2(a).

In the case of NO_2^-, two structures are superimposed on the non-resonant background, which confirms the two dianionic states seen in the previous experiment with NO_2^- [21]. Furthermore, the resonance at low energy is evident for $NO_2^-(H_2O)$ and $NO_2^-(H_2O)_2$. A fit by Gaussian functions provides reso-

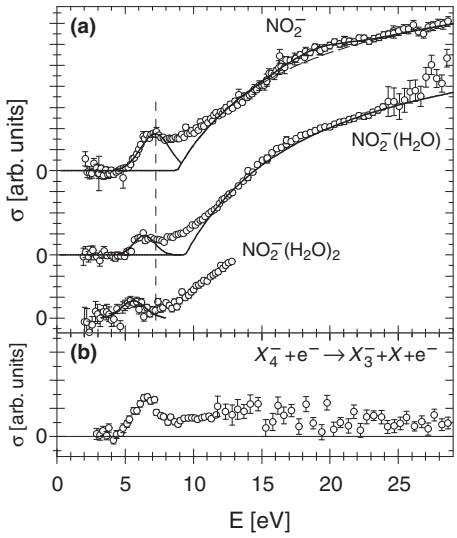

Figure 6.2: **(a)** The cross section for formation of neutrals as a function of the electron kinetic energy for NO_2^- (top), $NO_2^-(H_2O)$ (middle) and $NO_2^-(H_2O)_2$ (bottom) as obtained at the ELISA storage ring. The vertical line is the position of the dianion resonance for NO_2^-. Curves are drawn at the resonance positions to guide the eye. Further, the non-resonant contribution to the cross section according to Eq. (2.6) is drawn for NO_2^- and $NO_2^-(H_2O)$. **(b)** The cross section for production of an X fragment as the only neutral fragment as obtained at the ASTRID storage ring with $NO_2^-(H_2O)$. The cross section displays a clear low energy resonance.

nance energies of 7.2 ± 0.3 eV and 18.8 ± 0.4 eV for NO_2^- [1] and 6.4 ± 0.3 eV for $NO_2^-(H_2O)$. The signal to noise ratio is poorer for the $NO_2^-(H_2O)_2$ data, but the low energy resonance has clearly moved to an even lower value (5.6 ± 0.4 eV). Thus, the addition of single water molecules to NO_2^- increases the electron binding energy by 0.8 ± 0.3 eV per water for the ground-state dianion, i.e. the dianion becomes less electronically unbound upon hydration. The binding contribution per water molecule of the positive ground state is of the same order as observed for $SO_4^{2-}(H_2O)_n$ and $C_2O_4^{2-}(H_2O)_n$ bound-state dianions ($n \geq 3$) [124–126].

The width of the resonances is determined by three contributions: Franck-Condon factors, the experimental energy resolution and the natural width. These cannot easily be separated, and only a lower limit on the dianion life-

[1] This indicates that the previously found resonance energy of 16.5 eV was somewhat too low, as the present ELISA data agree well with the new ASTRID data on NO_2^-.

time can be given from the width, corresponding to roughly 0.5 fs (FWHM ~2 eV). As the dianions have decayed before reaching the end of the straight section, an upper bound on the lifetimes is estimated to be ~100 ns. For comparison, the lifetime of the NO_2 dianion is about a microsecond in bulk solution [189].

6.3.2 Branching ratios

The previous experiments with NO_2^- [21] revealed that the main contribution to the non-resonant background stems from pure detachment (production of neutral NO_2), which accounts for $75 \pm 15\%$ of the total events. Detachment in combination with loss of an N or O atom (i.e. production of $NO + O$ or $O_2 + N$) contributes $25 \pm 15\%$ as all channels with charged fragments were negligible [21]. In the case of NO_2^-, the dianion resonance was found in the channel corresponding to neutralization of the ion, indicating the following decay pathway:

$$NO_2^- + e^-(E = 7.2\text{ eV}) \rightarrow NO_2^{2-} \rightarrow \begin{cases} NO_2 + 2e^- & \Delta E = 2.27\text{ eV} \\ NO + O + 2e^- & \Delta E = 5.45\text{ eV} \\ N + O_2 + 2e^- & \Delta E = 6.83\text{ eV} \end{cases} . \tag{6.1}$$

Here, ΔE are the reaction energies calculated with the use of Ref. [160]. The possibility of total dissociation into $N + 2O + 2e^-$ is neglected as the energy threshold for this reaction is 12 eV. No information about the branching ratios of the different channels was reported.

For $NO_2^-(H_2O)$, the dominant reaction in the energy range between 10 eV and 45 eV is found to be detachment followed by dissociation into two fragments, X and X_3, respectively (see Sec. 6.2 for definition of X). This channel constitutes $50 \pm 7\%$ of the total events. The most likely bond to be broken is the hydrogen bond between the NO_2 and the water molecule, making it plausible that the main channel is detachment followed by dissociation into NO_2 and H_2O. The second most important channel corresponds to detachment followed by breakup into three fragments, i.e. the NO_2 molecule dissociates as well. The branching ratio for this reaction is $20 \pm 5\%$ in the energy range of 10 eV to 45 eV. All other channels contribute less than 10% each and together account for the remaining 30%.

Branching ratio measurements were also performed at the low energy resonance to identify the decay channels of the $NO_2^{2-}(H_2O)$. The most important decay channel was found to be the production of only one neutral fragment, being either N, O, OH, or H_2O, as the ASTRID experiment revealed a clear resonance in the cross section for this reaction (see Fig. 6.2(b)). Since the

anion-water bond is the weakest bond to break, this is interpreted as decay into $NO_2^- + H_2O + e^-$, which has a branching ratio of more than 50%. The resonance was further detected in the cross section for total neutralization, indicating that other channels also come into play. The measurements showed that the main neutral channels were $NO_2 + H_2O + 2e^-$ and $NO + O + H_2O + 2e^-$, as the channel $N + O_2 + H_2O + 2e^-$ is energetically forbidden at the resonance energy. However, some of these events stem from the non-resonant background and are thus not associated with the decay of the dianion.

6.4 Discussion

As shown above, the excess electron in $NO_2^{2-}(H_2O)_2$ is electronically unbound by 5.6 eV. For comparison, the transition into a true bound state dianion occurs at $n = 3$ for $SO_4^{2-}(H_2O)_n$ [125, 126], and an equal number of water molecules is required to make $C_2O_4^{2-}$ stable in the gas phase [124]. Whether this also holds for NO_2^{2-} is questionable. If each additional water molecule continues to stabilize the NO_2 dianion by the same amount as the two first waters (0.8 eV), at least ten water molecules are necessary to make the energy negative. Studies of $SO_4^{2-}(H_2O)_n$ and $C_2O_4^{2-}(H_2O)_n$ [124–126] show that the change in the electron binding energy when a water molecule is added decreases with the cluster size, n. Therefore, it is expected that many more than ten water molecules are needed to provide a stable dianion of $NO_2(H_2O)_n$. However, the character of the electronic structure of SO_4^{2-} and $C_2O_4^{2-}$ is different from that of NO_2^{2-}. The highest occupied molecular orbital is nonbonding for the former two but antibonding for NO_2^{2-}. As a result, the SO_4^{2-} and $C_2O_4^{2-}$ remain intact upon hydration, but this is not the case for NO_2^{2-}. In solution, the NO_2 dianion actually has a short lifetime of about 1 µs [189], and an electronically stable $NO_2^{2-}(H_2O)_n$ cluster for large n likely resembles an NO_2^- and a solvated electron, where the distance is maximized in order to lower the Coulomb repulsion. The repulsion is counterbalanced by the positive electron binding energy of a water cluster [190] rendering the $NO_2^-(H_2O)_n^-$ system electronically stable for large enough n.

The dianionic systems studied here may thus only be stable for larger ion-water clusters, but the interactions between ions and a few water molecules are still important to elucidate. In proteins, active sites are often shielded from water by surrounding amino acids, which leaves room for just a few water molecules in the vicinity of the site. Hence, only the role of single water molecules, and not the bulk solution, is relevant for the understanding of the behavior of the active site. The first few water molecules on NO_2^{2-} introduce a large change in the electron binding energy as also demonstrated for the

bound $SO_4^{2-}(H_2O)_n$ system [125], making the smaller clusters interesting.

6.5 Conclusion

It has been demonstrated that *unbound* electronic states of dianions are tuned in energy by the presence of a few water molecules. More specifically, the binding contribution of single water molecules to the NO_2 dianion has been directly measured. For the first two water molecules, the energy contribution is found to be 0.8 ± 0.3 eV for the ground state dianion. The dianion of NO_2 can decay by two-electron emission, possibly in combination with fragmentation. The $NO_2(H_2O)$ dianion mainly decays into $NO_2^- + H_2O + e^-$ with a branching ratio of more than 50%, whereas the channels, $NO_2 + H_2O + 2e^-$ and $NO + O + H_2O + 2e^-$, account for the remaining flux.

CHAPTER 7

Conclusion and outlook

The three investigations described in the preceding chapters focussed on different aspects of electron-anion collisions, and the results provide answers to some of the questions posed in Sec. 2.4.

Firstly, it was observed that the shape of the detachment cross section was well-described by a classical model cross section for most of the anions. However, for some of the systems, the measured cross section clearly exhibits a shape different from that of the model cross section. It was shown that this could possibly be explained by the detachment process being dependent on the relative orientation of the molecular anion with respect to the incoming electron.

Secondly, it was shown that the fragmentation pattern of cluster anions held together by hydrogen bonds is very different from that of covalently bound anions. Upon electron impact, dissociation is observed only to a minor extent for covalent anions, whereas the hydrogen-bonded cluster anions studied here dissociated into several fragments due to the much smaller dissociation energy.

Thirdly, it was observed that the properties of electronically unstable dianions are influenced by the presence of water. The addition of water molecules successively lowers the energy of the dianion state relative to the monoanion, thereby making the dianion less unstable.

Although some questions are now answered by the obtained results, new questions arise which could possibly be addressed in future studies of electron-anion collisions.

In the present thesis, a model for estimating the threshold energy for electron-induced detachment from monoanions has been presented. It was seen that the model gives a fairly good estimate of the threshold energy. However, in the case of PO_3^-, the measured threshold energy was significantly higher

than expected, and it was suggested that this might be an effect of the anion polarizability. It could be interesting to investigate in more detail what effect the polarizability might have on the threshold energy for detachment. In this respect, electron impact on two different types of anions of equal size could be compared. In one system, the excess electron is delocalized over the entire molecule, whereas in the other species the electron is localized. The delocalization might cause the threshold energy to be significantly higher than expected as the target electron is free to move around within the molecule, thereby possibly avoiding detachment. The two anions to be studied could possibly contain a carbon chain with suitable functional groups at each end. The comparison of the threshold energies for the two system could then be carried out for different lengths of the carbon chain. As the size increases, it could furthermore be imagined that for the system with the localized electron it becomes favorable to detach not the HOMO electron but an electron in the neutral end of the anion. As detachment of electrons in different states requires different threshold energies, such effects might be visible in the detachment cross section.

As mentioned above, it was shown that the attachment of water molecules changes the energy of the NO_2^{2-} transient state with respect to the corresponding monoanion. It would be interesting to repeat this type of experiment with another solute ion that exhibits a resonance state. The experiments rely on the detection of neutral fragments, and therefore the resonance energy of the naked dianion should not be too low, as decay of the transient state into at least one neutral fragment must be energetically possible. A good candidate for this study is NO_3^-, which exhibits a resonance state located at $\sim$18 eV above the ground state of the monoanion [47]. For this ion, it appears possible to trace the position of the resonance for larger numbers of attached water molecules than in the case of NO_2^-.

Another interesting experiment would be to investigate the influence of other solvent molecules than water on the stability of resonant dianion states. Solvent molecules with different dipole moments might result in different energy shifts upon solvation of the unstable states.

PART II
PHOTON-INDUCED FRAGMENTATION OF BIOMOLECULES

CHAPTER 8

Dissociation of photoexcited gas-phase chromophores

8.1 Introduction

The absorption of light by molecules is an extremely important process in nature. In photosynthesis, light is absorbed by, for instance, plants which convert the energy of the absorbed light into chemical energy, thereby allowing the plant to live. Light is also used by living organisms to sense the surrounding environment, a prominent example being the human vision.

In biological systems, the absorption of light is governed by *photoactive proteins*, and the particular molecular part of the protein responsible for the photoabsorption is called the *chromophore*. Upon absorption of light, the chromophore often undergoes structural changes, which in turn trigger the response of the whole protein. The initial chromophore response may be extremely fast (sub-picoseconds) when residing in the protein [191], but it is not known whether this is imposed by the protein or if it is an intrinsic property of the chromophore. Often, it is the assumption that the protein speeds up the initial process. However, without a detailed understanding of the intrinsic properties of the chromophore it is difficult to conclude how the presence of the protein may affect the chromophore photophysics. Therefore, it is crucial to study the isolated chromophore in order to elucidate what is happening in the protein. As an example, it is of importance to know the absorption spectrum of isolated chromophores in order to understand the perturbations that influence the absorption spectrum when surrounded by the protein [192].

Insight into the intrinsic response time of chromophores may be achieved by performing time-resolved pump-probe experiments in the gas phase. In

such experiments, the molecule is first excited by a short femtosecond light pulse, the pump pulse. To follow the temporal evolution of the excited molecule, a second pulse, the probe pulse, interacts with the species after a certain time delay. The effect of the probe pulse is monitored as a function of the time delay between the two pulses, and this allows elucidating the molecular dynamics going on upon photoexcitation. This technique was developed by Ahmed Zewail in the late 1980s, and it earned him the Nobel Prize for Chemistry in 1999.

In the present chapter, a new experimental setup is presented. It is the aim to use this setup to conduct pump-probe experiments on isolated chromophores. Here, preliminary results involving the delayed dissociation of photoexcited chromophore ions are reported, and these results represent the first steps on the way to time resolved pump-probe studies. In these preliminary experiments, chromophore ions are excited with only a single light pulse and the subsequent unimolecular dissociation of the ions into neutral fragments is studied.

The chromophore under investigation here is named retinal and is shown in Fig. 8.1. This chromophore is found in a protein called bacteriorhodopsin which governs the light-sensing function of certain bacteria. In the bacteriorhodopsin, the structure of the chromophore is the all-*trans* form as seen in the figure. The 11-*cis* form of the retinal chromophore serves as a photoreceptor in rhodopsin proteins. These proteins are present in the human eye and in the eyes of many other vertebrates where they are responsible for vision. This is actually the origin of the name 'retinal': the chromophore is present in the *retina* of the eye. In both proteins, the photoexcitation of the chromophore triggers an isomerization around the double bond between carbon number 11 and 12. This isomerization is the fastest photoreaction known in biology. Hence, knowledge of the intrinsic response time of the chromophore would be very interesting for the understanding of the role of the protein in this process.

In the present experiments, a model chromophore, which is not attached to the protein, is used (see Fig. 8.1). The structure of this chromophore is the all-*trans* form from bacteriorhodopsion and the link to the protein is replaced by a butyl group ($-CH_2CH_2CH_2CH_3$). The model chromophore is protonated at the nitrogen atom and is hence positively charged. This is also found to be the case in the protein and the model system studied here is therefore the biologically relevant species.

8.2 Decay of excited states

To understand the observations made in the experiments presented in the following, knowledge is required about different decay processes of excited

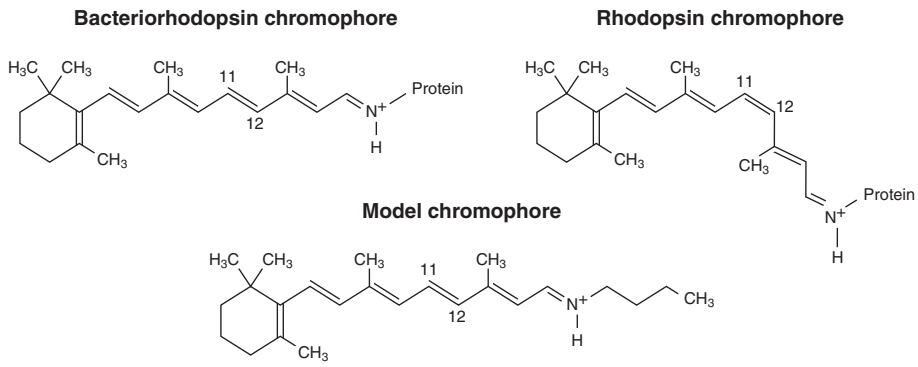

Figure 8.1: Structure of the all-*trans* retinal chromophore in bacteriorhodopsin, the 11-*cis* retinal chromophore in rhodopsin, and the all-*trans* *n*-butyl model retinal chromophore used here.

states of molecules with many degrees of freedom. The present section therefore serves as a brief introduction to the photophysical processes occurring upon photoexcitation. A more elaborate discussion on the topic may be found in Refs [193, 194].

Organic molecules are most commonly closed-shell species, i.e. they possess an even number of electrons, and therefore emphasis is put on such systems in the remainder of this section. In their ground state, all electrons are paired, which yields a total spin of $S = 0$. The ground state is thus a singlet state and is denoted S_0. Upon excitation of one electron, two possibilities for the total spin, S, exist: either the two unpaired electrons can couple to a total spin of $S = 1$ or $S = 0$. Generally, the triplet (i.e. $S = 1$) state has the lowest energy. This is attributed to the fact that electron motion is more correlated in a triplet state, which leads to a reduction in Coulomb repulsion for the triplet as compared to the singlet state. The excited singlet states are labelled S_n for the nth excited singlet state above S_0 and similarly for the excited triplet states, T_n. Note that the '0' subscript is reserved for the ground state (see Fig. 8.2).

To first order, spin is a conserved quantum number in molecular transitions, and as a consequence absorption of light preferentially excites the molecule from the singlet ground state to an excited singlet state. After the initial photoexcitation, several processes are competing, and these processes are schematically illustrated in Fig. 8.2. Some of the electronic energy may be converted into vibrational energy via a radiationless transition to a lower-lying singlet state, a process known as *internal conversion* (IC). It is also possible that a radiationless transition brings the system to a lower-lying triplet state

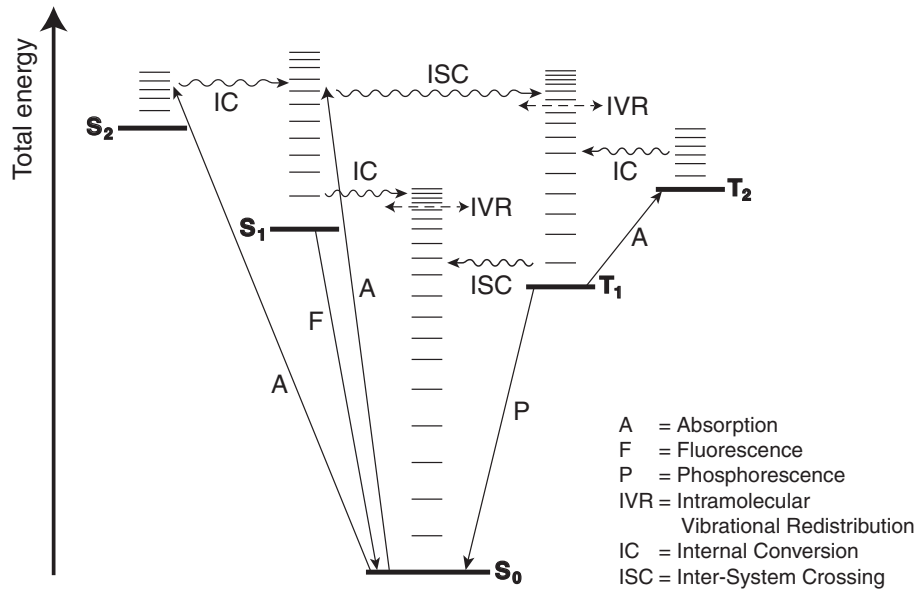

Figure 8.2: Schematic illustration of the various photophysical processes. Absorption and emission processes are indicated with straight arrows, whereas the horizontal arrows indicate radiationless processes. The wavy arrows represent transitions between different electronic states which convert electronic energy into vibrational energy. The dashed arrows signify redistribution of vibrational energy in which process the total vibrational energy is unchanged.

in which case the process is called *intersystem crossing* (ISC). The rate constant for internal conversion is dependent on the geometry of the potential energy surfaces involved in the transition and on the electronic couplings. The rate constant for the $S_1 \rightarrow S_0$ internal conversion may be of order 10^5–10^8 s^{-1}. However, if the two potential energy surfaces undergo a crossing or touch at one point (conical intersection), the time scale may be much faster (sub-picoseconds). The rate for intersystem crossings depends on the spin-orbit coupling. It is typically of order 10^6–10^9 s^{-1} for the $S_1 \rightarrow T_1$ transition in molecules without atoms heavier than oxygen, whereas it is of order 10^{-1}–10^4 s^{-1} for the $T_1 \rightarrow S_0$ intersystem crossing [193, 194].

Before these processes occur, *intramolecular vibrational redistribution* (IVR) normally takes place. In this process, the vibrational energy is distributed among the vibrational modes, which usually results in a statistical population of the $3N - 6$ modes, where N is the number of atoms in the molecule. As the energy is merely redistributed, the total vibrational energy is conserved in the

process.

As regards higher-lying excited states, S_n and T_n ($n \geq 2$), internal conversion to the lowest excited states, that is the $S_n \rightarrow S_{n-1} \rightarrow \cdots \rightarrow S_1$ and $T_n \rightarrow T_{n-1} \rightarrow \cdots \rightarrow T_1$ transitions, is very rapid (picoseconds). Therefore, relaxation back to the ground state through emission of light normally only occurs from the S_1 (this is called *Kasha's rule* [193, 194]) and T_1 states as the time scale for these processes is much lower. The spin-allowed radiative transition from S_1 to S_0 is referred to as *fluorescence* and has a rate constant of 10^6–10^9 s^{-1}. The spin-forbidden radiative transition $T_1 \rightarrow S_0$ is known as *phosphorescence*. The forbidden character of this transition is revealed in the rate constant for the process, which is of order 10^{-1}–10^4 s^{-1} [193, 194].

In the case where radiative transitions are slow compared to the radiationless transitions, decay back to the ground state occurs preferentially through radiationless transitions. Accordingly, all the energy of the absorbed light is put into vibrational excitation of the molecule. If the molecule is in a solution, it can dissipate the excess vibrational energy to the surrounding solvent molecules and thereby stay intact (*vibrational relaxation*). In the gas phase, however, things are quite different. Here, vibrational relaxation relies on infrared emission which is usually slow (milliseconds). Another option is fragmentation of the molecule. Through IVR, the excess vibrational energy is constantly being redistributed in the molecule. There is then a finite probability that certain vibrational modes may gain sufficient energy to be excited into the continuum, thereby causing fragmentation of the molecule. This process is known as *statistical dissociation*. The timescale for such a decay is dependent on the amount of energy deposited in the molecule and the size of the molecule. Hence, if more energy is deposited into the molecule, fragmentation will occur faster, as more energy is available for redistribution. For a given energy deposit, fragmentation of a large molecule happens slower than fragmentation of a small molecule, as the energy is distributed over more modes in the former case, thereby lowering the probability to cause sufficient excitation of one single mode.

If a photoexcited ion were to de-excite by fluorescence or phosphorescence, it would probably not dissociate once it was back in the electronic ground state. In the emission process, the molecule gets rid of some of the absorbed energy implying that much less energy is available for statistical dissociation following IVR. In the present experiment, only neutral fragments are detected meaning that photoexcitation events leading to light emission are probably not observable since, most likely, no neutral fragments are produced as argued.

8.3 Experimental setup

The experimental setup consists of three basic parts: the ion source for production of the chromophore ions, a single-pass beam line for ion transport and neutral detection, and a laser setup. Here, each of the three parts is introduced followed by a description of the data acquisition system.

8.3.1 The electrospray ion source

To bring biomolecules to the gas phase requires the use of so-called "soft" ionization techniques. Conventional ion sources, like those described in Chap. 3, make use of "hard" ionization techniques where ions are formed in harsh environments, often in the presence of a hot filament emitting electrons. Under these circumstances, the often fragile larger molecules dissociate, thereby making such sources unsuitable for production of gas-phase biomolecular ions.

In the 1980s, a new type of ion source, named the electrospray ion source, was developed by John Fenn [195] who was awarded the Nobel Prize for Chemistry in 2002 for his invention. This type of ion source is now widely used in many areas of physics and chemistry where gas-phase biomolecules are being studied.

A schematic drawing of the electrospray ion source used in the present experiments is seen in Fig. 8.3. First, a solution containing the biomolecules of interest is made. A small amount of a solid powder containing the biomolecules is dissolved in typically either methanol or a one-to-one mixture of water and methanol. As opposed to the ion sources for production of small molecular ions, where charging is obtained by removing or attaching electrons, the solute molecules are charged by adding or removing a proton, i.e. by protonation or deprotonation. Often, the charge state of the solute molecules is controlled by adding acetic acid or ammonia to produce the protonated or deprotonated ions, respectively.

Next, a syringe is filled with the solution, and the syringe is then placed in a syringe pump. The pump ensures a constant flow rate of the solution from the syringe through a fused silica capillary to the spray needle. The spray needle is usually kept on a potential of several kilovolts with respect to a heated capillary, which defines the entrance to the remainder of the source.

The strong electric field at the needle tip charges the emerging liquid, and due to the Coulomb repulsion the liquid is dispersed into a fine spray of charged droplets. Upon entering the heated capillary, solvent molecules begin to evaporate thereby decreasing the size of the droplets. Having reached a certain size (the Rayleigh limit), the Coulomb repulsion between the droplet surface charges exceeds the forces of the surface tension, and the droplet is

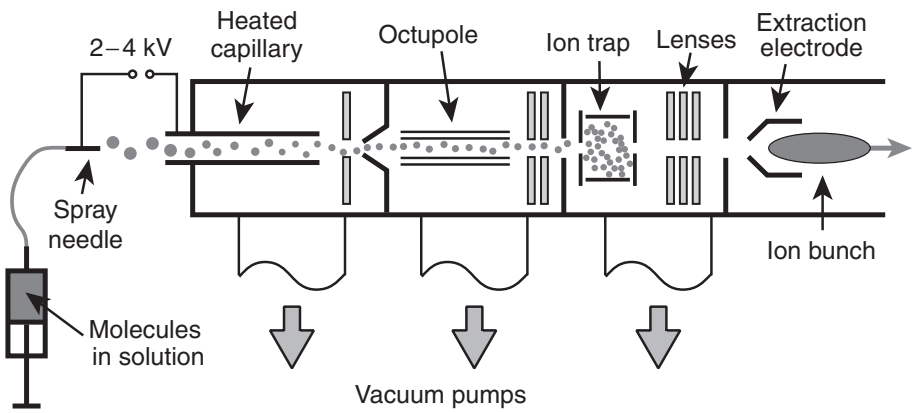

Figure 8.3: Schematic drawing of the electrospray ion source.

torn apart into smaller droplets. This process continues until the droplet size is small enough to allow for desorption of the ions into the ambient gas [195].

Following the heated capillary are lenses for focusing purposes and an octupole beam guide that steers the ions into a Paul trap consisting of a cylindrical ring electrode and two end caps [196]. In trapping mode, a radio-frequency (RF) potential is applied to the cylindrical electrode while the end caps are at static potential. Helium buffer gas is let into to the trap to dissipate the initial energy of the ions as they enter the trap. After some accumulation time, an ion bunch is extracted from the trap by turning off the RF and biasing the entrance and cylinder electrodes in such a way as to expel the ions from the trap. A typical number of ions in one bunch is of order 10^3–10^4 for an accumulation time of 100 ms. The bunch is then focused and extracted from the source.

8.3.2 The single-pass ion beam apparatus

Figure 8.4 illustrates the setup of the single-pass ion beam apparatus. During extraction from the ion source, the ions are accelerated to an energy of 20 keV and focused before they enter a 90° bending magnet. The bending magnet serves to select ions of a given mass-to-charge ratio, and only these continue further downstream. Here, they pass deflection plates and quadrupoles used to steer and focus the beam. In addition, this section of the beam line also serves as a differential pumping stage to connect the high vacuum region ($\sim 10^{-6}$ mbar) directly after the ion source with the ultra high vacuum region ($\sim 10^{-9}$ mbar) in the laser interaction region. Before entering an electron spectrometer surrounding the interaction region, the ion beam is deflected 3° by a

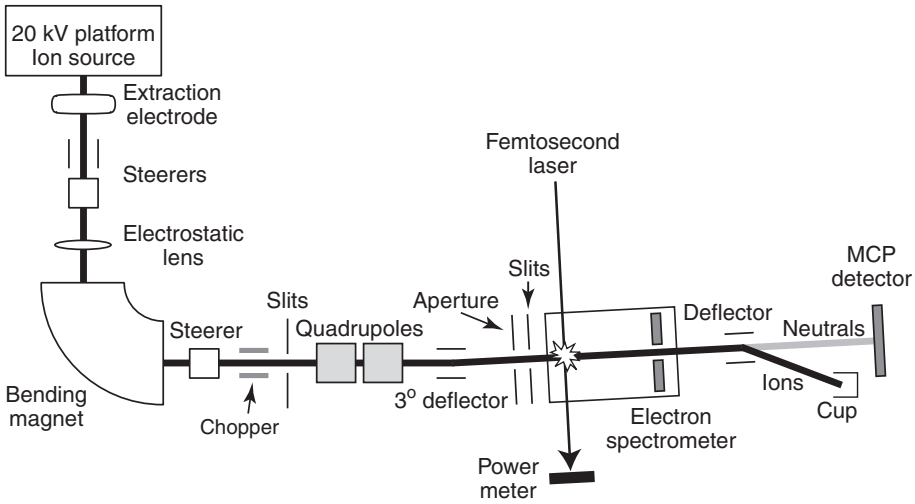

Figure 8.4: Schematic drawing of the single-pass ion beam apparatus.

set of electrostatic plates. This is done to remove neutrals formed in the preceding section by collisions with the residual gas, as these fragments would give rise to a significant background count rate. Moreover, a set of horizontal and vertical slits just before the spectrometer entrance allows removing neutrals as well as collimating the ion beam.

The electron spectrometer consists of a stack of 25 equidistant circular electrodes with increasing aperture diameter. The electrodes are interconnected through identical resistors, and the last electrode is grounded while the first one can be biased. When biased, the electrode configuration produces a homogenous electric field parallel to the ion beam direction. These electrodes were made for guiding photoelectrons onto a MultiChannel Plate (MCP) detector at the end of the spectrometer, hence the name 'electron spectrometer'. Both the detector and the connecting phosphor screen have a central hole in order to allow the ions and neutrals to pass. However, in the experiments presented here, this detector was not used. In the first part of the spectrometer, the ion beam is crossed at right angles with a laser beam, details of which are postponed to the next section.

The spectrometer is followed by a set of horizontal deflection plates, which deflects the ion beam into a Faraday cup. As the ion current is too low to be measured, the cup only serves as a beam dump. Neutrals pass unaffected through the deflection plates and impinge on a second MCP detector coupled to a phosphor screen located at the end of the beam line. The impinging neu-

trals give rise to a burst of electrons, which is amplified through the MCP detector, and in turn the electrons create a bright spot on the phosphor screen. To register the arrival of neutral fragments, the signal from the MCP may have been used, but this signal turned out to be too noisy. Instead, the light emitted from the phosphor screen is detected by a PhotoMultiplier Tube (PMT) which provides the final electronic signal used for neutral fragment detection.

8.3.3 The laser system

The femtosecond laser system consists of a modelocked Ti:Sapphire oscillator (NJA-5, Clark-MXR) which is pumped by a diode laser (Millenia, Spectra-Physics). To boost the output power of the Ti:Sapphire laser, the laser pulses are first stretched in time to reduce the peak intensity in order to avoid damage of optical elements in the amplifier, and to reduce nonlinear effects. Then the stretched pulses are sent into a regenerative amplifier, which is pumped by an Nd:YAG laser (ORC-1000, Clark-MXR). After several roundtrips in the amplifier, maximum power is reached, and at this time, the light is coupled out of the cavity by a Pockel cell. Subsequently, the light pulses are compressed in the time domain, and the final result are pulses with a time duration of $\sim$110 fs and a pulse energy of 0.8 mJ at a repetition rate of 1 kHz. The mean wave length is 820 nm and the spectral width is $\sim$15 nm (FWHM).

However, for the retinal chromophore studied here the lowest electronic excitation, that is the $S_0 \rightarrow S_1$ transition, is at 610 nm [197], and hence the 820 nm photons cannot excite the chromophore electronically. Meanwhile, the $S_0 \rightarrow S_2$ absorption band has a maximum around 390 nm [197] close to the second harmonic of the 820 nm. Therefore, the light is sent through a non-linear BBO (β-barium borate) crystal in which 410 nm light is produced by second harmonic generation. The conversion efficiency is 25%, yielding an average power of 200 mW at 1 kHz (0.2 mJ per pulse). Dispersion in the crystal increases the time duration of the light pulses to 150 fs [198].

After the nonlinear crystal, the 820 nm and 410 nm light are co-propagating, and the two colors are subsequently separated by means of a dichroic mirror coated for high reflectivity at 410 nm and high transmission at 820 nm. The 820 nm light is dumped in a beam dump while the 410 nm pulses are sent through the interaction region on the other side of which the light hits a power meter. Here, the measured power is 160 mW as losses are introduced by two mirrors before the interaction region, and, most significantly, by going through the windows in the vacuum chamber.

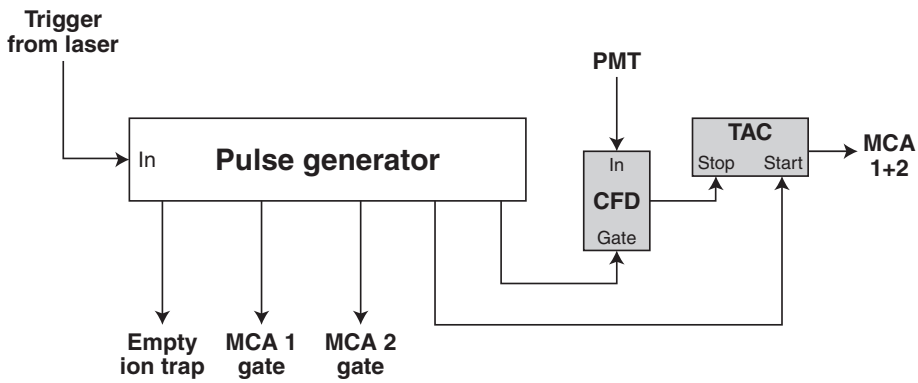

Figure 8.5: Schematic drawing of the timing and data acquisition system.

8.3.4 Data acquisition

A schematic drawing of the timing setup and the data acquisition system is shown in Fig. 8.5. Prior to the laser shot, a pulse generator receives a trigger signal from the laser. The ions are then extracted from the ion trap after a given time delay such that timely overlap between the ions and the laser pulse at the interaction point is ensured. Shortly before neutral fragments stemming from photoexcited ions are expected to arrive at the MCP, a pulse from the generator is transmitted to a Time-to-Amplitude Converter (TAC). The function of the TAC module is to produce a signal with an amplitude proportional to the elapsed time between two input pulses, and the generator pulse is the first one of these pulses. Soon after the TAC is started, the generator sends a gate signal to a Constant Fraction Discriminator (CFD) to which the output of the PhotoMultiplier Tube (PMT) is connected. Accordingly, the CFD is only active in the short time span when the laser-induced neutral fragments are anticipated to arrive at the MCP. When a neutral fragment is detected, the CFD sends a standard signal to the TAC to stop it. The TAC signal is then transmitted to a MultiChannel Analyzer card (MCA) which records the TAC pulse height distribution. Assuming that only one neutral fragment per ion bunch hits the detector within the active time of the CFD, the recorded pulse height spectrum directly yields the distribution of the time-of-flight (TOF) of the neutral fragments from the interaction region to the MCP.

However, not only neutrals created by ions interacting with the laser light contribute to the TOF spectrum, but also neutrals produced in collisions with residual gas are detected. To extract the TOF distribution of events that are due to interactions with the laser light, subtraction of the background events

must be enabled. Conceptually, this can be done by blocking the laser beam of every second ion bunch and then record the TOF spectrum with laser light on one MCA card and the background TOF spectrum on another.

In practice, the timing system runs in such a way that every laser trigger signal causes the system to perform two of the cycles described above. According to this timing scheme, only ion bunches from every second emptying of the trap are overlapped with the laser pulses. The TAC signal is then sent to two MCA cards, and in addition the pulse generator creates two gate pulses, one for each of the two MCA cards. The gate pulses ensure that one card only records the TAC signal from ion bunches that have interacted with the laser pulses, while the other card registers the remaining TAC signals. The TOF distribution for the laser-induced neutral fragments can now be extracted by subtracting the two recorded TOF distributions from one another.

8.4 Results and discussion

The distribution of flight times is shown in Fig. 8.6 where time zero is defined by the arrival of the laser pulse at the interaction region. As is evident, the TOF distribution of background events is smooth and without structures, but when the ions are crossed by the laser pulse, a pronounced peak is superimposed on the background signal. Subtracting the two distributions yields the TOF distribution for the laser-induced neutrals, and this spectrum is shown in same figure in the graph to the right.

At a first glance, it might be expected that the width of the laser-induced signal would be very small, as the ions are interacting with a short pulse of a duration of only 150 fs implying that the interaction time is very well-defined. Nonetheless, the finite extent of the interaction region, estimated from the laser spot size to be a few millimeters, induces a spread in the flight time to the MCP. Moreover, fluctuations in the acceleration voltage cause a spread of ion energies resulting in an additional spread in the flight time. To elucidate whether these two effects can account for the width of the observed signal, Monte Carlo simulations were performed. Using reasonable values for the voltage fluctuations, the spatial extent of the interaction region and the known geometry of the experimental setup (the distance from the interaction region to the detector etc.), a simulated TOF distribution as represented by the red dotted curve in Fig. 8.6 is obtained. It is clearly seen that the two effects alone cannot explain the width of the observed peak.

However, another contribution to the peak width turns out to be significant. The retinal chromophore ions are cations implying that the laser-induced neutral fragments can only stem from dissociation of the ions. In the dissociation process, the emerging fragments must carry some kinetic energy in the

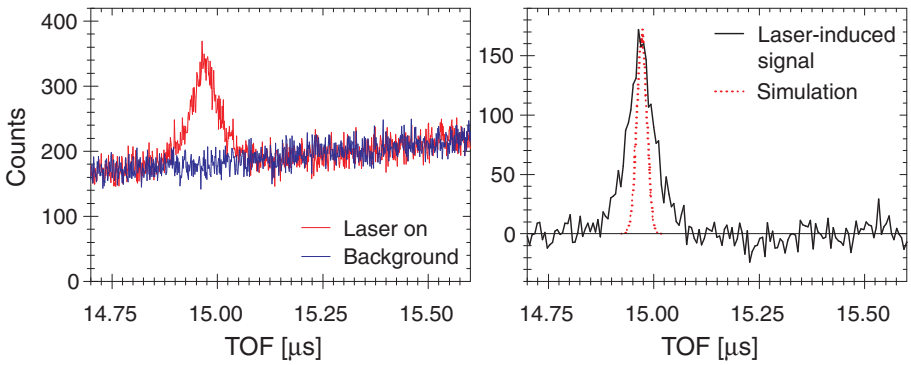

Figure 8.6: **Left:** Time-of-flight spectra recorded with laser (red curve) and without laser (blue curve). A pronounced peak is visible when the laser is on. **Right:** Laser-induced signal (black curve) together with a simulation (dotted curve) taking into account only the energy spread of the ions and the finite extent of the interaction region.

rest frame of the ion — otherwise dissociation is not achieved. Furthermore, the momentum gained by the neutral fragment has a random direction, and in the lab frame this effect adds to the energy spread of the neutral fragments. By comparison to the simulations presented above, it is concluded that the kinetic energy release in the dissociation process determines the width of the observed peak.

From the time-of-flight spectra in Fig. 8.6, not much information on the dissociation processes, like the characteristic decay time of the photoexcited ions, can be obtained. Meanwhile, it turns out that such information can actually be extracted if the electron spectrometer is employed. Figure 8.7 shows the TOF distributions with and without laser when a voltage of +3 keV is applied to the first electrode in the spectrometer. Again, the TOF distribution of background events is smooth and structure-less, but when the ions are crossed with the laser, two pronounced peaks appear in the TOF spectrum. When subtracting the background TOF distribution, it is clearly seen that there is also a signal in the region between the two peaks. The strange shape of the laser-induced TOF spectrum has a quite simple explanation as described in the following.

Figure 8.8 illustrates the effect of the spectrometer voltage on the TOF distribution. Being positively charged, the retinal ions are decelerated by the positive voltage applied to the first electrode in the spectrometer, implying that the ion kinetic energy is reduced to 17 keV at the spectrometer entrance. On their way through the spectrometer, the ions are slowly accelerated by the homogenous electric field until at the spectrometer exit they regain their initial

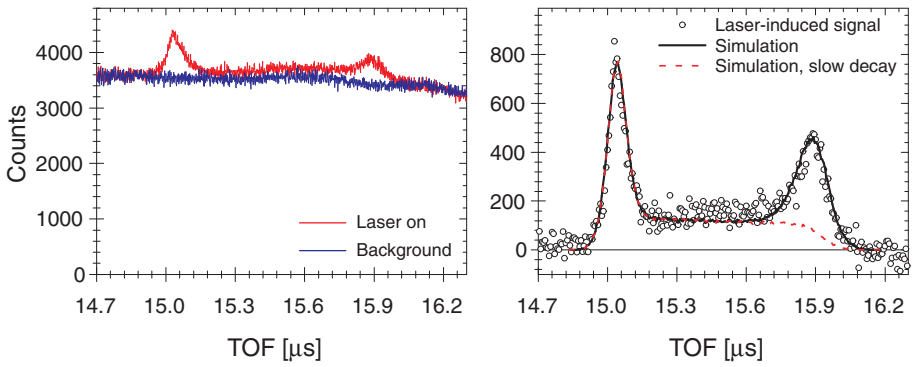

Figure 8.7: **Left:** Time-of-flight spectra recorded with and without laser with a voltage of +3 keV on the spectrometer. Two peaks are visible when the laser is on. **Right:** Laser-induced signal (open circles) together with simulations including only slow dissociation (red dashed curve) and both slow and fast decay (black curve).

kinetic energy (see Fig. 8.8). The neutral fragments created in the spectrometer retain the velocity of the parent ion at the time of dissociation, as they are unaffected by the electric fields. Thus, the electric field in the spectrometer causes a modulation of the velocity of the neutral fragments, and this modulation is reflected in the TOF distribution.

To explain the origin of the two peaks, it must first be noted that the ions giving rise to neutrals impinging on the detector are those which have decayed before reaching the deflector after the spectrometer (see Fig. 8.4). The flight time from the interaction region to this deflector is 3.5 µs at an energy of 20 keV, and hence only ions decaying within the first 3.5 µs after photoexcitation contribute to the measured TOF distribution.

Neglecting the energy spread, all ions that decay between the end of the spectrometer and the deflector have the same velocity, and consequently the corresponding neutral fragments all impinge on the MCP at the same time. The result is a large peak in the TOF distribution, and this explains the origin of the peak observed at early flight times.

In contrast, the neutrals created inside the spectrometer have different velocities dependent on at which point the parent ion dissociated. As the ions move slower in this region, the neutral fragments produced in the spectrometer have longer flight times to the detector than the ones produced outside. Hence, the former fragments arrive at the MCP at later times. The part of the TOF distribution that lies outside the peak at early flight times is therefore due to ions dissociating in the spectrometer. Since the ions spend 2 µs in

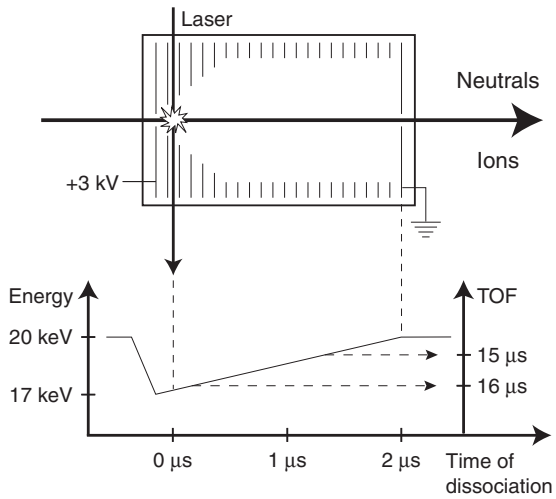

Figure 8.8: Illustration of how the homogenous electric field in the spectrometer influences the time-of-flight spectrum.

the spectrometer, this part of the TOF distribution stems from ions decaying within the first 2 µs after photoexcitation. The observation of a second peak at late flight times then indicates that a significant fraction of the ions dissociates quite rapidly after photoexcitation, i.e. early in the spectrometer where the ion velocity is low.

The decay of the present model chromophore after excitation by 400 nm photons was studied at the ELISA storage ring on the millisecond timescale [197]. In those experiments, the time resolution was limited to ∼75 µs, and consequently only decays with a much longer lifetime than this time resolution could be investigated. It was found that after irradiation by 400 nm photons the ions decayed on the millisecond timescale through statistical dissociation.

This piece of information may be used to simulate the TOF distribution observed in the present experiment. As previously mentioned, only ions decaying within the first 3.5 µs after photoexcitation contribute to the observed TOF signal. This timescale is three orders of magnitude smaller than the timescale for the slow statistical dissociation observed in the experiments mentioned above. In the present experiment, it can therefore, to a good approximation, be assumed that the ions undergo this slow dissociation with constant probability. By use of this assumption, the time-of-flight distribution for neutrals stemming from this slow decay can be modelled by performing Monte Carlo

simulations. The result of such a simulation for the slow decay is shown as the red dashed curve in Fig. 8.7. In addition to fluctuations in the acceleration voltage and the finite extent of the interaction region, the simulations furthermore include the effect of kinetic energy release in the breakup. The energy release is chosen so that the width of the simulated peak matches that of the experimentally observed one. Clearly, the peak at late flight times cannot be explained by the slow decay as also suggested earlier. If, in addition, an exponential decay with a lifetime of 100 ns is included in the simulations (black curve in Fig. 8.7), the simulation is able to reproduce the experimental findings to a satisfactory extent. Thus, it is concluded that photoexcitation of the ions leads to at least two different decay processes taking place on significantly different timescales: the lifetime of ions decaying via the slow statistical decay is on the millisecond timescale, whereas the lifetime of ions decaying by the faster process is of order 100 ns.

From the simulations, the fraction of photoexcited ions that decay via the slow statistical process can be estimated. As already mentioned, the entire decay curve for the slow decay was measured in another experiment [197]. Using these results it is estimated that of all ions decaying via this process only 0.8% are actually observed in the present experiment. Furthermore, it is found that 30% of the observed signal stems from the fast decay. As just a small fraction of the slowly decaying ions is in fact observed here, this implies that of all photoexcited ions merely 0.3% decay via the fast process.

8.5 Current status

The results presented in the previous section have all been obtained with the participation of the author of the thesis. However, during the writing of the present thesis, a few interesting discoveries have been made, but as the author has not been directly involved with the experiment in the writing phase, these discoveries are merely outlined in the following.

Firstly, it has been observed that the ion intensity within an ion bunch is modulated in time as shown in Fig. 8.9. This effect is caused by the RF potential keeping the ions trapped in the ion trap. During the emptying of the trap, this potential cannot be switched off instantaneously, and this causes the ions to 'splash out' in small bunches. If the phase of the RF potential at the time of extraction of ions from the trap is always the same, the microbunched structure of the ion bunch can actually be exploited. Provided that the RF phase is locked at extraction, it is possible to overlap the laser and the ions at the moment in time where the ion density in the interaction region reaches its maximum. As compared to the situation where the RF phase is random, the phase locking provides data with better statistics for the same recording

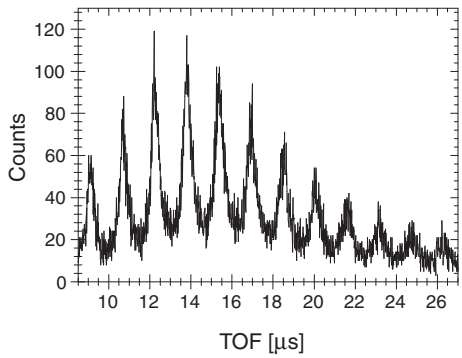

Figure 8.9: Time-of-flight distribution for the background events when the RF phase at extraction of the ions from the trap has been locked. The microbunching of the ion bunch is clearly seen.

time. Thus, the data acquisition becomes more efficient when the RF phase is locked, which it has been in the more recent measurements.

Secondly, only a small part of the ion bunch is in fact overlapped with the laser. In Fig. 8.9, it is seen that the time duration of one microbunch is ∼1.5 µs corresponding to a geometrical length of 20 cm. Since the ions do not have time to move during the interaction with the femtosecond light pulse, merely ions within the laser spot of a few millimeters in size interact with the laser light. As a consequence, only a small number of ions within one microbunch actually meet the laser light, and all remaining ions merely contribute to the background events. Using the chopper plates in the beam line (see Fig. 8.4), only a minor fraction of the ion bunch is now allowed to enter the interaction region, thereby reducing the background counts significantly. Moreover, since a very small number of neutrals are created by collisions with the residual gas in the spectrometer, neutrals from the fast decays arrive at the detector almost free of background events. Therefore, the signal-to-background ratio at late flight times is now improved drastically.

The two improvements have made it possible to obtain good-quality data on the dependence of the TOF distribution on the laser power. These measurements confirmed that the slow decay stems from ions having absorbed one photon as was anticipated from the previously published results [197]. However, the number of ions decaying through the fast decay varied as the square of the laser power. Thus, it was concluded that the fast decay is not due to another decay mechanism but rather to the absorption of two photons. In the latter case, much more energy is available for vibrational excitation, and as a consequence, the probability to excite one mode to the continuum increases,

thereby leading to a much shorter lifetime.

8.6 Conclusion

An experimental setup, which combines a single-pass ion beam apparatus with an electrospray ion source, has been presented. The long-term goal is to use the setup to do pump-probe studies of the fast response of large gas phase biomolecules to the absorption of light. Here, the first results obtained with the new setup were reported.

The unimolecular dissociation of the positively charged all-*trans* *n*-butyl retinal chromophore upon photoexcitation at 410 nm was studied. The setup allowed to investigate the decay of ions within the first 3.5 µs after photoexcitation. Furthermore, the decay curve could be mapped out for the first 2 µs of the decay, thereby making it possible to observe prompt decay of ions.

It was shown that at least two different dissociative processes were activated after photoexcitation of the chromophore cations. The timescales of the two dissociative processes were significantly different. The lifetime of ions decaying via the slow decay process was determined in another experiment to be of order milliseconds. In the present experiment, it was established that the lifetime of the fast decay was of order 100 ns. Through a measurement of the dependence of the two processes on the laser power, it was found that the slow decay was caused by the absorption of one photon, while ions decaying via the fast decay process had absorbed two photons. This implies that both decays are likely to be statistical, and accordingly no evidence for any non-statistical process is found. Furthermore, Monte Carlo simulations were performed. These were found to be in good agreement with the experimental observations, thereby bringing confidence to the interpretation of the results.

8.7 Outlook

It has now been demonstrated that with the new experimental setup it is possible to detect neutral fragments stemming from dissociation of photoexcited biomolecules with good signal-to-background ratio.

The next step is to build the laser-setup needed to do one-color pump-probe experiments. This involves splitting up the laser beam in two beams and setting up a delay stage in one of the beam paths before merging the two beams again. The TOF distribution is then monitored while the delay between the two pulses is changed.

For the pump-probe experiment to work, the ions must absorb a photon from each of the pulses implying that the process to be studied is a two-photon

process. Even though the probability for two-photon absorption is low, the results presented in this chapter bring hope that pump-probe studies are indeed feasible. Here, only a very small fraction of ions absorbed two photons, but still the two-photon signal was clearly visible as merely a small fraction of the one-photon signal is observable with the present experimental setup. Moreover, the two-photon signal could even be separated in time from both the one-photon signal and the main part of the background events, whereby a very good signal-to-background ratio is obtained for this signal.

In relation to the response process of the retinal chromophore taking place inside proteins, it would be more appropriate to follow the dynamics upon excitation of the chromophore to the S_1 potential energy surface rather than exciting the chromophore to the S_2 state. However, the $S_0 \rightarrow S_1$ absorption band is in the 600 nm region [197], and at the moment, the laser wavelength can only be chosen among the fundamental 820 nm wavelength and the second and third harmonic of the Ti:Sapphire laser at 410 nm and 270 nm, respectively. To provide femtosecond light-pulses of tunable wavelength, an Optical Parametric Oscillator (OPO) will be in used in the future. With the OPO at hand, it should be possible to study the dynamics following excitation to the S_1, whereby hopefully the main goal of measuring the intrinsic response time of the chromophore in vacuum could be reached.

CHAPTER 9

Summary

In the present thesis, electron-induced fragmentation of several gas-phase negative ions was studied. In addition, the results from an investigation of the delayed dissociation of a photoexcited biomolecular positive ion were presented.

Electron impact on PO_n^- ($n = 0$–3), $OH^-(H_2O)_n$ ($n = 0$–4), and $NO_2^-(H_2O)_n$ ($n = 0$–2) was studied for incident-electron energies in the range from 0 eV to 50 eV. In all cases, the cross section for electron detachment exhibits a well-defined onset at a threshold energy, which is significantly higher than the binding energy of the excess electron. This was attributed to the fact that the incoming electron has to overcome the Coulomb repulsion of the negative ion before detachment is possible. In most cases, the overall shape of the detachment cross section is represented fairly well by a classical model cross section. For some molecular ions, however, significant deviations occur. It was suggested that the deviations appeared because the detachment process was dependent on the relative orientation of the ion with respect to the incoming electron.

For PO_n^-, the dominant reaction channel is pure detachment, that is the excess electron is released upon electron impact. At higher energies, electron impact furthermore results in dissociative detachment where an P–O bond is broken. Three- and four-body fragmentation is found to be negligible, as the molecules are strongly bound.

In contrast, the dominant reaction channel for $OH^-(H_2O)_n$ is observed to be detachment combined with the fragmentation into $n + 1$ oxygen-containing fragments. This significant difference occurs since the hydroxide-water clusters are bound by hydrogen bonds. These bonds are much weaker than the covalent bonds of PO_n^-, and hence total fragmentation requires only little energy.

Upon bombardment by electrons, several of the ions are capable of form-

ing transient states of doubly charged negative ions. For $OH^-(H_2O)_3$ and $OH^-(H_2O)_4$, such a transient state is formed if the incoming electron has an energy of ~15 eV. For $NO_2^-(H_2O)_n$, the energy of the transient state decreases with the number of water molecules. This implies that the water molecules are able to make the transient state less unstable against spontaneous emission of electrons.

Finally, results on dissociation of a retinal model chromophore following photoexcitation were presented. It was shown that at least two different decays are in play when the chromophore is electronically excited by 410 nm photons. In one type of decay, the chromophore is excited to the second excited state of singlet character from where it returns to the ground state through radiationless decays. The absorbed energy was then converted into vibrational energy. There is a finite probability that sufficient energy to cause dissociation is localized in one vibrational mode, and consequently the ions dissociated on the millisecond timescale. The second type of decay occurs on a much faster timescale, the lifetime for dissociation being 100 ns. It was found that this faster decay is due to ions that have absorbed two photons. In this process, more energy is deposited into the vibrational modes, and dissociation happens on a much faster timescale.

A P P E N D I X

APPENDIX A

Space charge potential

The space charge potential created by the electron beam in the electron cooler was discussed in section 3.2.2. In the following section, the expression from Eq. (3.5) is derived.

The electron beam can be regarded as a uniform cylindrical charge distribution with radius, R_e. The charge density is given by $-en_e$. To obtain an expression for the electrical field inside the charge distribution, i.e. for $r < R_e$, a coaxial Gaussian cylinder of radius, r, and length, L, is drawn (see Fig. A.1). For this surface, Gauss's law states:

$$\oint_S \mathbf{E} \cdot \mathrm{d}\mathbf{a} = \frac{1}{\epsilon_0} Q_{\mathrm{enc}}, \tag{A.1}$$

where the enclosed charge, Q_{enc}, is

$$Q_{\mathrm{enc}} = \int -e\, n_e \, \mathrm{d}V = -en_e \pi r^2 L. \tag{A.2}$$

The cylindrical symmetry of the charge distribution dictates that the electrical field, $\mathbf{E}$, must point in the radial direction, and that $|\mathbf{E}|$ only depends on the distance to the axis. Hence, the magnitude of the electrical field is constant on the curved surface of the Gaussian cylinder. Furthermore, the surface element, $\mathrm{d}\mathbf{a}$, and $\mathbf{E}$ are parallel in every point, and for this curved portion of the surface, the integral therefore yields:

$$\int \mathbf{E} \cdot \mathrm{d}\mathbf{a} = \int |\mathbf{E}| \mathrm{d}a = |\mathbf{E}| \int \mathrm{d}a = |\mathbf{E}| 2\pi r L. \tag{A.3}$$

As the two ends do not contribute to the surface integral (here $\mathbf{E}$ is perpendic-

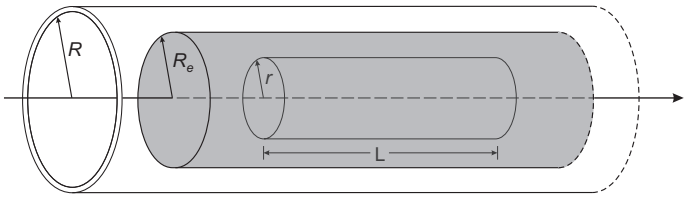

Figure A.1: Cylindrical charge distribution of radius, R_e, surrounded by a coaxial cylindrical chamber of radius, R. A Gaussian surface of radius, r, and length, L, is drawn inside the charge distribution.

ular to d**a**) Eq. (A.1) becomes:

$$\begin{aligned} &|\mathbf{E}|2\pi rL = \oint_S \mathbf{E}\cdot \mathrm{d}\mathbf{a} = \frac{1}{\epsilon_0}Q_{\mathrm{enc}} = \frac{-en_{\mathrm{e}}}{\epsilon_0}\pi r^2 L \\ &\Downarrow \\ &\mathbf{E}(\mathbf{r}) = -\frac{en_{\mathrm{e}}r}{2\epsilon_0}\hat{r},\ r < R_{\mathrm{e}}. \end{aligned} \tag{A.4}$$

The electrical field in the region between the chamber and the charged distribution, i.e. $R_{\mathrm{e}} < r < R$, can be calculated in a similar manner. By applying Gauss's law to a coaxial cylinder with radius r where $R_{\mathrm{e}} < r < R$, **E** is found to be:

$$\begin{aligned} &|\mathbf{E}|2\pi rL = \oint_S \mathbf{E}\cdot \mathrm{d}\mathbf{a} = \frac{1}{\epsilon_0}Q_{\mathrm{enc}} = \frac{-en_{\mathrm{e}}}{\epsilon_0}\pi R_{\mathrm{e}}^2 L \\ &\Downarrow \\ &\mathbf{E}(\mathbf{r}) = -\frac{en_{\mathrm{e}}R_{\mathrm{e}}^2}{2\epsilon_0 r}\hat{r},\ R_{\mathrm{e}} < r < R. \end{aligned} \tag{A.5}$$

The relation between the electric field and the potential is given by:

$$V(\mathbf{r}) = -\int_{\mathcal{O}}^{\mathbf{r}} \mathbf{E}\cdot \mathrm{d}\mathbf{l}, \tag{A.6}$$

where $\mathcal{O}$ is a reference point at which the potential is zero. The electron beam is surrounded by the grounded vacuum chamber of radius, R, and the reference point is therefore chosen to be at distance R from the axis. The space charge potential in the region inside the vacuum chamber but outside the electron beam is calculated to be:

$$V_{\mathrm{sp}}(\mathbf{r}) = -\int_{\mathbf{R}}^{\mathbf{r}} \mathbf{E}\cdot \mathrm{d}\mathbf{l} = \int_R^r \frac{en_{\mathrm{e}}R_{\mathrm{e}}^2}{2\epsilon_0 r'}\mathrm{d}r' = \frac{en_{\mathrm{e}}R_{\mathrm{e}}^2}{2\epsilon_0}\ln\left(\frac{r}{R}\right),\ R_{\mathrm{e}} < r < R, \tag{A.7}$$

whereas the potential inside the electron beam is

$$\begin{aligned} V_{\mathrm{sp}}(\mathbf{r}) &= -\int_{\mathbf{R}}^{\mathbf{r}} \mathbf{E}\cdot \mathrm{d}\mathbf{l} = \int_{R}^{R_{\mathrm{e}}} \frac{en_{\mathrm{e}}R_{\mathrm{e}}^2}{2\epsilon_0 r'}\mathrm{d}r' + \int_{R_{\mathrm{e}}}^{r} \frac{en_{\mathrm{e}}r'}{2\epsilon_0}\mathrm{d}r' \\ &= \frac{en_{\mathrm{e}}R_{\mathrm{e}}^2}{4\epsilon_0}\left[2\ln\left(\frac{R_{\mathrm{e}}}{R}\right) + \left(\frac{r}{R_{\mathrm{e}}}\right)^2 - 1\right], r < R_{\mathrm{e}}. \end{aligned} \tag{A.8}$$

This result is recognized as the expression from Eq. (3.5). In experiments, the known quantities are the electron current, I_{e}, and the electron energy in the laboratory frame, $E_{\mathrm{e}}^{\mathrm{lab}}$, and hence the above equations are more convenient when expressed in terms of these variables. Substituting n_{e} by the electron current, $I_{\mathrm{e}} = en_{\mathrm{e}}\pi R_{\mathrm{e}}^2 v_{\mathrm{e}}$, and the electron velocity, v_{e}, by $E_{\mathrm{e}}^{\mathrm{lab}}$, the following is obtained:

$$V_{\mathrm{sp}}(\mathbf{r}) = \frac{I_{\mathrm{e}}}{\sqrt{E_{\mathrm{e}}^{\mathrm{lab}}}}\frac{\sqrt{m_{\mathrm{e}}}}{4\pi\epsilon_0\sqrt{2}}\cdot\begin{cases} 2\ln\left(\frac{r}{R}\right), & R_{\mathrm{e}} < r < R \\ 2\ln\left(\frac{R_{\mathrm{e}}}{R}\right) + \left(\frac{r}{R_{\mathrm{e}}}\right)^2 - 1, & r < R_{\mathrm{e}} \end{cases}. \tag{A.9}$$

The space charge constant, $K_{\mathrm{sp}}(\mathbf{r})$, is introduced as the part of the potential only depending on the geometry, and $V_{\mathrm{sp}}(\mathbf{r})$ is finally expressed as:

$$V_{\mathrm{sp}}(\mathbf{r}) = -K_{\mathrm{sp}}(r)\frac{I_{\mathrm{e}}}{\sqrt{E_{\mathrm{e}}^{\mathrm{lab}}}}, \tag{A.10}$$

where

$$K_{\mathrm{sp}}(r) = -\frac{\sqrt{m_{\mathrm{e}}}}{4\pi\epsilon_0\sqrt{2}}\cdot\begin{cases} 2\ln\left(\frac{r}{R}\right), & R_{\mathrm{e}} < r < R \\ 2\ln\left(\frac{R_{\mathrm{e}}}{R}\right) + \left(\frac{r}{R_{\mathrm{e}}}\right)^2 - 1, & r < R_{\mathrm{e}} \end{cases}. \tag{A.11}$$

Defined as above, the space charge constant is always positive. The value of the space charge constant can now be extracted as a function of the distance to the center axis. The radius of the vacuum chamber is $R = 5$ cm and the adiabatic expansion factor is kept at 4.5 yielding an electron beam radius of $R_{\mathrm{e}} = \sqrt{4.5}\cdot 0.5$ cm $= 1.06$ cm. Using these numbers, the result shown in Fig. A.2 is obtained.

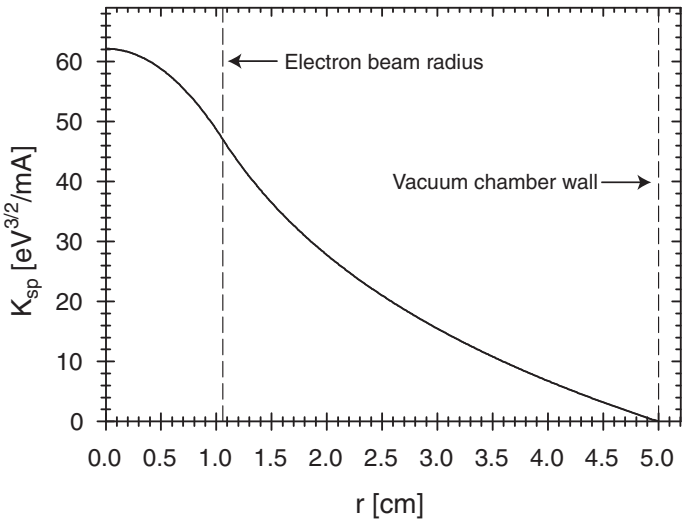

Figure A.2: Space charge constant as a function of the distance, *r*, to the center axis.

APPENDIX B

Collision energy spread in the merged-beams setup

The expression from Eq. (3.21) giving the collision energy spread in the merged-beams setup is derived in the following.

The electron velocity distribution is known both in the electron rest frame (Eq. (3.10)) and in the ion rest frame (Eq. (3.19)). Fig. B.1 shows the relation between the velocities entering the two distributions. The collision energy spread is most easily obtained by first relating the electron velocity in ion rest frame, **u**, to that in the electron rest frame, **v**. As Fig. B.1 implies:

$$u_\perp = v_\perp, \quad u_\parallel = v_\parallel + \Delta. \tag{B.1}$$

The collision energy, E_e, is the electron energy in the ion rest frame, and from the result above it is expressed as:

$$\begin{aligned} E_\mathrm{e} &= \frac{1}{2} m_\mathrm{e}(u_\perp^2 + u_\parallel^2) = \frac{1}{2} m_\mathrm{e}(v_\perp^2 + (v_\parallel + \Delta)^2) \\ &= \frac{1}{2} m_\mathrm{e} v_\perp^2 + \frac{1}{2} m_\mathrm{e} v_\parallel^2 + E_\mathrm{d} + m_\mathrm{e} v_\parallel \Delta. \end{aligned} \tag{B.2}$$

$E_\mathrm{d} = m_\mathrm{e}\Delta^2/2$ is the detuning energy assumed to be a constant as the ion velocity spread is negligible. The transversal and longitudinal velocities are independent variables, as their joint distribution (see Eq. (3.10)) is a product of the individual distributions [199]. Therefore it is obvious to exploit the fact that the variance of a sum of variables, $X = \sum X_i$, can be calculated according to [199]:

$$\mathrm{var}(X) = \langle X^2 \rangle - \langle X \rangle^2 = \sum_{i=1}^{n} \mathrm{var}(X_i) + 2 \sum_{1 \le i \le j \le n} \mathrm{cov}(X_i, X_j). \tag{B.3}$$

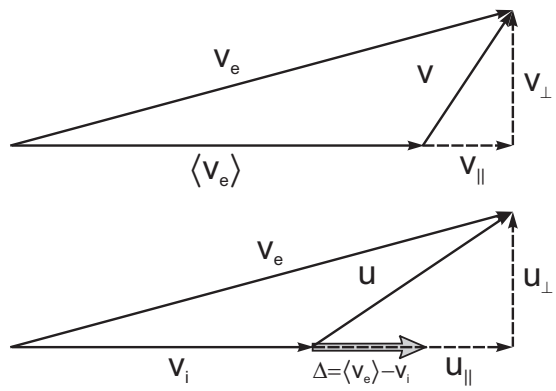

Figure B.1: Illustration of the different velocity definitions in Eqs (3.10) and (3.19).

Here, $\mathrm{cov}(X, Y)$ is the covariance of X and Y defined as:

$$\mathrm{cov}(X, Y) = \langle XY \rangle - \langle X \rangle \langle Y \rangle, \tag{B.4}$$

which is zero if the variables, X and Y, are independent. Combining all of the above, the variance of the collision energy can be found:

$$\begin{aligned} \mathrm{var}\left(E_\mathrm{e}\right) =& \mathrm{var}\left(\frac{1}{2} m_\mathrm{e} v_\perp^2\right) + \mathrm{var}\left(\frac{1}{2} m_\mathrm{e} v_\parallel^2\right) + \Delta^2 m_\mathrm{e}^2 \mathrm{var}\left(v_\parallel\right) \\ &+ \Delta m_\mathrm{e}^2 \mathrm{cov}\left(v_\parallel^2, v_\parallel\right). \end{aligned} \tag{B.5}$$

The longitudinal velocity distribution is symmetric around $v_\parallel = 0$ meaning that $\langle v_\parallel^n \rangle = 0$ for n odd. Thus, the last term above disappears since only odd moments is seen to enter in the covariance of $v_\parallel^2$ and $v_\parallel$. The three remaining variances are found by calculating $\langle v_{\parallel,\perp}^2 \rangle$ and $\langle v_{\parallel,\perp}^4 \rangle$ from the distribution given in Eq. (3.10). The result is:

$$\mathrm{var}\left(E_\mathrm{e}\right) = \left(kT_\perp\right)^2 + \frac{1}{2}\left(kT_\parallel\right)^2 + 2E_\mathrm{d} kT_\parallel. \tag{B.6}$$

The collision energy spread, $\delta E_\mathrm{e}(E_\mathrm{d})$, is defined as the square root of the variance, and the expression from Eq. (3.21) is now retained:

$$\delta E_\mathrm{e}(E_\mathrm{d}) = \sqrt{\mathrm{var}\left(E_\mathrm{e}\right)} = \sqrt{\left(kT_\perp\right)^2 + \frac{1}{2}\left(kT_\parallel\right)^2 + 2E_\mathrm{d} kT_\parallel}. \tag{B.7}$$

References

[1] T. Andersen, *Spectroscopy of Negative Ions*, Physica Scripta **T34**, 23 (1991).

[2] R. Wildt, *Electron Affinity in Astrophysics*, Astrophys. J. **89**, 295 (1939).

[3] R. Wildt, *The Continuous spectrum of stellar atmospheres consisting only of atoms and negative ions of hydrogen*, Astrophys. J. **93**, 47 (1941).

[4] S. Chandrasekhar, *On the Continuous absorption coefficient of the negative Hydrogen ion*, Astrophys. J. **102**, 223 (1945).

[5] L. M. Branscomb and S. J. Smith, *Experimental Cross Section for Photodetachment of Electrons from H^- and D^-*, Phys. Rev. **98**, 1028 (1955).

[6] R. Terzieva and E. Herbst, *Radiative electron attachment to small linear carbon clusters and its significance for the chemistry of diffuse interstellar clouds*, Int. J. Mass Spec. **201**, 135 (2000).

[7] D. K. Chakrabarty, *On unequal distributions of positive and negative ions in the upper stratosphere*, Adv. Space Res. **20**, 2191 (1997).

[8] E. Kopp, *A global model of positive and negative ions in the lower ionosphere*, Adv. Space Res. **25**, 173 (2000).

[9] M. J. Jensen, *Dynamic processes in molecules*, Ph.D. thesis, University of Aarhus, Denmark (2001).

[10] L. Vejby-Christensen, D. Kella, D. Mathur, H. B. Pedersen, H. T. Schmidt, and L. H. Andersen, *Electron-impact detachment from negative ions*, Phys. Rev. A **53**, 2371 (1996).

[11] H. B. Pedersen, N. Djurić, M. J. Jensen, D. Kella, C. P. Safvan, H. T. Schmidt, L. Vejby-Christensen, and L. H. Andersen, *Electron collisions with diatomic anions*, Phys. Rev. A **60**, 2882 (1999).

[12] H. B. Pedersen, R. Bilodeau, M. J. Jensen, I. V. Makassiouk, C. P. Safvan, and L. H. Andersen, *Electron collisions with the diatomic fluorine anion*, Phys. Rev. A **63**, 032718 (2001).

[13] G. F. Collins, D. J. Pegg, K. Fritioff, J. Sandström, D. Hanstorp, R. D. Thomas, F. Hellberg, A. Ehlerding, M. Larsson, F. Österdahl, A. Källberg, and H. Danared, *Electron-impact fragmentation of* Cl_2^-, Phys. Rev. A **72**, 042708 (2005).

[14] H. S. Taylor, G. V. Nazaroff, and A. Golebiewski, *Qualitative Aspects of Resonances in Electron-Atom and Electron-Molecule Scattering, Excitation, and Reactions*, J. Chem. Phys. **45**, 2872 (1966).

[15] G. J. Schulz, *Resonances in electron impact on atoms*, Rev. Mod. Phys. **45**, 378 (1973).

[16] A. Dreuw and L. S. Cederbaum, *Nature of the repulsive Coulomb barrier in multiply charged negative ions*, Phys. Rev. A **63**, 012501 (2000).

[17] M. K. Scheller, R. N. Compton, and L. S. Cederbaum, *Gas-Phase Multiply Charged Anions*, Science **270**, 1160 (1995).

[18] J. Simons, P. Skurski, and R. Barrios, *Repulsive Coulomb Barriers in Compact Stable and Metastable Multiply Charged Anions*, J. Am. Chem. Soc. **122**, 11893 (2000).

[19] L.-S. Wang, C.-F. Ding, X.-B. Wang, and J. B. Nicholas, *Probing the Potential Barriers and Intramolecular Electrostatic Interactions in Free Doubly Charged Anions*, Phys. Rev. Lett. **81**, 2667 (1998).

[20] X.-B. Wang, C.-F. Ding, and L.-S. Wang, *Photodetachment Spectroscopy of a Doubly Charged Anion: Direct Observation of the Repulsive Coulomb Barrier*, Phys. Rev. Lett. **81**, 3351 (1998).

[21] L. H. Andersen, R. Bilodeau, M. J. Jensen, S. B. Nielsen, C. P. Safvan, and K. Seiersen, *Coulomb and centrifugal barrier bound dianion resonances of* NO_2, J. Chem. Phys. **114**, 147 (2001).

[22] G. Tisone and L. M. Branscomb, *Detachment of Electrons From* H^- *by Electron Impact*, Phys. Rev. Lett. **17**, 236 (1966).

[23] D. F. Dance, M. F. A. Harrison, and R. D. Rundel, *A measurement of the cross-section for detachment of electrons from* H^- *by electron impact*, Proc. R. Soc. A **299**, 525 (1967).

[24] G. C. Tisone and L. M. Branscomb, *Detachment of Electrons from H^- and O^- Negative Ions by Electron Impact*, Phys. Rev. **170**, 169 (1968).

[25] B. Peart, D. S. Walton, and K. T. Dolder, *Electron detachment from H^- ions by electron impact*, J. Phys. B **3**, 1346 (1970).

[26] D. S. Walton, B. Peart, and K. T. Dolder, *Structure observed during detailed measurements of detachment from H^- by electron impact*, J. Phys. B **3**, L148 (1970).

[27] D. S. Walton, B. Peart, and K. T. Dolder, *A measurement of cross sections for detachment from H^- by a method employing inclined ion and electron beams*, J. Phys. B **4**, 1343 (1971).

[28] B. Peart and K. T. Dolder, *Measurements which indicate the existence of a second short-lived state of H^{2-}*, J. Phys. B **6**, 1497 (1973).

[29] B. Peart, R. A. Forrest, and K. T. Dolder, *A search for structure in cross sections for detachment from C^- and O^- ions by electron impact*, J. Phys. B **12**, 2735 (1979).

[30] B. Peart, R. Forrest, and K. T. Dolder, *Measurements of cross sections for detachment of electrons from C^- and O^- ions by electron impact*, J. Phys. B **12**, 847 (1979).

[31] B. Peart, R. Forrest, and K. T. Dolder, *Measurements of detachment from F^- by electron impact and tests of classical scaling for electron impact detachment cross sections*, J. Phys. B **12**, L115 (1979).

[32] M. Larsson, *Atomic and molecular physics with ion storage rings*, Rep. Prog. Phys. **58**, 1267 (1995).

[33] L. H. Andersen, T. Andersen, and P. Hvelplund, *Studies of Negative Ions in Storage Rings*, Adv. At. Mol. Opt. Phys. **38**, 155 (1997).

[34] L. H. Andersen, D. Mathur, H. T. Schmidt, and L. Vejby-Christensen, *Electron-Impact Detachment of D^-: Near-Threshold Behavior and the Nonexistence of D^{2-} Resonances*, Phys. Rev. Lett. **74**, 892 (1995).

[35] T. Tanabe, I. Katayama, H. Kamegaya, K. Chida, T. Watanabe, Y. Arakaki, M. Yoshizawa, Y. Haruyama, M. Saito, T. Honma, K. Hosono, K. Hatanaka, F. J. Currell, and K. Noda, *Search for H^{2-} resonances in the detachment of H^- by electron impact with a high-resolution cooler ring*, Phys. Rev. A **54**, 4069 (1996).

[36] L. H. Andersen, M. J. Jensen, H. B. Pedersen, L. Vejby-Christensen, and N. Djurić, *Electron-impact detachment from B^-*, Phys. Rev. A **58**, 2819 (1998).

[37] K. Andersson, D. Hanstorp, A. Neau, S. Rosén, H. T. Schmidt, R. Thomas, M. Larsson, J. Semaniak, F. Österdahl, H. Danared, A. Källberg, and A. Le Padellec, *Electron impact single detachment on the F^- ions using the heavy ion storage ring CRYRING: Cross-section determination*, Eur. Phys. J. D **13**, 323 (2001).

[38] A. Le Padellec, G. F. Collins, H. Danared, A. Källberg, F. Hellberg, A. Neau, K. Fritioff, D. Hanstorp, and M. Larsson, *Relative cross sections for the electron impact single detachment on Li^-*, J. Phys. B **35**, 3669 (2002).

[39] K. Fritioff, J. Sandström, D. Hanstorp, A. Ehlerding, M. Larsson, G. F. Collins, D. J. Pegg, H. Danared, A. Källberg, and A. Le Padellec, *Electron-impact detachment from Cl^-*, Phys. Rev. A **68**, 012712 (2003).

[40] K. Fritioff, J. Sandström, D. Hanstorp, F. Hellberg, A. Ehlerding, M. Larsson, G. F. Collins, D. J. Pegg, H. Danared, and A. Källberg, *Electron-impact detachment from S^-*, Eur. Phys. J. D **27**, 23 (2003).

[41] K. Fritioff, J. Sandström, P. Andersson, D. Hanstorp, F. Hellberg, R. Thomas, W. Geppert, M. Larsson, F. Österdahl, G. F. Collins, D. J. Pegg, H. Danared, A. Källberg, and N. D. Gibson, *Single and double detachment from H^-*, Phys. Rev. A **69**, 042707 (2004).

[42] L. H. Andersen, P. Hvelplund, D. Kella, P. H. Mokler, H. B. Pedersen, H. T. Schmidt, and L. Vejby-Christensen, *Resonance structure in the electron-impact detachment cross section of C_2^- caused by the formation of C_2^{2-}*, J. Phys. B **29**, L643 (1996).

[43] H. B. Pedersen, N. Djurić, M. J. Jensen, D. Kella, C. P. Safvan, L. Vejby-Christensen, and L. H. Andersen, *Doubly Charged Negative Ions of B_2 and C_2*, Phys. Rev. Lett. **81**, 5302 (1998).

[44] A. Le Padellec, K. Andersson, D. Hanstorp, F. Hellberg, M. Larsson, A. Neau, S. Rosén, H. T. Schmidt, R. Thomas, J. Semeniak, D. J. Pegg, F. Österdahl, H. Danared, and A. Källberg, *Electron scattering on CN^-*, Physica Scripta **64**, 467 (2001).

[45] L. H. Andersen, J. Bak, S. Boyé, M. Clausen, M. Hovgaard, M. J. Jensen, A. Lapierre, and K. Seiersen, *Resonant and nonresonant electron impact detachment of CN^- and BO^-*, J. Chem. Phys. **115**, 3566 (2001).

[46] A. Le Padellec, F. Rabilloud, D. Pegg, A. Neau, F. Hellberg, R. Thomas, H. T. Schmidt, M. Larsson, H. Danared, A. Källberg, K. Andersson, and D. Hanstorp, *Electron-impact detachment and dissociation of C_4^- ions*, J. Chem. Phys. **115**, 10671 (2001).

[47] K. Seiersen, J. Bak, H. Bluhme, M. J. Jensen, S. B. Nielsen, and L. H. Andersen, *Electron-impact detachment of O_3^-, NO_3^- and SO_2^- ions*, Phys. Chem. Chem. Phys. **5**, 4814 (2003).

[48] K. Fritioff, J. Sandström, P. Andersson, D. Hanstorp, F. Hellberg, R. Thomas, M. Larsson, F. Österdahl, G. F. Collins, A. Le Padellec, D. J. Pegg, N. D. Gibson, H. Danared, and A. Källberg, *Observation of an excited C_4^{2-} ion*, J. Phys. B **37**, 2241 (2004).

[49] A. Svendsen, M. O. A. El Ghazaly, and L. H. Andersen, *Molecular size effect in NCO and NCS dianion resonances*, J. Chem. Phys. **123**, 114311 (2005).

[50] L. Lammich, S. Altevogt, H. Buhr, H. Kreckel, S. Krohn, M. Lange, D. Strasser, R. Repnow, M. Grieser, R. Schinke, Z.-W. Qu, H. Zhu, D. Schwalm, D. Zajfman, and A. Wolf, *Electron-impact dissociation and transient properties of a stored LiH_2^- beam*, submitted to Eur. Phys. J. D.

[51] S. P. Møller, *ELISA, an electrostactic storage ring for atomic physics*, Nucl. Instr. Meth. A **394**, 281 (1997).

[52] M. Dahan, R. Fishman, O. Heber, M. Rappaport, N. Altstein, D. Zajfman, and W. J. van der Zande, *A new type of electrostatic ion trap for storage of fast ion beams*, Rev. Sci. Instrum. **69**, 76 (1998).

[53] D. Zajfman, O. Heber, L. Vejby-Christensen, I. Ben-Itzhak, M. Rappaport, R. Fishman, and M. Dahan, *An electrostatic bottle for long time storage of fast ion beams*, Phys. Rev. A **55**, 1577 (1997).

[54] H. Bluhme, M. J. Jensen, S. B. Nielsen, U. V. Pedersen, K. Seiersen, A. Svendsen, and L. H. Andersen, *Electron scattering on stored mononucleotide anions*, Phys. Rev. A **70**, 020701 (2004).

[55] T. Tanabe, K. Noda, M. Saito, E. B. Starikov, and M. Tateno, *Regular Threshold-Energy Increase with Charge for Neutral-Particle Emission in Collisions of Electrons with Oligonucleotide Anions*, Phys. Rev. Lett. **93**, 043201 (2004).

[56] A. Diner, Y. Toker, D. Strasser, O. Heber, I. Ben-Itzhak, P. D. Witte, A. Wolf, D. Schwalm, M. L. Rappaport, K. G. Bhushan, and D. Zajfman, *Size-Dependent Electron-Impact Detachment of Internally Cold C_n^- and Al_n^- Clusters*, Phys. Rev. Lett. **93**, 063402 (2004).

[57] M. O. A. El Ghazaly, A. Svendsen, H. Bluhme, S. B. Nielsen, and L. H. Andersen, *Electron scattering on p-benzoquinone anions*, Chem. Phys. Lett. **405**, 278 (2005).

[58] M. Eritt, A. Diner, Y. Toker, O. Aviv, O. Heber, M. L. Rappaport, and D. Zajfman, *Size effects in the interaction between ionic clusters and low-energy electrons*, Physica Scripta **73**, C32 (2006).

[59] M. O. A. El Ghazaly, A. Svendsen, H. Bluhme, A. B. Nielsen, S. B. Nielsen, and L. H. Andersen, *Electron Scattering on Centrosymmetric Molecular Dianions Pt(CN)$_4^{2-}$ and Pt(CN)$_6^{2-}$*, Phys. Rev. Lett. **93**, 203201 (2004).

[60] H. Hotop and W. C. Lineberger, *Binding Energies in Atomic Negative Ions. II*, J. Phys. Chem. Ref. Data **14**, 731 (1985).

[61] E. P. Wigner, *On the Behavior of Cross Sections Near Thresholds*, Phys. Rev. **73**, 1002 (1948).

[62] G. H. Wannier, *The Threshold Law for Single Ionization of Atoms or Ions by Electrons*, Phys. Rev. **90**, 817 (1953).

[63] M. R. C. McDowell and J. H. Williamson, *Electron detachment from H^- by electrons*, Phys. Lett. **4**, 159 (1963).

[64] B. M. Smirnov and M. I. Chibisov, *Breaking up of atomic particles by an electric field and by electron collisons*, Sov. Phys. JETP **22**, 585 (1966).

[65] M. Inokuti and Y.-K. Kim, *Total Cross Sections for Inelastic Scattering of Charged Particles by Atoms and Molecules. II. Negative Hydrogen Ion*, Phys. Rev. **173**, 154 (1968).

[66] O. Bely and S. B. Schwartz, *Electron detachment from H^- by electron impact*, J. Phys. B **2**, 159 (1969).

[67] F. H. M. Faisal and A. K. Bhatia, *Electron Detachment of H^- by e^- Collision*, Phys. Rev. A **5**, 2144 (1972).

[68] T. L. John and B. Williams, *Coulomb effects on electron negative ion detachment*, J. Phys. B **6**, L381 (1973).

[69] K. L. Bell, A. E. Kingston, and P. J. Madden, *Ionisation of H^- by electron impact*, J. Phys. B **11**, 2547 (1978).

[70] R. W. Hart, E. P. Gray, and W. H. Guier, *Energy Dependence of Cross Sections near Threshold: One Neutral and Two Charged Reaction Products*, Phys. Rev. **108**, 1512 (1957).

[71] E. A. Solov'ev, *Classical approximation for the ionization of a negative ion by electron impact near the threshold*, Sov. Phys. JETP **45**, 1089 (1977).

[72] P. V. Grujić and N. Simonović, *$e + H^-$ detachment function: I. The classical-dynamic study*, J. Phys. B **31**, 2611 (1998).

[73] V. N. Ostrovsky and K. Taulbjerg, *Quantum tunneling and classical above-barrier transitions in electron detachment from negative ions by negatively charged projectiles*, J. Phys. B **29**, 2573 (1996).

[74] A. K. Kazansky and K. Taulbjerg, *Quantum wavepacket study of electron detachment from H^- by electron impact*, J. Phys. B **29**, 4465 (1996).

[75] J. T. Lin, T. F. Jiang, and C. D. Lin, *Coulomb trajectory effects on electron-impact detachment of negative ions and on mutual neutralization cross sections*, J. Phys. B **29**, 6175 (1996).

[76] J. M. Rost, *Threshold Detachment of Negative Ions by Electron Impact*, Phys. Rev. Lett. **82**, 1652 (1999).

[77] M. S. Pindzola, *Electron-impact detachment from the H^- and O^- negative ions*, Phys. Rev. A **54**, 3671 (1996).

[78] M. S. Pindzola and F. Robicheaux, *Ejected-energy differential cross sections for the electron-impact detachment of H^-*, J. Phys. B **33**, L427 (2000).

[79] F. Robicheaux, *Electron Impact Detachment of Weakly Bound Negative Ions*, Phys. Rev. Lett. **82**, 707 (1999).

[80] F. Robicheaux, *Electron-impact detachment of weakly bound negative ions: Threshold and scaling laws*, Phys. Rev. A **60**, 1206 (1999).

[81] Y. N. Demkov and G. F. Drukarev, *Decay and Polarizability of negative ions in an electric field*, Sov. Phys. JETP **20**, 614 (1965).

[82] H. Deutsch, P. Scheier, K. Becker, and T. D. Märk, *Calculated cross-sections for the electron-impact detachment from negative ions using the Deutsch-Märk (DM) formalism*, Chem. Phys. Lett. **382**, 26 (2003).

[83] A. I. Boldyrev and J. Simons, *Isolated SO_4^{2-} and PO_4^{3-} Anions Do Not Exist*, J. Phys. Chem. **98**, 2298 (1994).

[84] X.-B. Wang, J. B. Nicholas, and L.-S. Wang, *Electronic instability of isolated SO_4^{2-} and its solvation stabilization*, J. Chem. Phys. **113**, 10837 (2000).

[85] M. K. Scheller and L. S. Cederbaum, *Stability of MX_3^{2-} ions in the gas phase and when do ionic molecules have large ionization potentials*, J. Chem. Phys. **99**, 441 (1993).

[86] J. Kalcher and A. F. Sax, *Gas Phase Stabilities of Small Anions: Theory and Experiment in Cooperation*, Chem. Rev. **94**, 2291 (1994).

[87] L.-S. Wang and X.-B. Wang, *Probing Free Multiply Charged Anions Using Photodetachment Photoelectron Spectroscopy*, J. Phys. Chem. A **104**, 1978 (2000).

[88] A. Dreuw and L. S. Cederbaum, *Multiply Charged Anions in the Gas Phase*, Chem. Rev. **102**, 181 (2002).

[89] H. S. Taylor and L. D. Thomas, *Short-Lived Resonant State of H^{--}*, Phys. Rev. Lett. **28**, 1091 (1972).

[90] L. D. Thomas, *Identification of a second resonant state of H^{2-}*, J. Phys. B **7**, L97 (1974).

[91] M. Anbar and R. Schnitzer, *Doubly Charged Negative Atomic Ions of Hydrogen*, Science **191**, 463 (1976).

[92] R. Schnitzer and M. Anbar, *Existence of H^{2-}, a relatively long-lived doubly charged negative atomic hydrogen ion*, J. Chem. Phys. **64**, 2466 (1976).

[93] R. Schnitzer and M. Anbar, *Existence of H^{2-}: Additional experimental evidence*, J. Chem. Phys. **65**, 4332 (1976).

[94] B. Simon, *Resonances and complex scaling: a rigorous overview*, Int. J. Quantum Chem. **14**, 529 (1978).

[95] T. Morishita, C. D. Lin, and C. G. Bao, *Nonexistence of Resonances in H^{2-}*, Phys. Rev. Lett. **80**, 464 (1998).

[96] T. Sommerfeld, U. V. Riss, H.-D. Meyer, and L. S. Cederbaum, *Evidence for a metastable state of the fundamental dianion H^{2-}*, Phys. Rev. A **55**, 1903 (1997).

[97] K. T. Chung, *Channel coupling and exchange interaction in negative ions*, Phys. Rev. A **58**, 2777 (1998).

[98] M. Bylicki and C. A. Nicolaides, *The H^{2-} $^4S^o$ spectrum has at least two resonance states*, J. Phys. B **31**, L685 (1998).

[99] W. K. Stuckey and R. W. Kiser, *Doubly charged Negative Ions of Oxygen, Fluorine, Chlorine and Bromine*, Nature **211**, 963 (1966).

[100] H. Baumann, E. Heinicke, H. J. Kaiser, and K. Bethge, *On the existence of doubly negative charged heavy ions*, Nucl. Instr. Meth. **95**, 389 (1971).

[101] L. Frees, E. Heinicke, and W. Koski, *Concerning doubly charged negative ions of iodine in the gas phase*, Nucl. Instr. Meth. **159**, 105 (1979).

[102] D. Spence, W. A. Chupka, and C. M. Stevens, *Search for long-lived doubly charged atomic negative ions*, Phys. Rev. A **26**, 654 (1982).

[103] K. H. Chang, R. D. McKeown, R. G. Milner, and J. Labrenz, *Search for long-lived doubly charged negative atomic ions*, Phys. Rev. A **35**, 3949 (1987).

[104] H. Hogreve, *On the maximal electronic charge bound by atomic nuclei*, J. Phys. B **31**, L439 (1998).

[105] T. Sommerfeld, *Resonance States of Atomic Di-anions*, Phys. Rev. Lett. **85**, 956 (2000).

[106] A. V. Sergeev and S. Kais, *Resonance States of Atomic Anions*, Int. J. Quantum Chem. **82**, 255 (2001).

[107] A. I. Boldyrev and J. Simons, *Theoretical search for small linear doubly charged anions*, J. Chem. Phys. **98**, 4745 (1993).

[108] T. Sommerfeld, *Lifetimes of Metastable Dianions: CN_2^{2-}, C_4^{2-}, and CO_3^{2-}*, J. Phys. Chem. A **104**, 8806 (2000).

[109] T. Sommerfeld, F. Tarantelli, H.-D. Meyer, and L. S. Cederbaum, *Ab initio calculation of energies and lifetimes of metastable dianions: The C_2^{2-} resonance*, J. Chem. Phys. **112**, 6635 (2000).

[110] P. J. Bruna, R. M. Mawhinney, and F. Grein, *Theoretical study of the stability of the dianion BN^{2-} and the related species LiBNLi, NaBNNa and BNCa*, J. Phys. B **29**, 2413 (1996).

[111] T. Sommerfeld, U. V. Riss, H.-D. Meyer, and L. S. Cederbaum, *Metastable C_2^{2-} Dianion*, Phys. Rev. Lett. **79**, 1237 (1997).

[112] R. C. Dougherty, *Negative-Ion Mass Spectrum of Benzol[cd]-pyrene-6-one. Evidence for a Doubly Charged Negative Ion in the Gas Phase*, J. Chem. Phys. **50**, 1896 (1969).

[113] S. N. Schauer, P. Williams, and R. N. Compton, *Production of Small Doubly Charged Negative Carbon Cluster Ions by Sputtering*, Phys. Rev. Lett. **65**, 625 (1990).

[114] H.-G. Weikert, L. S. Cederbaum, F. Tarantelli, and A. I. Boldyrev, *On the existence of free doubly negative molecular ions*, Z. Phys. D **18**, 299 (1991).

[115] H.-G. Weikert and L. S. Cederbaum, *Free doubly negative tetrahalides*, J. Chem. Phys. **99**, 8877 (1993).

[116] R. Middleton and J. Klein, *Experimental verification of the existence of the gas-phase dianions* BeF_4^{2-} *and* MgF_4^{2-}, Phys. Rev. A **60**, 3515 (1999).

[117] M. K. Scheller and L. S. Cederbaum, *Existence of doubly-negative charged ions and relation to solids*, J. Phys. B **25**, 2257 (1992).

[118] X.-L. Zhao and A. E. Litherland, *Observation of* LiF_3^{2-}, Phys. Rev. A **71**, 064501 (2005).

[119] J. Klein and R. Middleton, *Observation of* BeC_n^{2-}*, a particularly abundant gaseous dianion*, Nucl. Instr. Meth. B **159**, 8 (1999).

[120] A. Dreuw and L. S. Cederbaum, *Tunnelling lifetimes of metastable and binding properties of stable covalent* BeC_n^{2-} *(*$n = 4, 6$*) dianions*, J. Chem. Phys. **112**, 7400 (2000).

[121] H. Gnaser, A. Dreuw, and L. S. Cederbaum, *Discovery of a new class of stable gas-phase dianions: Mixed oxygen-carbon cluster* OC_n^{2-} *(*$n = 5$–19*)*, J. Chem. Phys. **117**, 7002 (2002).

[122] X.-B. Wang and L.-S. Wang, *Observation of negative electron-binding energy in a molecule*, Nature **400**, 245 (1999).

[123] X.-B. Wang, C.-F. Ding, J. B. Nicholas, D. A. Dixon, and L.-S. Wang, *Investigation of Free Singly and Doubly Charged Alkali Metal Sulfate Ion Pairs:* $M^+(SO_4^{2-})$ *and* $[M^+(SO_4^{2-})]_2$ *(M = Na, K)*, J. Phys. Chem. A **103**, 3423 (1999).

[124] X.-B. Wang, X. Yang, J. B. Nicholas, and L.-S. Wang, *Photodetachment of hydrated oxalate dianions in the gas phase,* $C_2O_4^{2-}(H_2O)_n$ *(*$n = 3$–40*): From solvated clusters to nanodroplet*, J. Chem. Phys. **119**, 3631 (2003).

[125] X.-B. Wang, X. Yang, J. B. Nicholas, and L.-S. Wang, *Bulk-Like Features in the Photoemission Spectra of Hydrated Doubly Charged Anion Clusters*, Science **294**, 1322 (2001).

[126] X. Yang, X.-B. Wang, and L.-S. Wang, *Photodetachment of Hydrated Sulfate Doubly Charged Anions:* $SO_4^{2-}(H_2O)_n$ *(*$n = 4$–40*)*, J. Phys. Chem. A **106**, 7607 (2002).

[127] B. Minofar, L. Vrbka, M. Mucha, P. Jungwirth, X. Yang, X.-B. Wang, Y.-J. Fu, and L.-S. Wang, *Interior and Interfacial Aqueous Solvation of Benzene Dicarboxylate Dianions and Their Methylated Analogues: A Combined Molecular Dynamics and Photoelectron Spectroscopy Study*, J. Phys. Chem. A **109**, 5042 (2005).

[128] X.-B. Wang, X. Yang, and L.-S. Wang, *Probing solution-phase species and chemistry in the gas phase*, Int. Rev. Phys. Chem. **21**, 473 (2002).

[129] R. Middleton and C. T. Adams, *A Close to Universal Negative Ion Source*, Nucl. Instr. Meth. **118**, 329 (1974).

[130] H. H. Andersen and P. Tykesson, *A PIG sputter source for negative ions*, IEEE Trans. Nucl. Sci. **22**, 1632 (1975).

[131] P. Tykesson, H. H. Andersen, and J. Heinemeier, *Further Investigations of ANIS (Aarhus Negative-Ion Source)*, IEEE Trans. Nucl. Sci. **23**, 1104 (1976).

[132] V. E. Krohn, *Emission of Negative Ions from Metal Surfaces Bombarded by Positive Cesium Ions*, J. Appl. Phys. **33**, 3523 (1962).

[133] D. E. Holmgren, *Excitation and spectroscopy of quartet level of Lithium, Sodium, and Cesium using a pulsed hollow-cathode discharge*, Ph.D. thesis, Stanford University, USA (1984).

[134] M. Ohring, *The Materials Science of Thin Films,* (Academic Press, 1992), chapter 3, pp. 101–109.

[135] S. P. Møller, *ASTRID - A Storage Ring for Ions and Electrons*, in *Conference Record of the 1991 IEEE Particle Accelerator Conference*, edited by L. Lizama (New York, 1991), p. 2811.

[136] S. P. Møller, *ASTRID - A small Multi-Purpose Storage Ring*, in *Proceedings of the Third European Particle Accelerator Conference* (Berlin, 1992).

[137] ISA research, URL: *http://www.isa.au.dk/research/sr-research.html*.

[138] H. Poth, *Electron cooling: theory, experiment, application*, Phys. Rep. **196**, 135 (1990).

[139] J. R. Pierce, *Rectilinear Electron Flow in Beams*, J. Appl. Phys. **11**, 548 (1940).

[140] C. D. Child, *Discharge from Hot CaO*, Phys. Rev. **32**, 492 (1911).

[141] L. H. Andersen, J. Bolko, and P. Kvistgaard, *State-selective dielectronic-recombination measurements for He- and Li-like carbon and oxygen ions*, Phys. Rev. A **41**, 1293 (1990).

[142] N. Madsen, *Dynamics of laser-cooled ion beams*, Ph.D. thesis, University of Aarhus, Denmark (1998).

[143] J. S. Nielsen, S. P. Møller, L. H. Andersen, P. Balling, and M. K. Raarup, *Electron cooling of D^- at the ASTRID storage ring*, Nucl. Instr. Meth. A **441**, 150 (2000).

[144] F. Mandl, *Statistical Physics*, 2nd edition (Wiley, 1988), chapter 7, pp. 210–214.

[145] H. Danared, *Fast electron cooling with a magnetically expanded electron beam*, Nucl. Instr. Meth. A **335**, 397 (1993).

[146] M. Born, *The Mechanics of the Atom*, (Ungar, New York, 1960), chapter 2, pp. 57–59.

[147] J. D. Jackson, *Classical Electrodynamics*, 3rd edition (Wiley, New York, 1999), chapter 12.

[148] T. J. Morgan, K. H. Berkner, and R. V. Pyle, *Cross Sections for Destruction of 1- to 25-keV/Nucleon Hydrogen Molecules in Collisions with H_2 Gas*, Phys. Rev. Lett. **26**, 602 (1971).

[149] J. B. A. Mitchell, J. L. Forand, C. T. Ng, C. P. Levac, R. E. Mitchell, P. M. Mul, W. Claeys, A. Sen, and J. W. McGowan, *Measurement of the Branching Ratio for the Dissociative Recombination of $H_3^+ + e$*, Phys. Rev. Lett. **51**, 885 (1983).

[150] S. Datz, G. Sundström, C. Biedermann, L. Broström, H. Danared, S. Mannervik, J. R. Mowat, and M. Larsson, *Branching Processes in the Dissociative Recombination of H_3^+*, Phys. Rev. Lett. **74**, 896 (1995).

[151] L. H. Andersen, O. Heber, D. Kella, H. B. Pedersen, L. Vejby-Christensen, and D. Zajfman, *Production of Water Molecules from Dissociative Recombination of H_3O^+ with Electrons*, Phys. Rev. Lett. **77**, 4891 (1996).

[152] S. P. Møller, *Design and first operation of the electrostatic storage ring, elisa*, in *Proc. 6th European Particle Accelerator Conference* (1998), p. 73.

[153] A. Fleischmann, C. Enss, and G. Seidel, *Metallic magnetic calorimeters*, in *Topics in Applied Physics volume 99. Cryogenic Particle Detection*, edited by C. Enss (Springer-Verlag, 2005), pp. 151–216.

[154] M. J. Jensen, U. V. Pedersen, and L. H. Andersen, *Stability of the Ground State Vinylidene Anion H_2CC^-*, Phys. Rev. Lett. **84**, 1128 (2000).

[155] U. V. Pedersen, M. Hyde, S. P. Møller, and T. Andersen, *Lifetime measurement of He^- utilizing an electrostatic ion storage ring*, Phys. Rev. A **64**, 012503 (2001).

[156] S. J. Buckman and C. W. Clark, *Atomic negative-ion resonances*, Rev. Mod. Phys. **66**, 539 (1994).

[157] T. Andersen, *Atomic negative ions: structure, dynamics and collisions*, Phys. Rep. **394**, 157 (2004).

[158] M. J. Travers, D. C. Cowles, and G. B. Ellison, *Reinvestigation of the electron affinities of O_2 and NO*, Chem. Phys. Lett. **164**, 449 (1989).

[159] J. D. Jackson, *Classical Electrodynamics*, 3rd edition (Wiley, New York, 1999), chapter 13.

[160] NIST Chemistry WebBook, URL: *http://webbook.nist.gov/chemistry/*.

[161] J. C. Rienstra-Kiracofe, G. S. Tschumper, H. F. Schaefer, S. Nandi, and G. B. Ellison, *Atomic and Molecular Electron Affinities: Photoelectron Experiments and Theoretical Computations*, Chem. Rev. **102**, 231 (2002).

[162] P. F. Zittel and W. C. Lineberger, *Laser photoelectron spectrometry of PO^-, PH^-, and PH_2^-*, J. Chem. Phys. **65**, 1236 (1976).

[163] C. Xu, E. de Beer, and D. M. Neumark, *Photoelectron Spectroscopy of PO_2^-*, J. Chem. Phys. **104**, 2749 (1996).

[164] X.-B. Wang and L.-S. Wang, *Vibrationally resolved photoelectron spectroscopy of PO_3^- and the electronic structure of PO_3*, Chem. Phys. Lett. **313**, 179 (1999).

[165] D. Feldmann, *Infra Red Photodetachment Threshold Measurements: Li^- and P^-*, Z. Phys. A **277**, 19 (1976).

[166] B. M. Smirnov, *Negative Ions* (McGraw-Hill Inc., 1982).

[167] M. Smits, C. A. de Lange, A. Stolow, and D. M. Rayner, *Dynamic Polarization in the Strong-Field Ionization of Small Metal Clusters*, Phys. Rev. Lett. **93**, 203402 (2004).

[168] K. M. Ervin, J. Ho, and W. C. Lineberger, *Ultraviolet Photoelectron Spectrum of NO_2^-*, J. Phys. Chem. **92**, 5405 (1988).

[169] E. E. Ferguson and F. Arnold, *Ion Chemistry of the Stratosphere*, Acc. Chem. Res. **14**, 327 (1981).

[170] R. S. MacTaylor and A. W. Castleman Jr., *Cluster Ion Reactions: Insights into Processes of Atmospheric Significance*, J. Atmos. Chem. **36**, 23 (2000).

[171] A. W. Castleman Jr. and I. N. Tang, *Role of Small Clusters in Nucleation about Ions*, J. Chem. Phys. **57**, 3629 (1972).

[172] R. G. Harrison, *Cloud formation and the possible significance of charge for atmospheric condensation and ice nuclei*, Space Sci. Rev. **94**, 381 (2000).

[173] R. T. Wiedmann, R. G. Tonkyn, M. G. White, K. Wang, and V. McKoy, *Rotationally resolved threshold photoelectron spectra of OH and OD*, J. Chem. Phys. **97**, 768 (1992).

[174] R. H. Page, R. J. Larkin, Y. R. Shen, and Y. T. Lee, *High-resolution photoionization spectrum of water molecules in a supersonic beam*, J. Chem. Phys. **88**, 2249 (1988).

[175] A. K. H.-J. Deyerl andLuong, T. G. Clements, and R. E. Continetti, *Transition state dynamics of the OH+ H_2O hydrogen exchange reaction studied by dissociative photodetachment of $H_3O_2^-$*, Faraday Discuss. **115**, 147 (2000).

[176] M. Masamura, *Structures, energetics, and spectra of $OH^-(H_2O)_n$ and $SH^-(H_2O)_n$ clusters, $n = 1$–5: Ab initio study*, J. Chem. Phys. **117**, 5257 (2002).

[177] M. Masamura, *Ab initio molecular orbital study of $OH^-(H_2O)_n$ and $SH^-(H_2O)_n$ in the gas phase*, Chem. Phys. Lett. **339**, 279 (2001).

[178] M. Masamura, *Ab initio MO study on the structures of $OH^-(H_2O)_n$ in the gas phase*, J. Mol. Struct. (Theochem) **498**, 87 (2000).

[179] M. Meot-Ner and C. V. Speller, *Filling of Solvent Shells about Ions. 1. Thermochemical Criteria and the Effects of Isomeric Clusters*, J. Phys. Chem. **90**, 6616 (1986).

[180] J. R. Pliego and J. M. Riveros, *Ab initio study of the hydroxide ion-water clusters: An accurate determination of the thermodynamic properties for the processes $nH_2O + OH^- \rightarrow HO^-(H_2O)_n$ ($n = 1$–4)*, J. Chem. Phys. **112**, 4045 (2000).

[181] S. S. Xantheas, *Theoretical Study of Hydroxide Ion-Water Clusters*, J. Am. Chem. Soc. **117**, 10373 (1995).

[182] J. D. Payzant, R. Yamdagni, and P. Kebarle, *Hydration of CN^-, NO_2^-, NO_3^-, and OH^- in Gas Phase*, Can. J. Chem. **49**, 3308 (1971).

[183] J. J. Novoa, F. Mota, C. P. del Valle, and M. Planas, *Structure of the First Solvation Shell of the Hydroxide Anion. A Model Study Using $OH^-(H_2O)_n$ ($n = 4, 5, 6, 7, 11, 17$) Clusters*, J. Phys. Chem. A **101**, 7842 (1997).

[184] C. P. del Valle and J. J. Novoa, *Density functional computations on the structure and stability of $OH^-(H_2O)_n$ ($n = 1$–3) clusters. A test study*, Chem. Phys. Lett. **269**, 401 (1997).

[185] J. R. Smith, J. B. Kim, and W. C. Lineberger, *High-resolution threshold photodetachment spectroscopy of OH^-*, Phys. Rev. A **55**, 2036 (1997).

[186] T. G. Clements, A. K. Luong, H.-J. Deyerl, and R. E. Continetti, *Dissociative photodetachment studies of $O^-(H_2O)_2$, $OH^-(H_2O)_2$, and the deuterated isotopomers: Energetics and three-body dissociation dynamics*, J. Chem. Phys. **114**, 8436 (2001).

[187] M. J. Frisch, G. W. Trucks, H. B. Schlegel et al., *GAUSSIAN 98 (Revision A.7)* (Gaussian, Inc., Pittsburgh, PA, 1998).

[188] C.-F. Ding, X.-B. Wang, and L.-S. Wang, *Photoelectron Spectroscopy of Doubly Charged Anions: Intramolecular Coulomb Repulsion and Solvent Stabilization*, J. Phys. Chem. A **102**, 8633 (1998).

[189] S. V. Lymar, H. A. Schwarz, and G. Czapski, *Reactions of the Dihydroxylamine ($HNO_2^{-\cdot}$) and Hydronitrite ($NO_2^{2-\cdot}$) Radical Ions*, J. Phys. Chem. A **106**, 7245 (2002).

[190] J. V. Coe, G. H. Lee, J. G. Eaton, S. T. Arnold, H. W. Sarkas, K. H. Bowen, C. Ludewigt, H. Haberland, and D. R. Worsnop, *Photoelectron spectroscopy of hydrated electron cluster anions, $(H_2O)^-_{n=2\text{–}69}$*, J. Chem. Phys. **92**, 3980 (1990).

[191] R. A. Mathies, C. H. B. Cruz, W. T. Pollard, and C. V. Shank, *Direct Observation of the Femtosecond Excited-State cis-trans Isomerization in Bacteriorhodopsin*, Science **240**, 777 (1988).

[192] L. H. Andersen, I. B. Nielsen, M. B. Kristensen, M. O. A. El Ghazaly, S. Haacke, M. B. Nielsen, and M. Å. Petersen, *Absorption of Schiff-Base Retinal Chromophores in Vacuo*, J. Am. Chem. Soc. **127**, 12347 (2005).

[193] N. J. Turro, *Modern Molecular Photochemistry* (University Science Books, 1991).

[194] M. Klessinger and J. Michl, *Excited States and Photochemistry of Organic Molecules* (VCH Publishers, Inc., 1995).

[195] J. B. Fenn, M. Mann, C. K. Meng, S. F. Wong, and C. M. Whitehouse, *Electrospray Ionization for Mass Spectrometry of Large Biomolecules*, Science **246**, 64 (1989).

[196] J. U. Andersen, P. Hvelplund, S. B. Nielsen, S. Tomita, H. Wahlgreen, S. P. Møller, U. V. Pedersen, J. S. Forster, and T. J. D. Jørgensen, *The combination of an electrospray ion source and an electrostatic storage ring for lifetime and spectroscopy experiments on biomolecules*, Rev. Sci. Instr. **73**, 1284 (2002).

[197] I. B. Nielsen, L. Lammich, and L. H. Andersen, *S_1 and S_2 Excited States of Gas-Phase Schiff-Base Retinal Chromophores*, Phys. Rev. Lett. **96**, 018304 (2006).

[198] I. B. Nielsen, *Gas phase studies of protein chromophores. From vacuum to the interior of proteins*, Ph.D. thesis, University of Aarhus, Denmark (2005).

[199] L. L. Helms, *Introduction to probability theory: with contemporary applications* (W. H. Freeman and company, 1997).